bioRxiv preprint doi: https://doi.org/10.1101/561340; this version posted May 15, 2019. The copyright holder for this preprint (which was not certified by peer review) is the author/funder. All rights reserved. No reuse allowed without permission.

Circadian light-mediated endothelial metabolic reprogramming

Yoshimasa Oyama MD, Ph.D.,[1*] Colleen M. Bartman Ph.D.,[1,4*] Stephanie Bonney Ph.D.,[1,4*] J. Scott Lee Ph.D.,[1] Lori A. Walker Ph.D.,[2] Jun Han Ph.D.,[3] Christoph H. Borchers Ph.D.,[3] Peter M. Buttrick M.D.,[2] Carol M. Aherne Ph.D.[1], Nathan Clendenen M.D.,[1] Sean P. Colgan Ph.D.[1] and Tobias Eckle M.D., Ph.D.[1,2,4#]

[*]authors contributed equally

[1]Mucosal Inflammation Program, Departments of Medicine and Anesthesiology, University of Colorado Anschutz Medical Campus, Aurora, CO, USA; [2]Division of Cardiology, Department of Medicine, University of Colorado Anschutz Medical Campus, Aurora, CO, USA, [3]Department of Biochemistry and Microbiology, Genome BC Proteomics Centre, University of Victoria, Victoria, BC, Canada; [4]Graduate Training Program in Cell Biology, Stem Cells, and Development, University of Colorado Anschutz Medical Campus, Aurora, CO, USA

[#]*Correspondence should be addressed to:*
Tobias Eckle, M.D., Ph.D.
Professor of Anesthesiology, Cardiology and Cell Biology
Department of Anesthesiology
University of Colorado Denver
12700 E 19th Avenue, Mailstop B112, RC 2, Room 7121
Aurora, CO 80045; Office: +1-303-724 -2932 or - 2947, Fax: +1-303-724-2852
Email: tobias.eckle@ucdenver.edu

Short title: Intense light as endothelium-targeting strategy in myocardial ischemia

bioRxiv preprint doi: https://doi.org/10.1101/561340; this version posted May 15, 2019. The copyright holder for this preprint (which was not certified by peer review) is the author/funder. All rights reserved. No reuse allowed without permission.

SUMMARY

Consistent daylight oscillations and abundant oxygen availability are fundamental to human health. While both are connected from an evolutionary and cellular perspective, only oxygen is an established therapy in cardiovascular medicine. We investigated the intersection between light- (Period 2, PER2) and oxygen- (hypoxia inducible factor, HIF1A) sensing pathways in cellular adaptation to myocardial ischemia. We demonstrate that intense light is cardioprotective via circadian PER2 amplitude enhancement, mimicking hypoxia elicited adenosine- and HIF1A-metabolic adaptation to myocardial ischemia under normoxic conditions. Whole-genome array analysis from uninjured, intense light exposed wildtype or *Per2*$^{-/-}$ mice and myocardial ischemia in endothelial-specific PER2 deficient mice uncover a critical role for intense light in maintaining endothelial barrier function via light-enhanced HIF1A transcription. A proteomics screen in human endothelia reveals a dominant role for PER2 in metabolic reprogramming to hypoxia via mitochondrial translocation, TCA cycle enzyme activity regulation and HIF1A transcriptional adaption to hypoxia. Translational investigation of intense light in human subjects suggests similar increases in PER2 dependent metabolism, implicating the use of intense light for the treatment of cardiovascular disease.

bioRxiv preprint doi: https://doi.org/10.1101/561340; this version posted May 15, 2019. The copyright holder for this preprint (which was not certified by peer review) is the author/funder. All rights reserved. No reuse allowed without permission.

INTRODUCTION

The appearance of sunlight and oxygen on earth were undoubtedly the most dramatic environmental changes during evolution (Zerkle et al., 2017). As a result, almost all organisms on this planet are equipped with light- and oxygen- sensing pathways. Notably, light sensing and oxygen sensing pathways are linked on a cellular level in mammals (Gu et al., 2000; Hogenesch et al., 1998; McIntosh et al., 2010). Hypoxia inducible factor 1α (HIF1A), an evolutionarily conserved transcription factor enabling cellular adaptation to low oxygen availability (Semenza, 2011), belongs to the same protein family as the light-inducible circadian core protein Period 2 (PER2) (Liu et al., 2012). Both belong to the *PAS* domain superfamily of signal sensors for oxygen, light, or metabolism (Hogenesch et al., 1998; Taylor and Zhulin, 1999). As such, *Hif1α* mRNA levels cycle in a circadian manner in mouse cardiac tissue (Eckle et al., 2012) and rhythmic oxygen levels reset the circadian clock through HIF1A (Adamovich et al., 2017). This evolutionarily conserved relationship between light (circadian)- and oxygen-sensing pathways suggest a role for light elicited circadian rhythm proteins in disease states of low oxygen availability, such as myocardial ischemia.

In the present studies, we sought to develop a cardioprotective strategy using light to target and manipulate PER2 function and uncover mechanisms of PER2 dependent adaptation to hypoxia or ischemia (Eckle et al., 2012). In a comprehensive and systems biology approach, we dissect light and hypoxia elicited pathways in mice and humans from a cellular level to the whole body. Our investigations reveal that circadian PER2 functions at the crossroads between light elicited circadian amplitude enhancement and transcriptional HIF1A-dependent adaptation to oxygen depletion in hypoxia or ischemia. Combined, we demonstrate a mechanistic understanding of cardioprotection with light therapy by targeting and manipulating hypoxic pathways to reduce infarct sizes after myocardial ischemia.

bioRxiv preprint doi: https://doi.org/10.1101/561340; this version posted May 15, 2019. The copyright holder for this preprint (which was not certified by peer review) is the author/funder. All rights reserved. No reuse allowed without permission.

RESULTS

Intense light elicited cardiac PER2 amplitude enhancement as a novel cardioprotective mechanism

Intense light is the dominant regulator of human circadian rhythms and PER2 activity (Albrecht et al., 2001; Bonney et al., 2013; Remi, 2015). Here we investigated intense light exposure protocols and found that housing mice under "intense light conditions" (10,000 LUX, full spectrum, UV-filter, L(light):D(dark) phase 14:10h) robustly enhances cardioprotection, reflected as a time-dependent decrease in infarct size and circulating troponin-I levels **(Fig. 1A-C**). The following evaluation of locomotor activity, as determined by wheel running during intense light housing, excluded a phase shift of the circadian period as the underlying mechanism, but identified increases of the total distance walked or the circadian amplitude (**Fig. 1D-F, Supplementary Fig. 1**). Indeed, after housing PER2 reporter mice under intense light for one week, we found increases in the circadian peak and trough levels of cardiac PER2 protein levels (**Fig. 1G**). Further analysis of wheel running activity in *Per2*$^{-/-}$ mice revealed intense light elicited increases of the total distance walked or the circadian amplitude to be PER2 dependent (**Fig. 1H-J, Supplementary Fig. 2A-B**).

To confirm that cardiac circadian PER2 amplitude enhancement requires visual light perception, we enucleated wildtype mice to remove any light sensing structures. Ocular enucleation induced a complete loss of PER2 stabilization in "blind" mice exposed to intense light conditions compared to "seeing" animals. **(Fig. 1K, L)**. Myocardial ischemia and reperfusion studies in blind mice under room light housing conditions found 'shifted' cardiac troponin kinetics (Troponin 'blind': ZT3 [9AM] < ZT15 [9PM] vs Troponin 'seeing': ZT3>ZT15) and slightly overall higher troponin levels in 'blind; mice ('blind' vs 'seeing' troponin: 168 vs 118 ng/ml, not significant), indicating a lack of circadian synchronization by light **(Fig. 1M, Supplementary Fig. 2C).** Indeed, wheel running activity in 'blind mice'

bioRxiv preprint doi: https://doi.org/10.1101/561340; this version posted May 15, 2019. The copyright holder for this preprint (which was not certified by peer review) is the author/funder. All rights reserved. No reuse allowed without permission.

demonstrated abolished increase of the circadian amplitude similar to *Per2*$^{-/-}$ mice (**Fig. 1N**, **Supplementary Fig. 2D).**

To evaluate if intense light-mediated increases of circulating cortisol levels (Oster et al., 2017) or the temperature (Schibler et al., 2015) could have caused the observed circadian amplitude enhancement, we next measured rectal temperatures or plasma cortisol levels following 7 days of intense or room light housing. However, we did not observe increases in plasma cortisol levels, or the body temperature in intense light-exposed mice when compared to controls (**Supplementary Fig. 3)**.

Together, these data demonstrate that intense light elicited cardiac circadian amplitude is a novel cardioprotective strategy which requires PER2 and visual light perception.

Intense light 'adenosine-preconditions' and increases HIF1A-HRE binding in the heart before an ischemic insult

Next, we further deciphered the mechanism of intense light elicited cardiac circadian amplitude enhancement and cardioprotection. First, we evaluated the effect of intense light on infarct sizes or circulating troponin-I levels at ZT15, as one week of intense light housing had increased cardiac PER2 protein levels significantly more at ZT15 (9PM) compared to ZT3 (9AM) (**Fig. 1G**). However, we only found slightly smaller infarct sizes or troponin-I levels at ZT15 compared to ZT3 (**Fig. 2A**). Thus, all following studies focused on the robust cardioprotective effect observed at ZT3.

Since intense light had increased the physical activity in mice (**Fig. 1E**), we investigated the influence of voluntary wheel running (Schroeder et al., 2012) on the circadian amplitude and myocardial infarct sizes. In contrast to intense light exposure, however, two weeks of voluntary wheel running with a longer distance walked were necessary until we noted robust cardioprotection from myocardial ischemia **(Fig. 2B)** or a significant increase of the circadian amplitude **(Fig. 2C)**. Nevertheless, the total distance achieved on the wheel inversely correlated

bioRxiv preprint doi: https://doi.org/10.1101/561340; this version posted May 15, 2019. The copyright holder for this preprint (which was not certified by peer review) is the author/funder. All rights reserved. No reuse allowed without permission.

with infarct sizes **(Fig. 2D)**. We, therefore, evaluated two weeks of voluntary wheel running in *Per2*$^{-/-}$ mice, which revealed a decrease in total running distance, decreased circadian amplitude, increased infarct sizes and significant circadian disruption in *Per2*$^{-/-}$ mice compared to wildtype controls (**Fig. 2E-H)**. These findings demonstrate that PER2 is essential for driving the precise rhythmicity of circadian oscillations (Hallows et al., 2013).

As adenosine-mediated increases of cAMP is a core component of PER2 expression and PER2 mediated ischemic preconditioning of the heart (Eckle et al., 2012; O'Neill et al., 2008), we next evaluated if intense light also 'preconditioned' the heart similar to ischemia. Analyzing uninjured hearts from wildtype or *Per2*$^{-/-}$ mice after one week of intense light 'preconditioning' we discovered that intense light significantly increased cardiac adenosine or cAMP levels, which was abolished in *Per2*$^{-/-}$ mice **(Fig. 2 I-J).** As light elicited adenosine increase was abolished in *Per2*$^{-/-}$ mice, and light induction of cardiac PER2 protein required visual perception (**Fig. 1K**), these data suggest intense light elicited adenosine as circulating signaling molecule from the brain (Zhang et al., 2006) to enhance peripheral PER2 expression.

Based on observations that PER2 initiates a switch from energy-efficient lipid to oxygen-efficient glucose metabolism during myocardial ischemia which is pivotal to allow the myocardium to function (Aragones et al., 2009; Eckle et al., 2012), we next assessed the effect of intense light on glycolytic flux rates during normoxia as a possible underlying mechanism. Using liquid chromatography-tandem mass spectrometry studies following the infusion of labeled glucose ([U]^{13}C-glucose), we found that intense light significantly increased the glycolytic flux in cardiac tissue before an ischemic event (**Fig. 2K**). We further found that intense light increased the activity of the key and rate-limiting enzyme of glycolysis (phosphofructokinase) in heart tissue or plasma in a PER2 dependent manner (**Fig. 2L-M**).

Considering glycolysis is HIF1A regulated under conditions of low oxygen availability (Krishnan et al., 2009), we next investigated if intense light would also increase cardiac HIF1A-hypoxia response element (HRE) binding under normoxia and before an ischemic insult.

bioRxiv preprint doi: https://doi.org/10.1101/561340; this version posted May 15, 2019. The copyright holder for this preprint (which was not certified by peer review) is the author/funder. All rights reserved. No reuse allowed without permission.

Indeed, intense light significantly increased total cardiac HIF1A-HRE binding at ZT15 vs. ZT3 when compared to room light conditions (**Fig. 2N**). Finally, subsequent myocardial ischemia and reperfusion studies in *Per2*$^{-/-}$ mice confirmed that intense light elicited circadian amplitude enhancement and subsequent cardioprotection was PER2 dependent (**Fig. 2O, P**).

Taken together, these studies found that intense light does not work via increases of physical activity only, but 'preconditions' cardiac tissue via increases of cardiac adenosine-cAMP signaling, via increases of HIF1A-HRE binding and via increases of energy efficient and HIF1A regulated glycolysis prior to an ischemic insult. Furthermore, our data suggest intense light elicited adenosine as circulating signaling molecule (Zhang et al., 2006) to enhance peripheral PER2 mediated cardioprotection.

Intense light elicited cardioprotection is abolished in mice with endothelial-specific deletion of *Per2* and improves the endothelial barrier function via light-enhanced HIF1A transcription

To further understand intense light elicited and PER2 dependent pathways, we performed a genome-wide array, profiling intense light-dependent gene expression before an ischemic event. *In silico* analysis found dominant regulation of circadian and metabolic pathways (**Fig. 3A**) and identified the hypoxia/HIF1A-regulated and metabolic key player Angiopoietin-Like 4 (ANGPTL4) as the top light and PER2 dependent gene **(Fig. 3B)**, supporting our findings that intense light elicited PER2 activates HIF1A regulated metabolic pathways under normoxic conditions. As ANGPTL4 is an endothelial secreted protein which protects the endothelial barrier function during acute myocardial IR-injury (Galaup et al., 2012), we next evaluated endothelial specific *Per2* deletion in myocardial IR-injury. Using a novel tissue-specific mouse line with a 70% deletion of PER2 in the endothelium (**Fig. 3C,** *Per2*$^{loxP/loxP}$-VE-Cadherin-Cre, **Supplementary Fig. 4**), we found significantly increased infarct sizes and troponin-I serum levels in *Per2*$^{loxP/loxP}$-VE-Cadherin-Cre (**Fig. 3D-F)**. In fact, intense light elicited

bioRxiv preprint doi: https://doi.org/10.1101/561340; this version posted May 15, 2019. The copyright holder for this preprint (which was not certified by peer review) is the author/funder. All rights reserved. No reuse allowed without permission.

cardioprotection was abolished in *Per2*$^{loxP/loxP}$-VE-Cadherin-Cre mice. As these data implicated intense light in maintaining the vascular integrity during myocardial IR-injury, we determined the vascular leakage of Evans blue dye following 7 days of room light or intense light housing. As shown in **Figure 3G-I**, intense light 'pretreatment' significantly improved endothelial barrier function during myocardial IR-injury which was abolished in endothelial-specific *Per2*$^{-/-}$ mice.

Recent studies identified adenosine signaling via the adenosine A2B receptor (ADORA2B) as a crucial pathway for PER2 stabilization during myocardial ischemia (Eckle et al., 2012). As intense light had increased cardiac adenosine levels, we questioned if ADORA2B mediated adenosine signaling would be the signaling link between the brain and the heart. Indeed, our data revealed abolished intense light therapy mediated improvement of the endothelial barrier function in *Adora2b*$^{-/-}$ mice (**Figure 3J)**.

Considering intense light had increased HIF1A-HRE binding at ZT15, we next evaluated HIF1A binding to the promoter region of mouse *Angptl4* at ZT15. Evaluation of mouse *Angptl4* promoter regions identified several HRE binding sites (**Supplementary Fig. 5)**, and the following ChIP assay demonstrated significantly increased HIF1A binding in two promoter regions (**Figure 3K, Supplementary Fig. 5)**.

Taken together these data identify endothelial specific PER2 as a mechanism of intense light elicited cardioprotection and suggest intense light as a strategy to improve endothelial barrier function via increasing adenosine-ADORA2B signaling and HIF1A-transcription.

Endothelial PER2 is critical for the transcriptional control of HIF1A dependent glycolysis

Based on our findings for a vital role of endothelial-specific PER2 in intense light-mediated cardioprotection and endothelial barrier protection during myocardial IR-injury *in vivo*, we next evaluated endothelial PER2 signaling targets during hypoxia *in vitro*. For this purpose, we generated a novel lentiviral-mediated PER2 knockdown (KD) stable cell line in human

bioRxiv preprint doi: https://doi.org/10.1101/561340; this version posted May 15, 2019. The copyright holder for this preprint (which was not certified by peer review) is the author/funder. All rights reserved. No reuse allowed without permission.

microvascular endothelial cells (HMEC-1). Similar to previous studies in PER2 gene-targeted mice (Eckle et al., 2012), hypoxia increased PER2 transcript or protein levels in HMEC-1 scrambled (Scr) controls, whereas PER2KD HMEC-1 displayed abolished transcriptional induction of HIF1A dependent glycolytic enzymes, attenuated lactate production, reduced glycolytic capacity, and increased cytotoxicity (**Supplementary Fig.6**). Based on observations in HMEC-1 that PER2 is significantly increased at 24h after cell synchronization when compared to the 12h time point (Eckle et al., 2012), we determined whether oscillatory higher PER2 levels would affect metabolism under normoxic conditions. These studies revealed a significant increase of glycolytic capacity in control HMEC-1 compared to PER2KD cells at the 24h time point (**Supplementary Fig.7A-B**). Mechanistic studies, using a chromatin immunoprecipitation assay (ChIP) uncovered hypoxia-induced HIF1A binding to the human lactate dehydrogenase promotor region, a response that was abolished in PER2KD cells (**Supplementary Fig.7C**).

Together, these findings uncover a critical role for endothelial PER2 in cellular metabolic adaption under normoxia or hypoxia and reveal endothelial PER2 as an essential co-factor of HIF1A mediated transcription of glycolytic genes, and thus a key regulator of glycolytic metabolism.

Identification of endothelial PER2 as a regulator of TCA cycle activity

As hypoxia increased PER2 protein like intense light, we next used an unbiased affinity purification-mass spectrometry-based proteomics screen for PER2 protein interactions under hypoxic conditions to gain a deeper mechanistic perspective of endothelial PER2 dependent mechanisms **(Fig. 4A, Supplementary Table 1, Supplementary Fig. 8**). Serendipitously, a high percentage of PER2-protein interactions hinted towards an essential role for PER2 in controlling TCA cycle function (**Fig. 4B**). Subsequent Co-IP pull-downs on TCA cycle enzymes confirmed binding to PER2 during hypoxia (**Fig. 4C, D**). Following analyses of

bioRxiv preprint doi: https://doi.org/10.1101/561340; this version posted May 15, 2019. The copyright holder for this preprint (which was not certified by peer review) is the author/funder. All rights reserved. No reuse allowed without permission.

subcellular compartments found that hypoxia increased PER2 protein levels in the cytoplasm, nucleus and the mitochondria (**Fig. 4E**). Thus, PER2 protein interactions may facilitate the transport of mitochondrial proteins, which are almost exclusively synthesized in the cytosol. In fact, our proteomics screen indicated PER2 binding to the mitochondrial outer membrane translocase (Tom) complex [**Supplementary Table 1** (Faou and Hoogenraad, 2012)], which is the main protein entry gate of mitochondria (Boengler et al., 2011). Following co-localization studies confirmed PER2 translocation into the mitochondria during hypoxia **(Fig. 4F, Supplementary Fig. 9)**. Functional assays on TCA cycle enzyme activity revealed regulation of TCA cycle function during hypoxia in a PER2 dependent manner (**Fig. 4G-I**), and hypoxic PER2 KD cells showed significantly less CO_2 production, a surrogate endpoint of TCA cycle function (**Fig. 4J**).

Considering TCA cycle enzyme activity is also known to be regulated by Sirtuin3 (SIRT3) mediated de-acetylation (Yu et al., 2012), which is under circadian control (Peek et al., 2013), we investigated whether hypoxia and HIF1A-PER2 dependent pathways would regulate SIRT3 expression. HMEC-1 transcriptional or translational analyses with a PER2- or HIF1AKD revealed a PER2-HIF1A dependent regulation of SIRT3 under hypoxic conditions (**Fig. 4K-M**, **Supplementary Fig. 10A-B)**. *In silico* analysis confirmed a hypoxia response element (HRE) in the human promoter region of SIRT3 **(Supplementary Fig. 10C)**.

Together, our proteomics screen uncovered a critical role for endothelial PER2 in controlling oxidative TCA cycle metabolism during hypoxia by translocating into the mitochondria and via transcriptional regulation of HIF1A-SIRT3-dependent pathways. These data suggest a more complex function of PER2, possibly controlling the TCA cycle function via post-translational mechanisms.

Endothelial PER2 regulates mitochondrial ATP generation via HIF1A-COX4.2

bioRxiv preprint doi: https://doi.org/10.1101/561340; this version posted May 15, 2019. The copyright holder for this preprint (which was not certified by peer review) is the author/funder. All rights reserved. No reuse allowed without permission.

Additional analysis of our proteomics screen indicated binding of PER2 to mitochondrial complex 4 (**Supplementary Table 1,** *Cytochrome C*), supporting a role for PER2 in controlling mitochondrial function under hypoxia. Indeed, oxygen consumption rates (OCR; a measure of mitochondrial functionality), basal respiration, maximal respiration, ATP production, spare capacity, and maximal respiration were significantly reduced in PER2KD cells during a mitochondrial stress test **(Fig. 5A-D, Supplementary Fig. 11A, B)**. Moreover, OCR levels were significantly increased in cells with higher PER2 levels at time point 24h when compared to 12h post cell synchronization (Eckle et al., 2012). These findings highlight a role for oscillatory PER2 overexpression in metabolic adaptation under normoxia (**Supplementary Fig 11C, D).**

Considering HIF1A mediates a switch of complex 4 subunits (COX4.1 to COX4.2) in hypoxia to enhance oxygen efficiency, which conserves cellular ATP content (Fukuda et al., 2007), we next investigated the transcriptional regulation of COX4.2 in PER2KD cells under hypoxia. Here, we found abolished increases of COX4.2 mRNA or complex 4 activity in hypoxic PER2KD cells or ischemic hearts from *Per2*$^{-/-}$ mice, respectively (**Fig. 5E, F**).

To understand if compromised oxidative phosphorylation in PER2 deficiency would be associated with a reduced mitochondrial membrane potential, which is associated with compromised mitochondrial function (Solaini et al., 2010), we next used MitoTracker deep red staining (Zhou et al., 2011). Studies in PER2KD HMEC-1 indicated already reduced mitochondrial potential under normoxia (**Fig. 5G)**. Indeed, analysis of a cell energy phenotype assay revealed significantly less aerobic metabolism in PER2KD cells at baseline (**Supplementary Fig. 12)**. Confirming these results, JC-1 assay showed a significant reduction of the membrane potential in PER2 KD cells at both normoxia and under hypoxia (**Fig. 5H, Supplementary Fig. 13**).

To further explore PER2 dependent metabolism, we next used liquid chromatography-tandem mass spectrometry studies following the exposure of labeled glucose (^{13}C-glucose) or

bioRxiv preprint doi: https://doi.org/10.1101/561340; this version posted May 15, 2019. The copyright holder for this preprint (which was not certified by peer review) is the author/funder. All rights reserved. No reuse allowed without permission.

palmitic acid (^{13}C-palmitic acid) to assess metabolic flux rates in PER2KD endothelial cells. Here we confirmed that PER2 is an essential regulator of glycolysis and oxidative metabolism under hypoxia (**Fig. 5I-J**). Moreover, we also found PER2 to be critical for the pentose phosphate pathway under normoxia or hypoxia, indicating that PER2KD cells are compromised in generating the redox cofactor NADPH, which has a pivotal role for circadian timekeeping (**Fig. 5K**) (Rey et al., 2016). As PER2 has been shown to inhibit lipid metabolism via PPARγ (Grimaldi et al., 2010), we also found altered fatty acid metabolism in PER2KD cells under hypoxia (**Fig. 5L**). *In silico* analysis of our proteomics screen confirmed these findings and highlight PER2 as a master regulator of endothelial energy metabolism (**Supplementary Fig. 14.).**

As ATP has been implicated in endothelial barrier enhancement and tight junction functionality (Kolosova et al., 2005), we next evaluated endothelial barrier function of PER2KD HMECs and controls during a 24h hypoxia time course. As shown in **Figure 5M**, PER2KD HMEC demonstrated increased cell permeability at 2, 4, 6, 12 and 24 h of hypoxia when compared to scrambled controls.

Taken together, these data identify endothelial PER2 as the critical control point of energy homeostasis via transcriptional regulation of HIF1A dependent mitochondrial respiration, ultimately conserving the endothelial function.

A light-sensing human endothelial cell line recapitulates *in vivo* light exposure

As proof of concept that PER2 mimics HIF1A pathways under normoxia, we reiterated light sensing for PER2 overexpression on a cellular level by generating an HMEC-1 line, overexpressing the human light sensing photopigment melanopsin (OPN4), a retinal ganglion cell receptor responsible for circadian entrainment. Exposing the light sensing HMEC-1 cultures to light resulted in a significant increase of cAMP, phospho-CREB (cyclic AMP-responsive element binding protein), PER2 mRNA, glycolytic capacity and oxygen

bioRxiv preprint doi: https://doi.org/10.1101/561340; this version posted May 15, 2019. The copyright holder for this preprint (which was not certified by peer review) is the author/funder. All rights reserved. No reuse allowed without permission.

consumption rates (**Fig. 6A-H)**. Taken together, these studies recapitulate that normoxic PER2 overexpression can optimize cellular metabolism in a similar fashion as seen under hypoxic conditions.

In summary, our *in vivo* and *in vitro* studies on light-elicited pathways identified a light perception dependent circadian entrainment mechanism through adenosine-cAMP and HIF1A transcriptional adaptation in a PER2 regulated manner. Furthermore, our studies discover that light or hypoxia elicits PER2 as a critical factor in maintaining endothelial barrier function during myocardial ischemia via metabolic reprogramming (**Fig. 6I**).

Intense light enhances the circadian amplitude and PER2 dependent metabolism in humans

Next, we investigated if intense light would have similar effects on healthy human volunteers. Based on strategies using intense light therapy [10,000 LUX] to treat seasonal mood disorders or depression in humans (Yorguner Kupeli et al., 2017), we adopted a similar protocol. We exposed healthy human volunteers to 30 min of intense light in the morning on 5 consecutive days and performed serial blood draws. Intense light therapy increased PER2 protein levels in human buccal or plasma samples in the morning (9AM) or evening (9PM), indicating an enhancement of the circadian amplitude in different tissues at the same time via light therapy (**Fig. 7A-C, Supplementary Fig. 15)**. To test the efficacy of intense light therapy on the circadian system (Lewy et al., 1980), we determined melatonin plasma levels, which were significantly suppressed upon light treatment (**Fig. 7D, E**). Also, room light was less efficient than intense light therapy in suppressing melatonin (**Fig. 7D**).

Further analyses revealed that intense light therapy increased plasma phosphofructokinase at 9AM or 9PM (**Fig. 7F, G**). Moreover, plasma triglycerides, a surrogate for insulin sensitivity and carbohydrate metabolism (Ginsberg et al., 2005), significantly decreased upon light therapy (**Fig. 7H**), indicating increased insulin sensitivity and glucose

bioRxiv preprint doi: https://doi.org/10.1101/561340; this version posted May 15, 2019. The copyright holder for this preprint (which was not certified by peer review) is the author/funder. All rights reserved. No reuse allowed without permission.

metabolism. Targeted metabolomics from human plasma samples confirmed a strong effect of light therapy on metabolic pathways such as glycolysis or TCA cycle (**Fig. 7I, Supplementary Fig. 16**). We found significant decreases in pyruvate or succinate levels after 5 days of light therapy (**Fig. 7J-K**). Together with increased plasma phosphofructokinase activity, this finding indicates improved metabolic flux, possibly due to increased glycolysis, improved TCA cycle or mitochondrial function.

As sleep deprivation is directly associated with decreased insulin sensitivity and compromised glucose metabolism (Depner et al., 2014), we next determined how our light therapy protocol would impact human physiology in terms of sleep behavior. Using a validated accelerometer for actigraphy (Lee and Suen, 2017) (Actiwatch 2) we found less WASO (wake after sleep onset) episodes, overall improved sleep efficiency, increased day-activity and increases of the circadian amplitude (**Fig. 7L-P, Supplementary Fig. 17**). Taken together, our data suggest that intense light therapy, a mechanism of circadian amplitude enhancement, targets similar PER2 dependent metabolic pathways in humans as seen in mice and may present a promising novel strategy for the treatment or prevention of low oxygen conditions such as myocardial ischemia.

bioRxiv preprint doi: https://doi.org/10.1101/561340; this version posted May 15, 2019. The copyright holder for this preprint (which was not certified by peer review) is the author/funder. All rights reserved. No reuse allowed without permission.

DISCUSSION

In the present study, we demonstrated a potential role for intense light in cardioprotection from myocardial ischemia. *In vivo* murine studies using 14h-daily-intense light exposure up to one week revealed a robust and time-dependent cardioprotective effect. Following studies on intense light elicited cardioprotection uncovered circadian amplitude enhancement of cardiac PER2 as an underlying mechanism. The intense light was found to increase cardiac adenosine, cAMP, and glycolysis before ischemia in a PER2 dependent manner, with targeted gene deletion of PER2 abolishing the intense light induced cardioprotective effects. A whole genome array on intense light and PER2 dependent pathways indicated that intense light activates HIF1A mediated pathways under normoxia in the uninjured heart and pointed towards a critical role for endothelial PER2 in regulating such pathways. Studies on myocardial IR-injury using endothelial specific PER2 deficient mice revealed abolished cardioprotection by intense light. Moreover, intense light enhanced HIF1A-transcription in the uninjured heart and improved the endothelial barrier function in an endothelial-PER2 specific manner during myocardial ischemia. In-depth mechanistic studies on endothelial PER2 function revealed a prominent metabolic role for PER2 under hypoxia or normoxia, controlling glycolysis, TCA cycle or mitochondrial respiration. Translational studies in humans found that intense light activated similar pathways as seen in our murine studies. Together, these studies point towards PER2 as a critical control point of endothelial metabolic reprogramming to maintain vascular integrity during myocardial IR-injury and suggest intense light to increase PER2 signaling as a therapeutic strategy for the treatment of coronary artery disease.

We found that intense light can decrease murine infarct sizes, increase murine cardiac glycolysis, adenosine, cAMP, HIF1A-transcription, endothelial barrier function, and affects human metabolism which establishes a critical role for intense light in regulating critical biological processes (Zadeh et al., 2014). Epidemiologic studies noting an increase in MIs

bioRxiv preprint doi: https://doi.org/10.1101/561340; this version posted May 15, 2019. The copyright holder for this preprint (which was not certified by peer review) is the author/funder. All rights reserved. No reuse allowed without permission.

during the darker winter months in *all* US states (Spencer et al., 1998) provide strong evidence to support our conclusion that intense light elicits robust cardioprotection. The mechanism of how the entrainment signal gets to peripheral organs remains unclear but may incorporate neuro-hormonal factors, or autonomic innervation (Takahashi, 2017). Studies on altered liver metabolism in constant darkness found adenosine as a possible circulating circadian factor (Zhang et al., 2006), which suggests adenosine signaling as a mechanism for establishing circadian rhythmicity between peripheral organs and the suprachiasmatic nuclei (SCN). Indeed, the importance of adenosine signaling via the adenosine A2B receptor (ADORA2B) and following cAMP increases for PER2 stabilization and cardiac metabolic adaption to ischemia has been shown in recent studies investigating the mechanism of myocardial ischemic preconditioning (Eckle et al., 2012). In the current studies, we found that light elicited cardiac circadian amplitude enhancement increased cardiac adenosine and cAMP levels under normoxia, which was also PER2 dependent. While we did not determine plasma adenosine levels, we were able to detect adenosine increases in blood containing and flash frozen mouse hearts following one week of the intense light housing. Since intense light pre-treatment did not improve the endothelial barrier function in *Adora2b* deficient mice, adenosine signaling likely plays an essential role in transmitting the 'cardioprotective' light signal from the SCN to the heart.

While cardiomyocytes are significant oxygen consumers and account for approximately 75% of the myocardial volume, there is at least one capillary adjacent to every cardiomyocyte, and cardiomyocytes are outnumbered 3:1 by the endothelial cells (Brutsaert, 2003). Recent electron microscopic investigations during reperfusion after cardioplegia suggest that endothelial cells might be even more prone to damage during reperfusion than cardiomyocytes (Schmiedl et al., 2002). Mitochondrial metabolism in endothelial cells has been proposed as a central oxygen sensor in the vasculature (Davidson and Duchen, 2007), and studies have

bioRxiv preprint doi: https://doi.org/10.1101/561340; this version posted May 15, 2019. The copyright holder for this preprint (which was not certified by peer review) is the author/funder. All rights reserved. No reuse allowed without permission.

suggested that human endothelial cells can regulate the activity of HIF1A, thus affecting key response pathways to hypoxia and metabolic stress (Davidson and Duchen, 2007). Endothelial damage also accounts for the "no-reflow" phenomenon observed when regions of a de-occluded heart do not restore normal blood flow (Reffelmann and Kloner, 2006). As such, endothelial dysfunction plays a significant role in myocardial IR-injury, rendering endothelial cells an attractive target for myocardial protection (Yang et al., 2016). In the current studies, we uncovered a critical role for light elicited PER2 as a regulator of endothelial metabolism. While PER2 has been implicated in controlling endothelial function in previous studies (Viswambharan et al., 2007; Wang et al., 2008), an endothelial specific role of PER2 during acute myocardial IR-injury, which can be targeted using intense light, has not yet been described. Moreover, our *in vivo* and *in vitro* studies suggest that light elicited reprogramming of endothelial metabolism protects the endothelial barrier function during IR-injury. Together with previous studies on myocardial IR-injury (Yang et al., 2016), these studies highlight the importance of cardiac endothelial metabolism in IR-injury and point towards unrecognized therapeutic strategies for cardiovascular disease using intense light or pharmacological compounds, such as the circadian rhythm enhancer nobiletin (Gile et al., 2018; Oyama et al., 2018), to increase endothelial PER2 amplitude.

The importance of HIF1A in cardioprotection has been shown in numerous studies (Semenza, 2014) and the interaction between HIF1A and PER2 has been demonstrated on the protein (Eckle et al., 2012; Kobayashi et al., 2017) and transcriptome level (Wu et al., 2017), In general, HIF1A requires hypoxic conditions to be stabilized (Semenza, 2014). In the current studies, we further established the dependence of HIF1A on PER2 as a transcription factor during hypoxia, supporting previous studies on PER2 function as an effector molecule for the recruitment of HIF1A to promoter regions of its downstream genes (Kobayashi et al., 2017). However, we also found that specific HIF1A pathways such as glycolysis or ANGPTL4

bioRxiv preprint doi: https://doi.org/10.1101/561340; this version posted May 15, 2019. The copyright holder for this preprint (which was not certified by peer review) is the author/funder. All rights reserved. No reuse allowed without permission.

signaling can also be activated via light elicited circadian overexpression of PER2 under normoxia. These findings would suggest that PER2 amplitude enhancement strategies can 'precondition' the myocardium by establishing a HIF1A-similar signaling environment before an ischemic event. Indeed, we demonstrated that intense light increased overall cardiac HIF1A-HRE binding or HIF1A-transcription of the endothelial barrier protective factor *Angptl4*.

Given a close association of circadian amplitude dampening and disease progression (Gloston et al., 2017), 'clock'-enhancing strategies are promising novel approaches for disease treatment. Although it is well known that light regulates circadian rhythms (Czeisler et al., 1990) and that high intensities of light are more effective for circadian entrainment and amplitude enhancement (Lewy et al., 1980), only a few reports exist on circadian entrainment and cardioprotection (Martino et al., 2007). While previous studies suggested that short term intense light exposure could mediate cardioprotection in a PER2 dependent manner (Eckle et al., 2012), no specific mechanisms were provided. In the current studies, we uncovered that intense light elicited cardioprotection works via amplitude enhancement of endothelial-specific PER2 and profiling of intense light elicited and PER2 dependent gene expression revealed intense light activation of circadian, metabolic or HIF1A regulated pathways. In fact, our *in vivo* and *in vitro* studies demonstrated that PER2 is not only an essential co-factor of HIF1A transcription in metabolic adaptation of the hypoxic endothelium but also activates hypoxia-dependent pathways under normoxic conditions.

It is essential to note the translation of our findings from mice as a model system to humans. Indeed, our light exposure strategy in humans showed similar kinetics as in mice. It is well known that circadian rhythms function independently of a diurnal or nocturnal behavior due to multiple yet parallel outputs from the SCN (Kronfeld-Schor et al., 2013). Very basic features of the circadian system are the same in apparently diurnal and nocturnal animals, including the molecular oscillatory machinery and the mechanisms responsible for pacemaker

bioRxiv preprint doi: https://doi.org/10.1101/561340; this version posted May 15, 2019. The copyright holder for this preprint (which was not certified by peer review) is the author/funder. All rights reserved. No reuse allowed without permission.

entrainment by light (Kronfeld-Schor et al., 2013). Also, PER2 is hypoxia-regulated in mice and humans, which supports similar mechanisms in both species (Eckle et al., 2012). HIF1A regulation and function under hypoxia, which is strongly associated with PER2 (Kobayashi et al., 2017), also seems to be independent of a nocturnal nature (Semenza, 2014), despite HIF1A expression being under circadian control (Wu et al., 2017). Indeed, human and mouse studies on HIF1A find similar responses to cardiovascular ischemic events (Semenza, 2014).

Supporting the importance of circadian rhythms in myocardial susceptibility to ischemia, recent studies found a diurnal pattern for troponin values in patients undergoing aortic valve replacement (Montaigne et al., 2018). Here, troponin values following surgery were significantly higher in the morning when compared to the afternoon. While nothing can be done about a diurnal pattern, applying light therapy before high risk non-cardiac or cardiac surgery to enhance the circadian amplitude, however, might be able to provide robust cardioprotection. Light elicited circadian amplitude enhancement suggests an overall increase in PER2 levels and concomitant cardioprotection even at the trough of the amplitude, indicating that this strategy could promote general cardioprotection and potentially decrease troponin levels in both the morning and evening times. Despite the fact we show that circadian amplitude enhancement is a reasonable strategy for adaptive protection from myocardial ischemia, its potential to also protect against the consequences of an ischemic event, however, will need further investigation in mechanistic research endeavors.

bioRxiv preprint doi: https://doi.org/10.1101/561340; this version posted May 15, 2019. The copyright holder for this preprint (which was not certified by peer review) is the author/funder. All rights reserved. No reuse allowed without permission.

Acknowledgement

The authors wish to acknowledge Melissa Card, the University of Colorado Molecular and Cellular Analytical Core of the Colorado Nutrition and Obesity Research Center for use of the Seahorse Bioanalyzer, and the University of Colorado School of Medicine Biological Mass Spectrometry Core Facility for technical assistance.

Funding:

The present research work is supported by National Heart, Lung, and Blood Institute Grant (NIH-NHLBI) 5R01HL122472 to T.E., Colorado Clinical and Translational Sciences Institute (CCTSI) TL1 TR001081 and American Heart Association (AHA) Predoctoral Fellowship 16PRE30510006 Grant to C.M.B and AHA Postdoctoral Fellowship 19POST34380105 Grant to Y.O.

Competing interests: The authors declare there are no conflicts of interest.

bioRxiv preprint doi: https://doi.org/10.1101/561340; this version posted May 15, 2019. The copyright holder for this preprint (which was not certified by peer review) is the author/funder. All rights reserved. No reuse allowed without permission.

Figures and Figure Legends

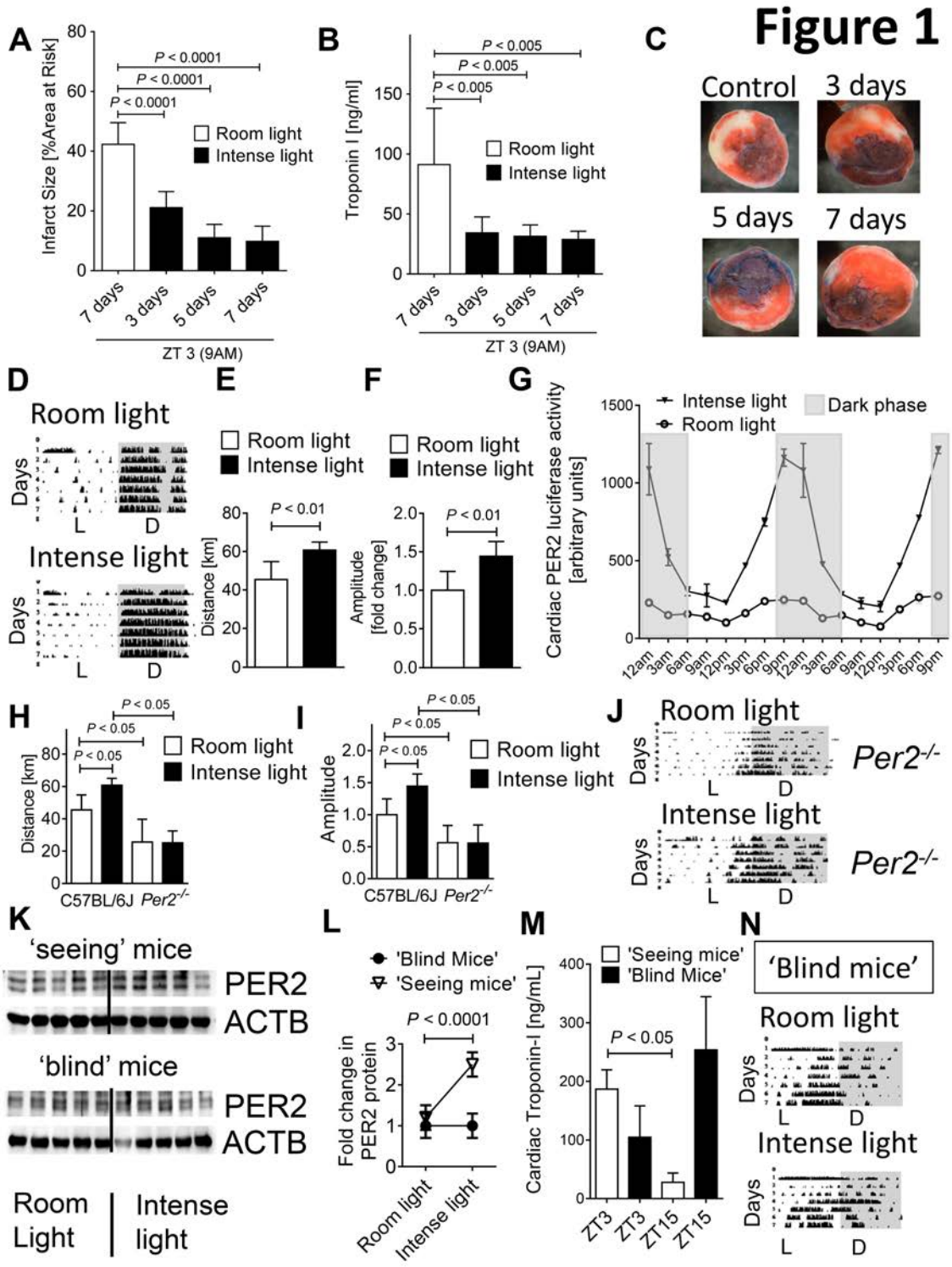

Figure 1. Intense light elicited circadian PER2 amplitude enhancement is cardioprotective. (A-C) C57BL/6 mice housed under intense light conditions (10,000 LUX, L:D 14:10 h) for 3, 5, or 7 days were subjected to 60 min of *in situ* myocardial ischemia

bioRxiv preprint doi: https://doi.org/10.1101/561340; this version posted May 15, 2019. The copyright holder for this preprint (which was not certified by peer review) is the author/funder. All rights reserved. No reuse allowed without permission.

followed by 2h reperfusion at ZT3 (9AM) and compared to mice housed under standard room light (200 LUX, L:D 14:10 h, 7 days). Infarct sizes are expressed as the percent of the area at risk that was exposed to myocardial ischemia (double staining with Evan's blue and triphenyltetrazolium chloride; mean±SD; n=6). **(B)** Parallel measurements of serum troponin-I by ELISA (mean±SD; n=6). **(C)** Representative images of infarcts. **(D-F)** Wheel running measurements during 7 days of room light or intense light housing conditions in C57BL/6J mice (L=light phase, D=dark phase, n=6, see also **Supplementary Fig. 1** for individual recordings). **(G)** Cardiac PER2 luciferase activity indicating protein in mice after intense light or standard room light for 7 days (mean±SD; n=4). **(H-J)** Wheel running during 7 days of room light or intense light housing in C57BL/6J and *Per2*$^{-/-}$ mice (n=5-6, see also **Supplementary Fig. 2** for individual recordings). (**K, L**) Immunoblot and quantification for PER2 protein in seeing or enucleated (blind) C57BL/6 mice after 7 days of room light or intense light at ZT3 (mean±SD; n=5). **(M**) Troponin-I serum levels in seeing or blind C57BL/6J mice housed under room light conditions followed by 60 min ischemia and 2 h reperfusion at ZT3 or ZT15 (mean±SD; n=4, see also **Supplementary Fig. 2**). **(N)** Wheel running measurements during 7 days of room light or intense light housing conditions in 'blind' C57BL/6J mice (mean±SD; n=6, see also **Supplementary Fig. 2**).

bioRxiv preprint doi: https://doi.org/10.1101/561340; this version posted May 15, 2019. The copyright holder for this preprint (which was not certified by peer review) is the author/funder. All rights reserved. No reuse allowed without permission.

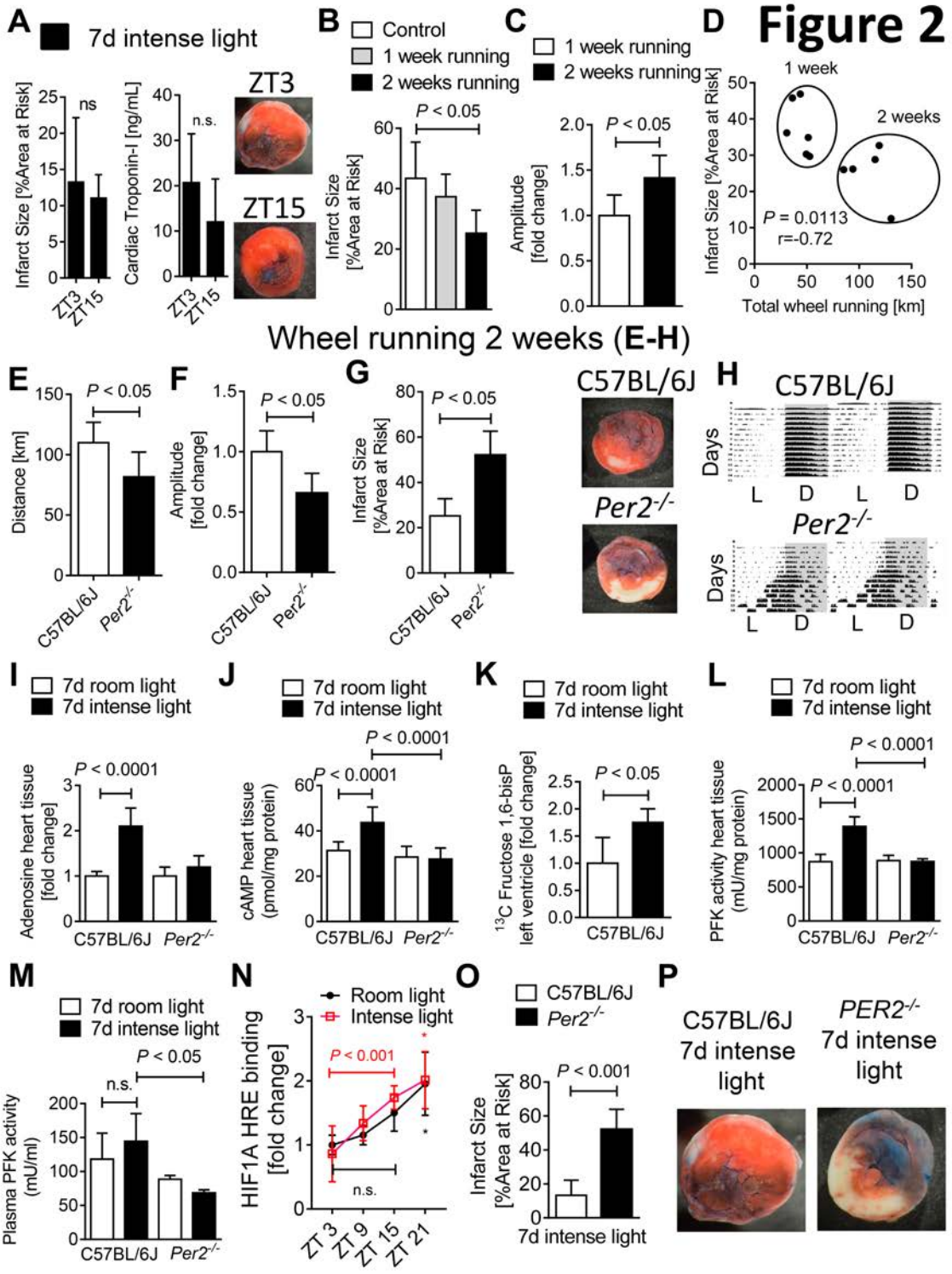

Figure 2. Intense light increases cardiac adenosine-cAMP and glycolytic flux via PER2 in the uninjured heart. **(A)** Infarct sizes in C57BL/6J mice that were housed under intense light (10,000 LUX, L:D 14:10 h) for 7 days and subjected to 60 min of *in situ* myocardial ischemia followed by 2h reperfusion at ZT3 or ZT15 (mean±SD; n=6). **(B-D)** C57BL/6J mice exposed

bioRxiv preprint doi: https://doi.org/10.1101/561340; this version posted May 15, 2019. The copyright holder for this preprint (which was not certified by peer review) is the author/funder. All rights reserved. No reuse allowed without permission.

to voluntary wheel running for 1 versus 2 weeks. Shown are infarct sizes after 60 min of myocardial ischemia and 2h reperfusion at ZT3 or circadian amplitude and distance walked measurements (mean±SD; n=6). (**E-H**) Wheel running measurements during or infarct size studies after 2 weeks of wheel running at ZT3 in C57BL/6J or *Per2*$^{-/-}$ mice (mean±SD; n=5). One representative infarct size staining and one wheel running activity recording are shown. **(I, J)** Adenosine measured by HPLC or cAMP determined by ELISA in heart tissue from C57BL/6J or *Per2*$^{-/-}$ mice at ZT3 after 7d of room- or intense light housing (mean±SD; n=5). **(K)** C57BL/6J mice were housed under intense light or standard room light (200 LUX, L:D 14:10 h) for 7 days followed by the infusion of 10 mg/kg/min U-^{13}C-glucose via an intra-arterial catheter over 90 minutes. Hearts were flushed with ice cold KCl and the left ventricle was shock frozen at ZT3 and analyzed by liquid chromatography–tandem mass spectrometry (mean±SD; n=4). (**L, M**) Phosphofructokinase (PFK) activity in both heart tissue and plasma samples from C57BL/6J or *Per2*$^{-/-}$ mice at ZT3 after 7d of room- or intense light housing (mean±SD; n=4-5). **(N)** HIF1A-hyoxi response element (HRE) binding was determined at ZT 3, 9, 15 and 21 (mean±SD; n=5) *Note:* * $P < 0.05$ for ZT21 vs. ZT3 in room light and intense light housed mice. **(O)** C57BL/6J or *Per2*$^{-/-}$ mice housed under intense light for 7 d prior to 60 min myocardial ischemia and 2 h reperfusion at ZT3. Infarct sizes are expressed as the percent of the area at risk that was exposed to myocardial ischemia (mean±SD; n=5). (**P**) Representative infarct staining.

bioRxiv preprint doi: https://doi.org/10.1101/561340; this version posted May 15, 2019. The copyright holder for this preprint (which was not certified by peer review) is the author/funder. All rights reserved. No reuse allowed without permission.

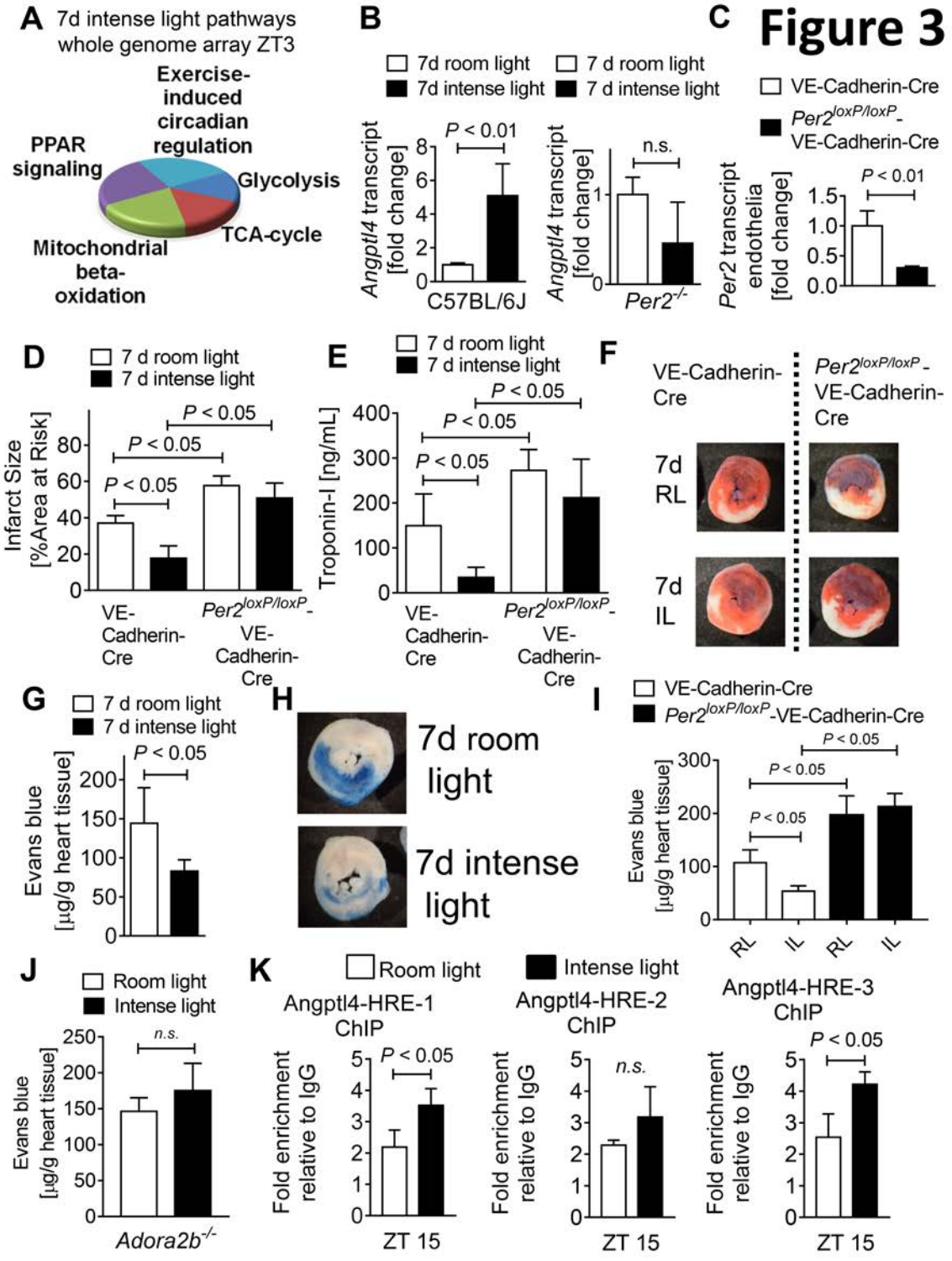

Figure 3. Intense light elicited cardioprotection is endothelial PER2 specific. (A) Whole genome array from C57BL/6J or *Per2*$^{-/-}$ heart tissue after 7d of intense light (10,000 LUX, L:D 14:10 h) or standard room light (200 LUX, L:D 14:10 h) housing at ZT3 (n=3 per group, total of 12 arrays). (**B**) Validation of transcript levels of the top light and PER2 dependent gene

bioRxiv preprint doi: https://doi.org/10.1101/561340; this version posted May 15, 2019. The copyright holder for this preprint (which was not certified by peer review) is the author/funder. All rights reserved. No reuse allowed without permission.

(ANGPTL-4) identified by whole genome array (mean±SD; n=4-5). (**C**) RT-PCR data showing *Per2* mRNA transcript levels from endothelial cells isolated from endothelial specific PER2 deficient (*Per2*$^{loxP/loxP}$-VE-Cadherin-Cre) or control (VE-Cadherin-Cre) hearts (mean±SD; n=3). (**D, E**) Infarct sizes or serum troponin-I in *Per2*$^{loxP/loxP}$-VE-Cadherin-Cre or VE-Cadherin-Cre mice housed under room- or intense light conditions for 7d followed by 60 min of *in situ* myocardial ischemia and 2h reperfusion at ZT3 (mean±SD; n=5). (**F**) Representative infarct staining. (**G- I**) Vascular leakage of Evans blue dye in C57BL/6J or *Per2*$^{loxP/loxP}$-VE-Cadherin-Cre after 60 min of *in situ* myocardial ischemia and 2h reperfusion at ZT3 following 7 days of room- or intense light housing (RL=room light, IL=intense light, mean±SD; n=5). (**J**) Vascular leakage of Evans blue dye in *Adora2b*$^{-/-}$ after 60 min of *in situ* myocardial ischemia and 2h reperfusion at ZT3 following 7 days of room- or intense light housing (mean±SD; n=5). (**K**) ChIP assay for HIF1A binding to the promoter region of Angptl4 in C57BL/6J following 7 days of room- or intense light housing (mean±SD; n=3).

bioRxiv preprint doi: https://doi.org/10.1101/561340; this version posted May 15, 2019. The copyright holder for this preprint (which was not certified by peer review) is the author/funder. All rights reserved. No reuse allowed without permission.

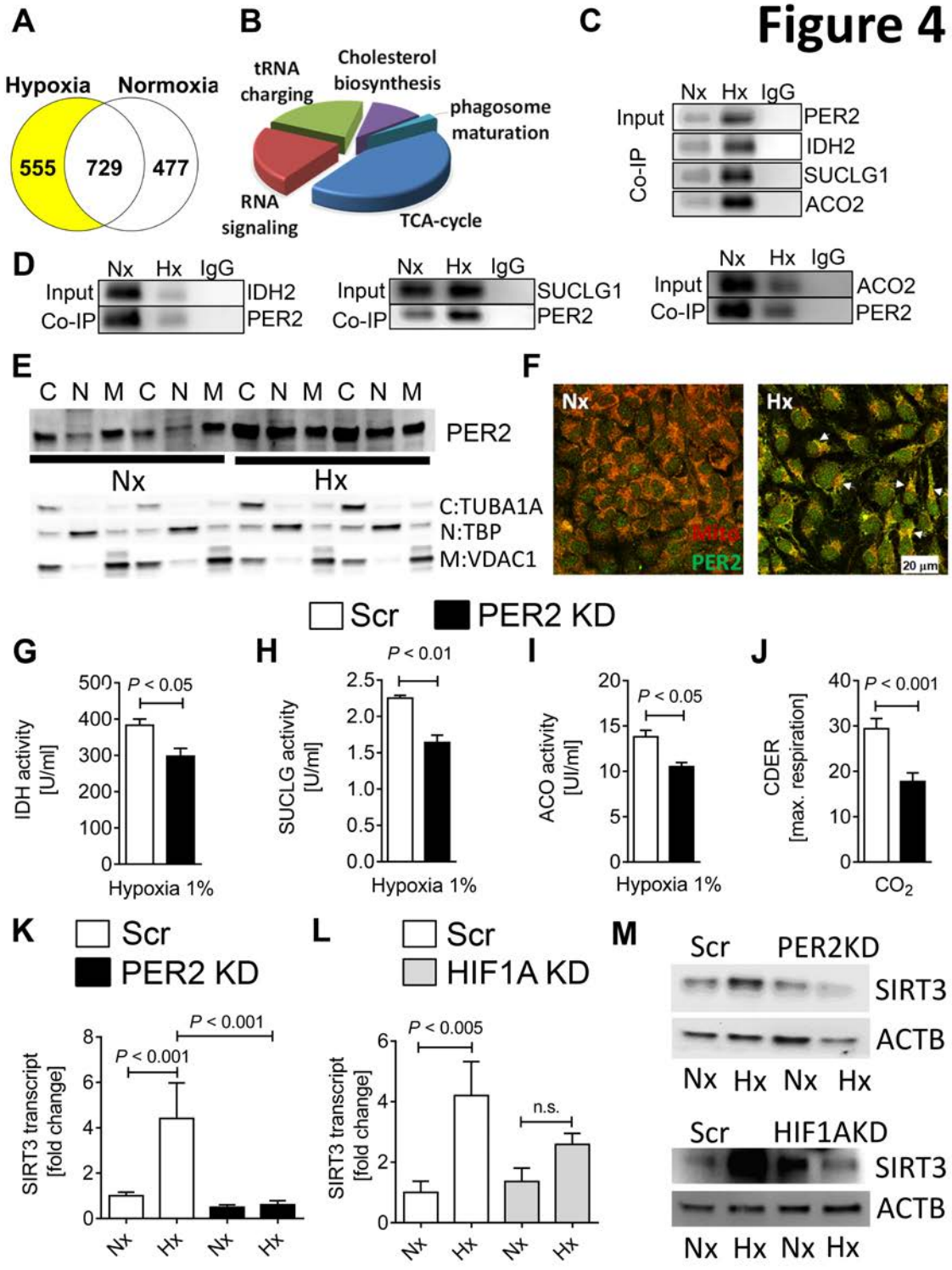

Figure 4. Identification of endothelial PER2 as a regulator of TCA cycle activity. HMEC-1 or stable lentiviral-mediated PER2KD and Scr control HMEC-1 were synchronized and exposed to 24h of normoxia (Nx) or 1% hypoxia (Hx). In a subset of experiments synchronized stable lentiviral-mediated HIF1AKD and Scr HMEC-1 were exposed to Nx or Hx. **(A-B)**

bioRxiv preprint doi: https://doi.org/10.1101/561340; this version posted May 15, 2019. The copyright holder for this preprint (which was not certified by peer review) is the author/funder. All rights reserved. No reuse allowed without permission.

Affinity purification-mass spectrometry-based proteomics screen for PER2 protein interactions in normoxic and hypoxic HMEC-1 (see also **Supplementary Fig. 8**). (**C, D**) Co-immunoprecipitation for PER2 in hypoxic or normoxic HMEC-1 against isocitrate dehydrogenase 2 (IDH2), succinyl Co-A ligase (SUCLG1) and aconitase (ACO2) and vice versa. One representative blot of three is displayed. (**E**) Subcellular compartment analysis of PER2 during normoxia or hypoxia (C= cytoplasm, N=nucleus, M=mitochondria; compartment-specific loading controls: Tubulin Alpha 1a (TUBA1A) for cytoplasm, TATA-Box Binding Protein (TBP) for nucleus and Voltage-Dependent Anion Channel 1 (VDAC1) for mitochondria). (**F**) Translocation of PER2 into the mitochondria during hypoxia (see also **Supplementary Fig. 9)**. **(G-I)** TCA cycle enzyme activities of IDH, SUCLG and ACO from stable lentiviral-mediated PER2KD and Scr control HMEC-1 during hypoxia (mean±SD, n=3). **(J)** Carbon dioxide evolution rates (CDER), as a surrogate for TCA cycle function, in PER2 KD or Scr HMEC-1 measured by a mitochondrial stress test using a Seahorse XF24 FluxPak assay (mean±SD, n=5). (**K-M**) SIRT3 transcript or protein levels from stable lentiviral-mediated PER2KD and Scr or stable lentiviral-mediated HIF1AKD and Scr control HMEC-1 (mean±SD, n=3, see also **Supplementary Fig. 10**).

bioRxiv preprint doi: https://doi.org/10.1101/561340; this version posted May 15, 2019. The copyright holder for this preprint (which was not certified by peer review) is the author/funder. All rights reserved. No reuse allowed without permission.

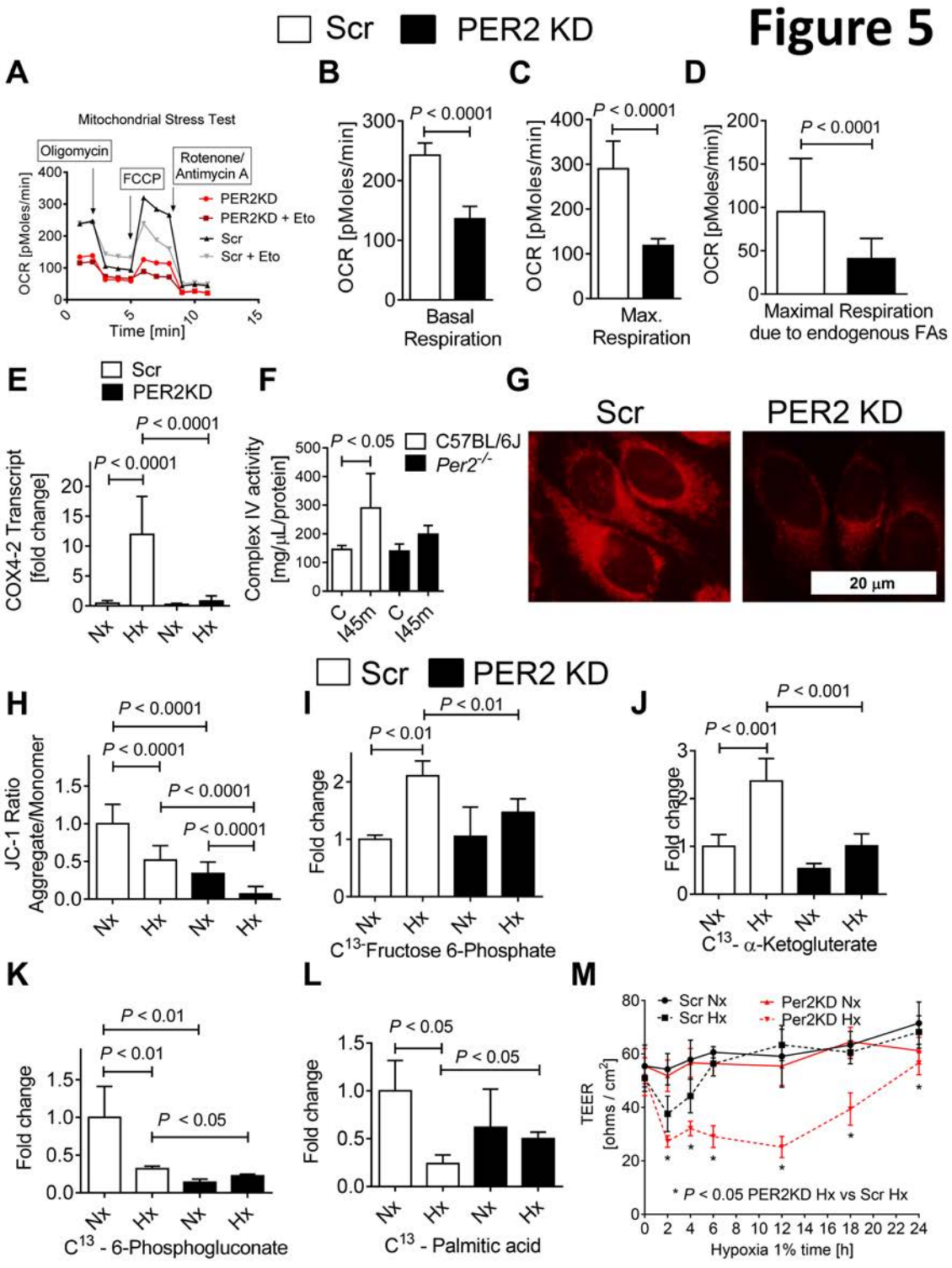

Figure 5. Endothelial PER2 regulates mitochondrial function via HIF1A-COX4.2. (A-D) Oxygen consumption rates (OCR) measured by a mitochondrial stress test kit on a Seahorse Biosciences XF24 analyzer in PER2KD or Scr HMEC-1 with or without the irreversible carnitine palmitoyltransferase-1 inhibitor etomoxir (Eto). Quantification of basal respiration,

bioRxiv preprint doi: https://doi.org/10.1101/561340; this version posted May 15, 2019. The copyright holder for this preprint (which was not certified by peer review) is the author/funder. All rights reserved. No reuse allowed without permission.

maximum achievable respiration, and maximal respiration due to endogenous fatty acid are shown (mean±SD, n=5, see also **Supplementary Fig. 11**). **(E**) COX4.2 transcript levels in PER2 KD or Scr HMEC-1 after 24h of Nx or 1% Hx treatment (mean±SD, n=6). **(F)** Complex IV enzyme activity in *Per2*$^{-/-}$ or C57BL/6 mouse hearts subjected to 45 min of ischemia (mean±SD, n=4). **(G)** MitoTracker Red CMXRos staining of PER2 KD or Scr HMEC-1 at baseline. One representative image of 5 is shown (see also **Supplementary Fig. 12** for a corresponding cell energy phenotype assay). **(h)** Quantification of the mitochondrial membrane potential probe JC-1(mean±SD, n=6; see also **Supplementary Fig. 13**). **(I-K)** U-^{13}C-glucose was added to the supernatant of PER2 KD or Scr HMEC-1. Following 24h of Nx or 1% Hx treatment cells were harvested and analyzed for ^{13}C-metabolites using liquid chromatography-tandem mass spectrometry. Data are presented as percentage of total metabolite present (mean±SD, n=3). **(L)** 1,2-^{13}C-palmitic acid tracers in PER2 KD or Scr HMEC-1 in 24 h Nx or 1% Hx (mean±SD, n=3). (**M**) Permeability assay in PER2 KD or Scr HMEC-1 during 24h of 1% hypoxia (mean±SD, n=5). *Note:* Permeability increases after prolonged hypoxia exposure of endothelial cells due to morphological changes (Am. J. Physiol. 269 (Lung Cell. Mol. Physiol. 13): L52- L58, 1995.)

bioRxiv preprint doi: https://doi.org/10.1101/561340; this version posted May 15, 2019. The copyright holder for this preprint (which was not certified by peer review) is the author/funder. All rights reserved. No reuse allowed without permission.

Figure 6

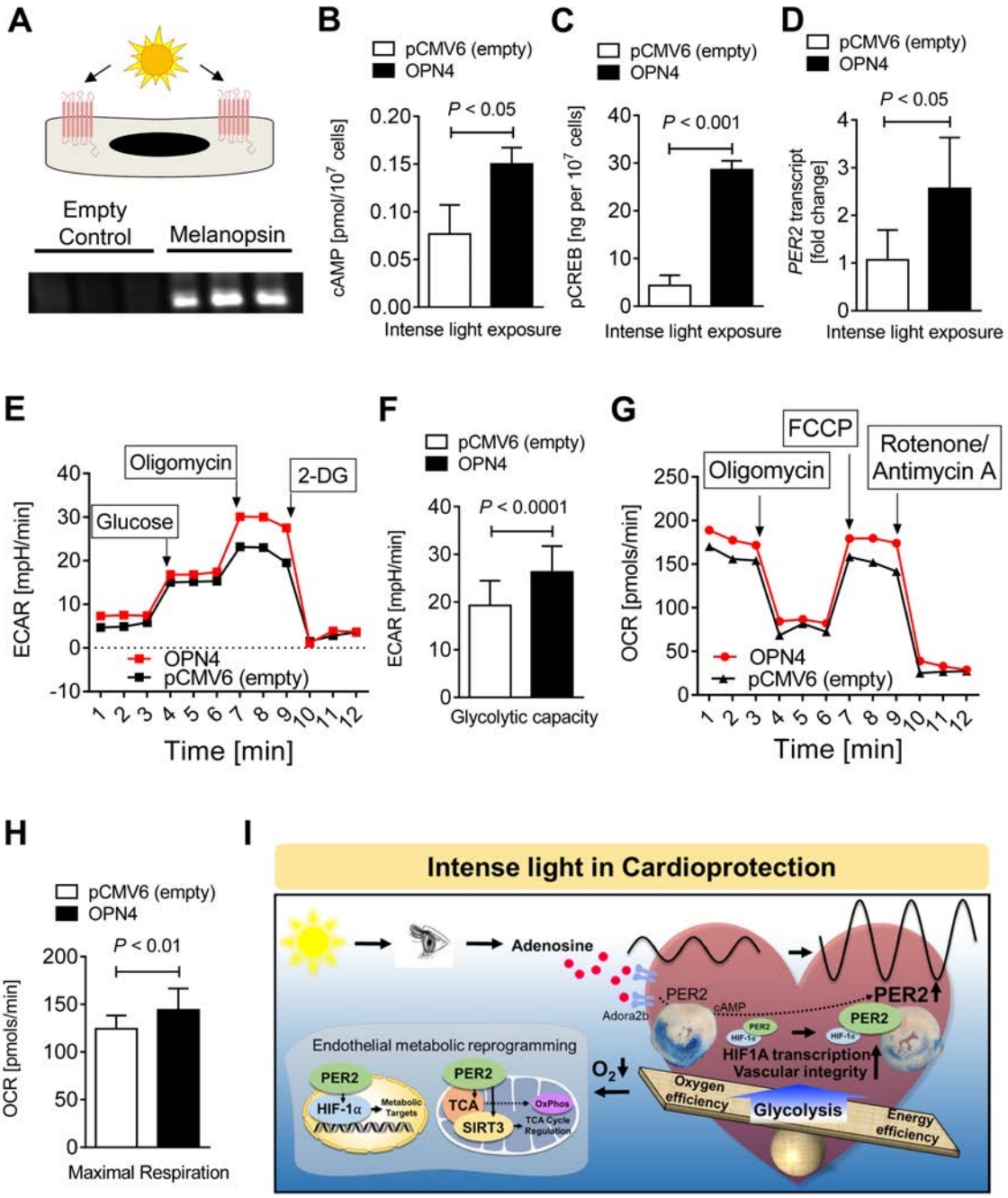

Figure 6. Light-sensing human cell line recapitulates *in vivo* light exposure. (**A**) Study design and verification of melanopsin overexpression by immunoblot. pCMV6 is the empty vector control, and OPN4-pCMV6 is the plasmid containing the gene encoding melanopsin (n=3). (**B-H**) cAMP, pCREB levels, PER2 transcript, glycolytic capacity, and maximum

bioRxiv preprint doi: https://doi.org/10.1101/561340; this version posted May 15, 2019. The copyright holder for this preprint (which was not certified by peer review) is the author/funder. All rights reserved. No reuse allowed without permission.

achievable respiration after light-sensing cells were exposed to intense light (mean±SD, n=6-10). (**I**) Schematic model.

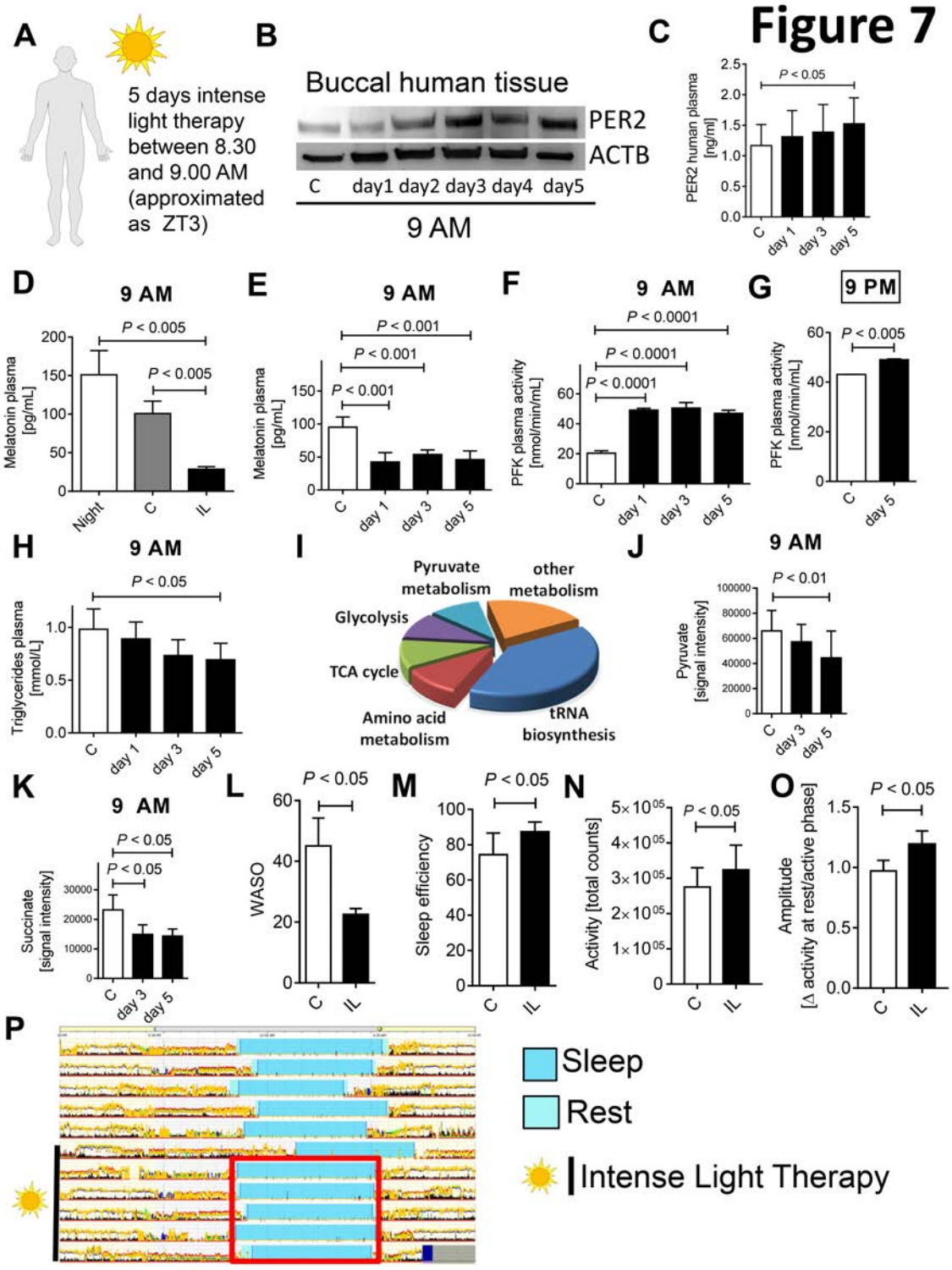

Figure 7. Intense light enhances the circadian amplitude of PER2 and activates PER2 metabolism in humans. **(A)** Protocol for intense light exposure experiments in healthy human volunteers. 20 healthy volunteers (11 female and 6 male, age range between 21-44 yrs.) were

bioRxiv preprint doi: https://doi.org/10.1101/561340; this version posted May 15, 2019. The copyright holder for this preprint (which was not certified by peer review) is the author/funder. All rights reserved. No reuse allowed without permission.

exposed to intense light (10,000 LUX) from 8.30-9.00 AM on 5 consecutive days. **(B, C**) PER2 protein levels from buccal tissue or plasma samples at 9AM during 5d of intense light exposure assessed by immunoblot or ELISA, respectively (mean±SD; n=6, see also **Supplementary Fig. 15**). **(D)** Effect of room light versus intense light on human plasma melatonin levels (mean±SD; n=3-6). (**E**) Longitudinal monitoring of human plasma melatonin levels during 5d of intense light exposure at 9AM (mean±SD; n=3-6). **(F)** Human plasma phosphofructokinase (PFK) activity during 5d of intense light exposure at 9AM (mean±SD; n=3-6). (**G**) Human plasma PFK activity after 5d of intense light exposure at 9PM (mean±SD; n=3). **(H)** Human plasma triglyceride levels during 5 d of intense light exposure at 9 AM (mean±SD; n=8). **(I-K)** Targeted metabolomics using mass-spectrometry on human plasma samples from healthy volunteers exposed to intense light therapy for 5 days. Key metabolites of glycolysis (pyruvate) or TCA cycle (succinate) are shown for day 3 and day 5 of intense light therapy (mean±SD; n=3, see also **Supplementary Fig. 16**). **(L-P)** Actigraphy data using a validated accelerometer (Actiwatch 2). Shown are the wake-up episodes after the sleep onset (WASO, **L**), the sleep efficiency (**M**), day activity (**N**), the circadian amplitude (**O**, mean±SD; n=6), and one representative actigraphy recording from one healthy volunteer before and during intense light therapy (**Note**: synchronized sleep phases [turquoise bar] during intense light exposure [red square]; see also **Supplementary Figure 17**). C=control subjects prior to any light exposure, IL=intense light.

bioRxiv preprint doi: https://doi.org/10.1101/561340; this version posted May 15, 2019. The copyright holder for this preprint (which was not certified by peer review) is the author/funder. All rights reserved. No reuse allowed without permission.

Sup. Figure 1

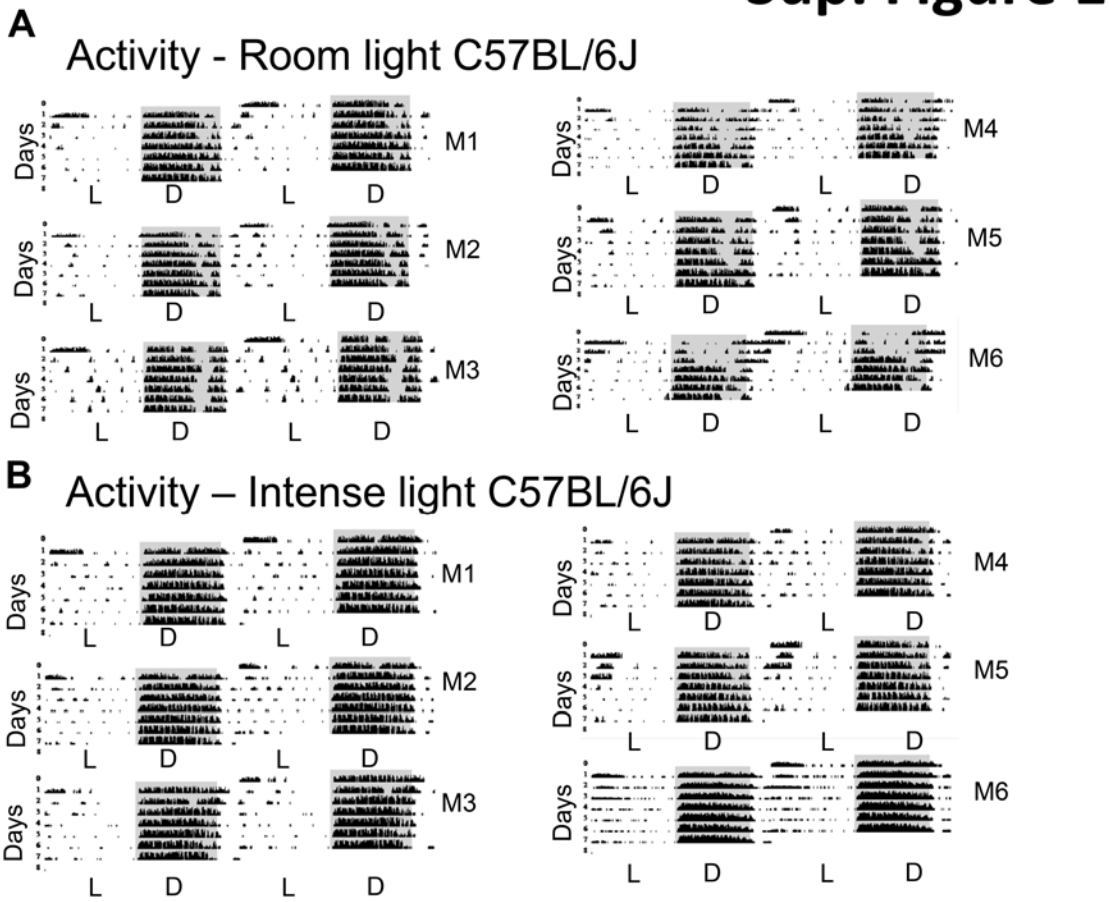

Supplementary Figure 1. (A, B) 7 day wheel running activity graphs from wildtype mice exposed to 7 days room light versus 7 days intense light (mean±SD, n=6, M=mouse, L=light phase, D=dark phase, double-plotted actograms, ***Note***: numbers on the left indicate days).

bioRxiv preprint doi: https://doi.org/10.1101/561340; this version posted May 15, 2019. The copyright holder for this preprint (which was not certified by peer review) is the author/funder. All rights reserved. No reuse allowed without permission.

Sup. Figure 2

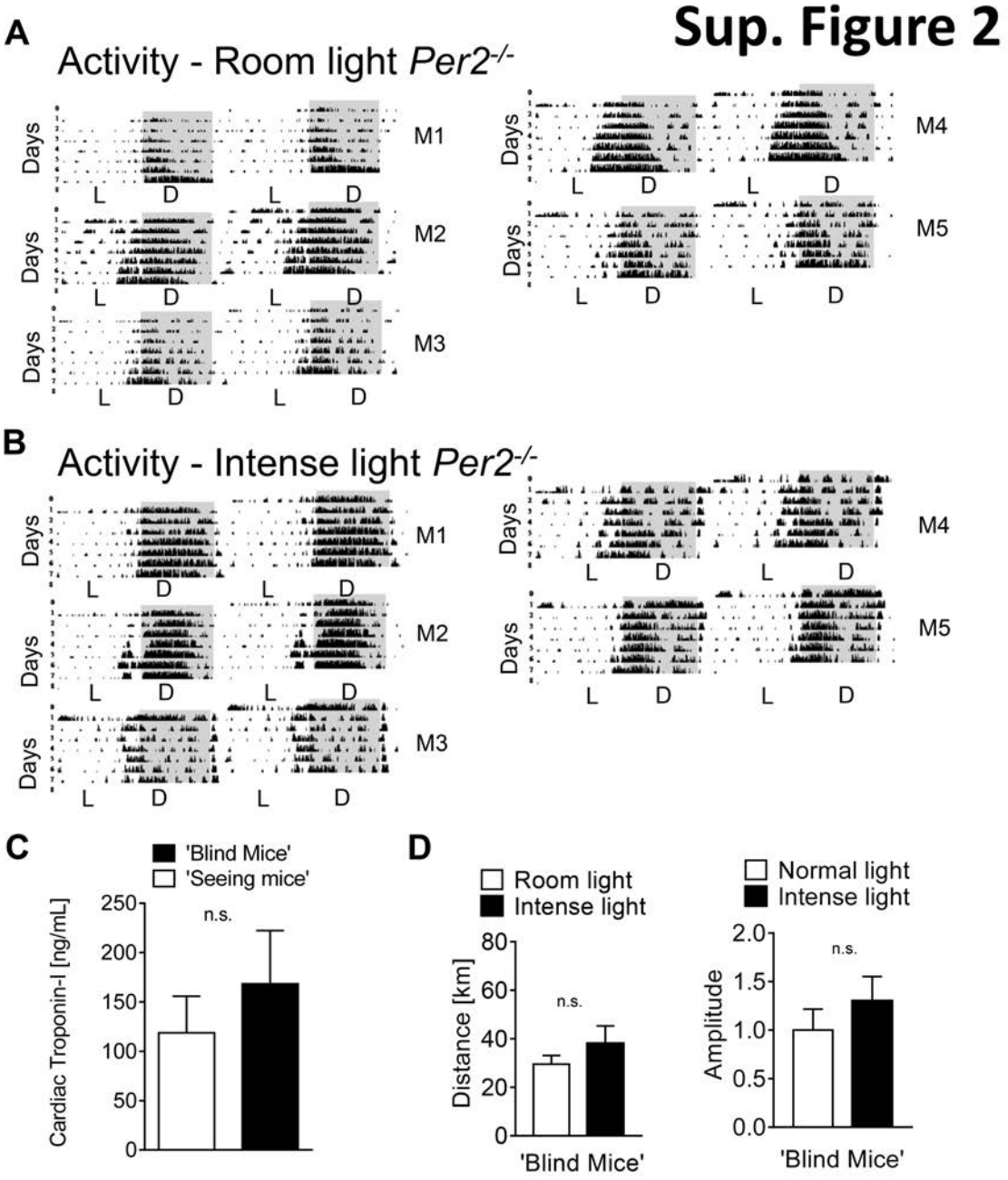

Supplementary Figure 2. (A, B) Wheel running activity graphs from *Per2*$^{-/-}$ mice exposed to 7 days room light versus 7 days intense light (mean±SD, n=5, M=mouse, L=light phase, D=dark phase, double-plotted actograms). **(C)** Cumulative cardiac troponin measurements (ZT3+ZT15) from 'seeing' compared to enucleated 'blind' wildtype mice subjected to 60 min ischemia and 2 h reperfusion (mean±SD, n=7); (**D**) Wheel running measurements during 7 days of room light or intense light housing conditions in 'blind' C57BL/6J mice (mean±SD; n=4).

bioRxiv preprint doi: https://doi.org/10.1101/561340; this version posted May 15, 2019. The copyright holder for this preprint (which was not certified by peer review) is the author/funder. All rights reserved. No reuse allowed without permission.

Sup. Figure 3

A

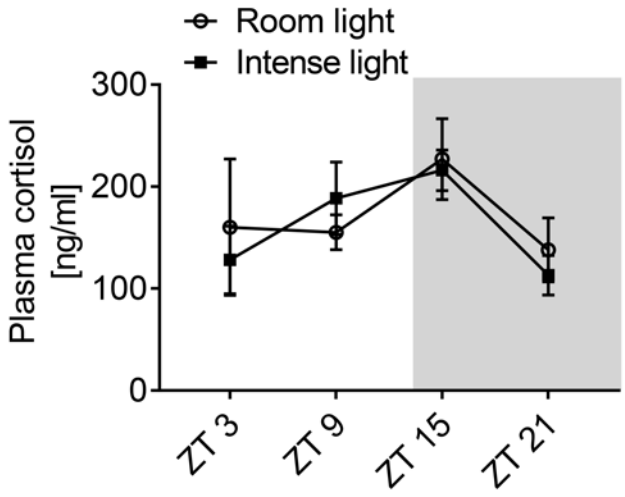

B

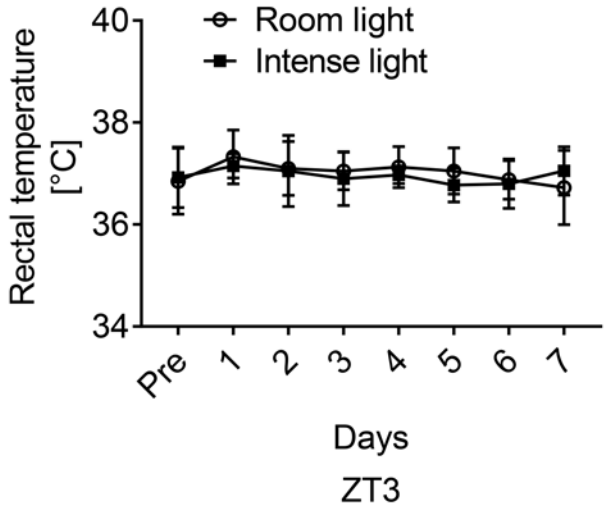

Supplementary Figure 3. (**A**) Plasma cortisol levels after 7 days of room or intense light exposure (mean±SD, n=5, (**B**) Rectal temperatures during 7 days of room light or intense light at ZT3 (mean±SD; n=4).

bioRxiv preprint doi: https://doi.org/10.1101/561340; this version posted May 15, 2019. The copyright holder for this preprint (which was not certified by peer review) is the author/funder. All rights reserved. No reuse allowed without permission.

Sup. Figure 4

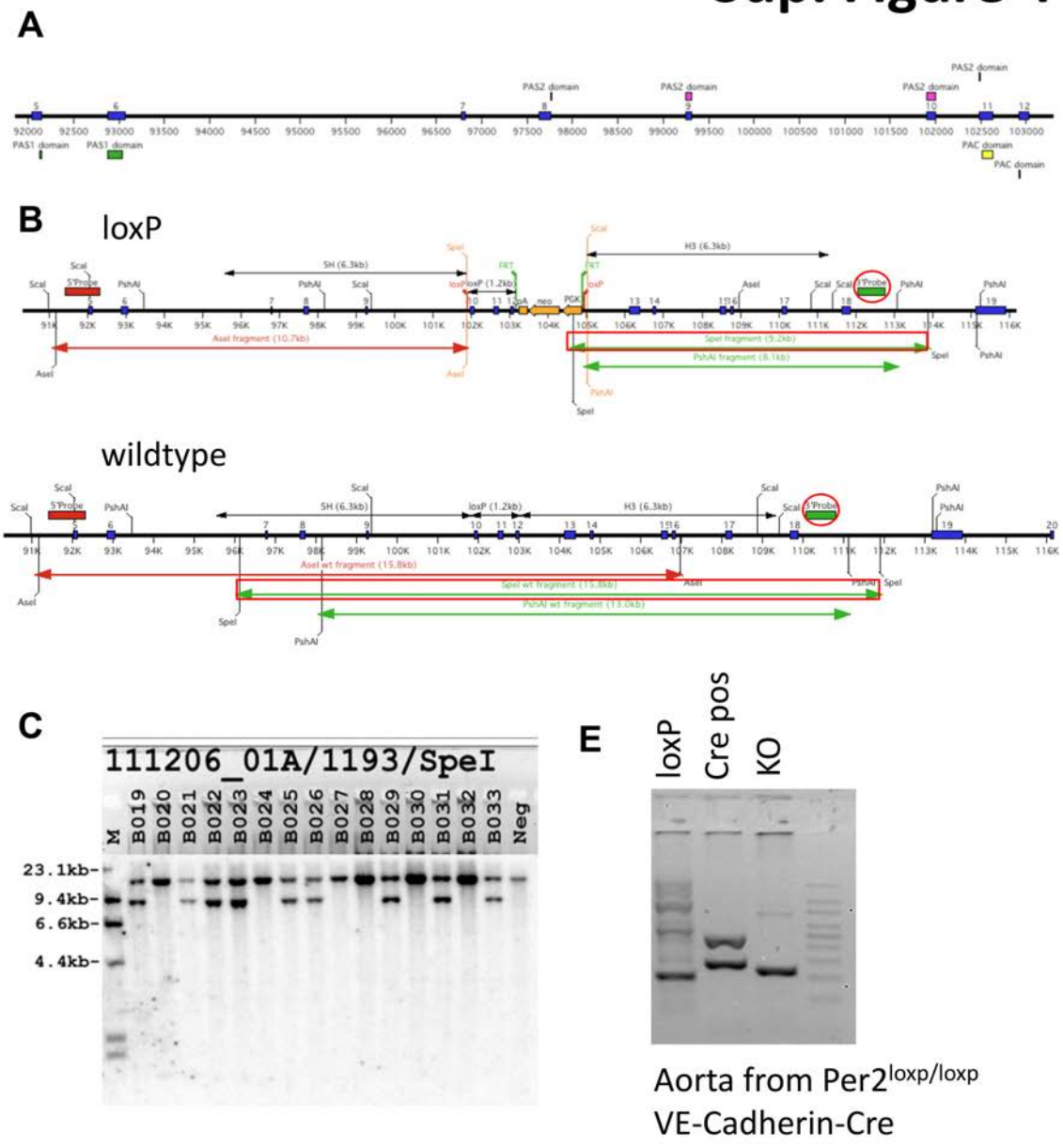

Supplementary Figure 4. (A) *Per2*$^{loxp/loxp}$ -strategy: deletion of exons 10, 11 and 12 in the *Per2* gene removes half of the PAS2 domain and all of the PAC domain. This deletion also results in a frameshift mutation introducing an early stop codon. **(B)** Screening strategy. (**C**) Screening: DNA was digested with SpeI and probed with the P3 probe. These mice were the result of a wt (wildtype) /loxP x C57BL/6J mating. The expected sizes were: wildtype 15.8kb and loxP 9.2kb. Correct integration was confirmed by full sequencing. (**D**) PCR-Genotyping of aorta from a *Per2*$^{loxP/loxP}$ -VE-Cadherin-Cre mouse.

bioRxiv preprint doi: https://doi.org/10.1101/561340; this version posted May 15, 2019. The copyright holder for this preprint (which was not certified by peer review) is the author/funder. All rights reserved. No reuse allowed without permission.

Sup. Figure 5

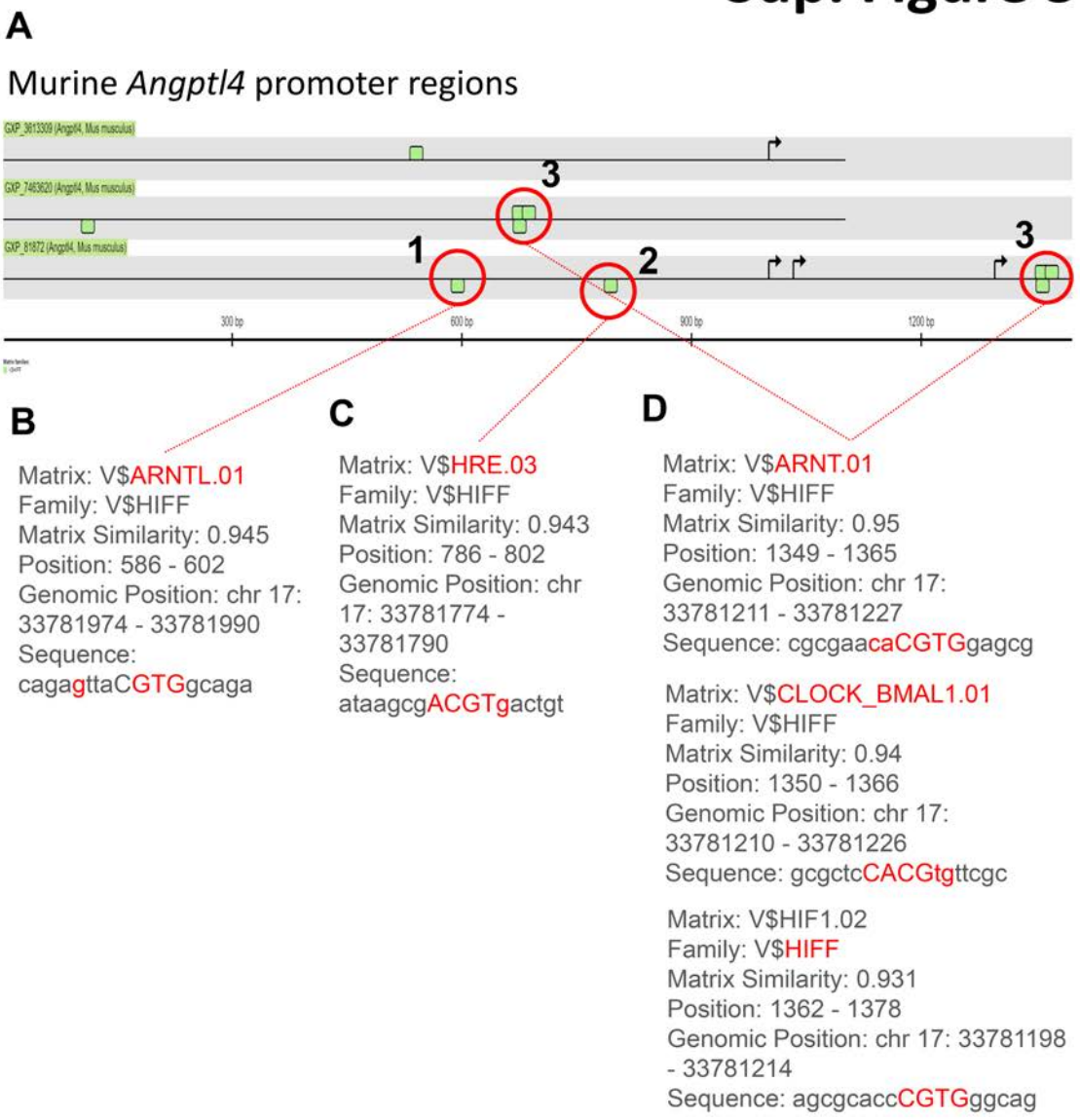

Supplementary Figure 5. (A) Mouse *Anptl4* promotor regions (Genomatix). HIFF family binding sites are depicted by green boxes. (**B-D**) Primers for the ChIP assay covered the regions marked with a red circle (*Angptl4*-HRE1-3, **see Figure 3**).

bioRxiv preprint doi: https://doi.org/10.1101/561340; this version posted May 15, 2019. The copyright holder for this preprint (which was not certified by peer review) is the author/funder. All rights reserved. No reuse allowed without permission.

Sup. Figure 6

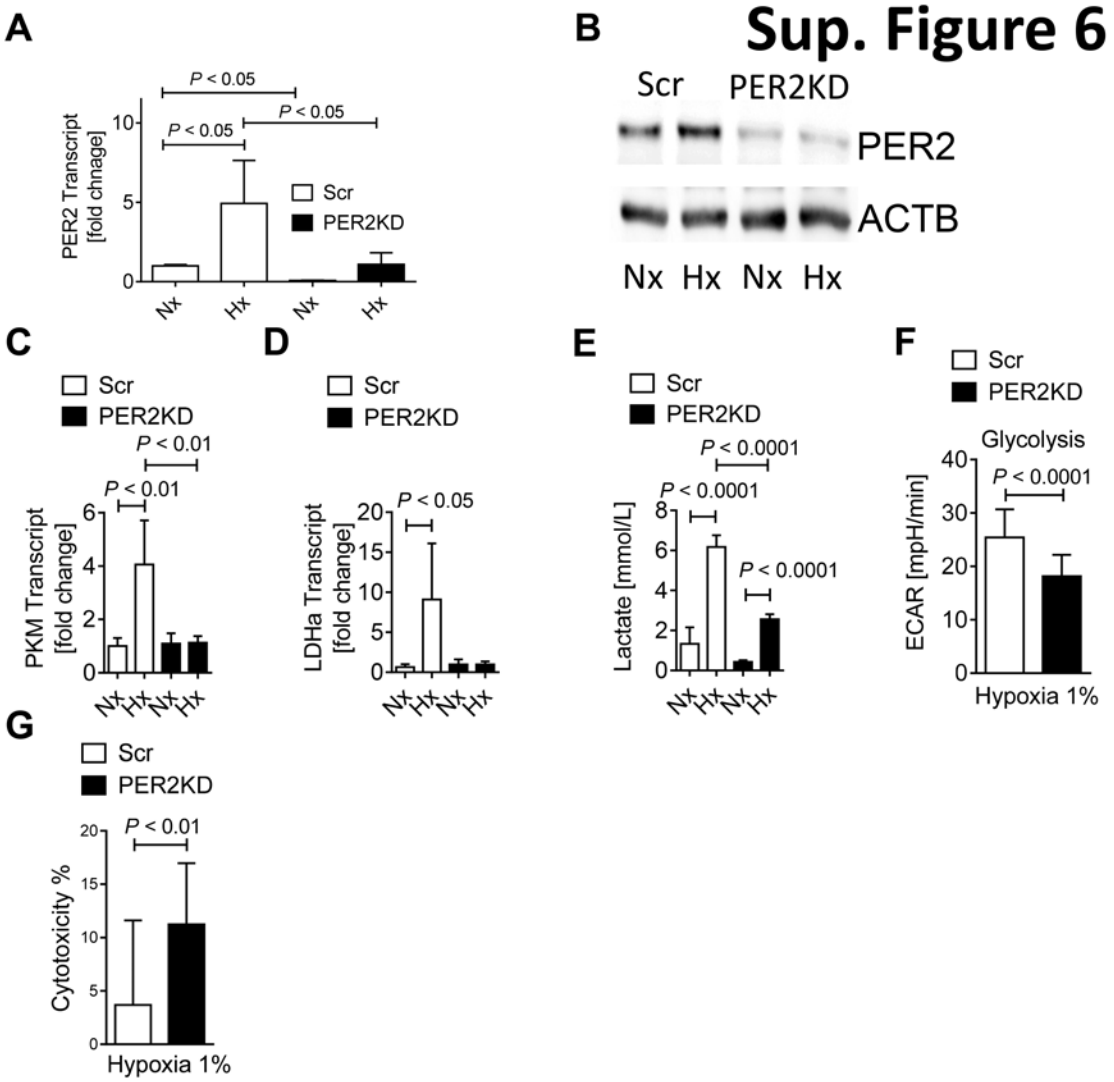

Supplementary Figure 6. HMEC-1 controls (Scr; treated with lentiviral scrambled shRNA) or HMEC-1 PER2 knockdown (KD; treated with lentiviral PER2 shRNA) were synchronized via serum starvation and exposed to 24 h of normoxia (Nx) or 1% hypoxia (Hx) in all experiments. (**A, B**) PER2 transcript or protein levels from stable lentiviral mediated PER2KD or Scr control HMEC-1were determined by real-time RT-PCR relative to housekeeping gene beta-actin or immunoblot analysis of PER2 protein, respectively (mean±SD, n=3). (**C, D**) Transcript expression of pyruvate kinase (PKM) or lactate dehydrogenase (LDHa) in stable lentiviral mediated PER2KD HMEC-1 or controls (Scr, mean±SD, n=3). (**E**) Lactate levels in supernatants obtained from HMEC-1 with a lentiviral-mediated PER2KD HMEC-1 or controls (Scr; mean±SD, n=3). (**F**) Glucose metabolism from stable lentiviral mediated PER2KD or Scr control HMEC-1 after 24h at 1% hypoxia. Glycolysis assay was performed using a glycolytic stress test kit on a Seahorse Biosciences XF24 analyzer. (**G**) LDH-Cytotoxicity assay from HMEC-1 with a lentiviral-mediated PER2KD or controls (Scr, mean±SD, n=10).

bioRxiv preprint doi: https://doi.org/10.1101/561340; this version posted May 15, 2019. The copyright holder for this preprint (which was not certified by peer review) is the author/funder. All rights reserved. No reuse allowed without permission.

Sup. Figure 7

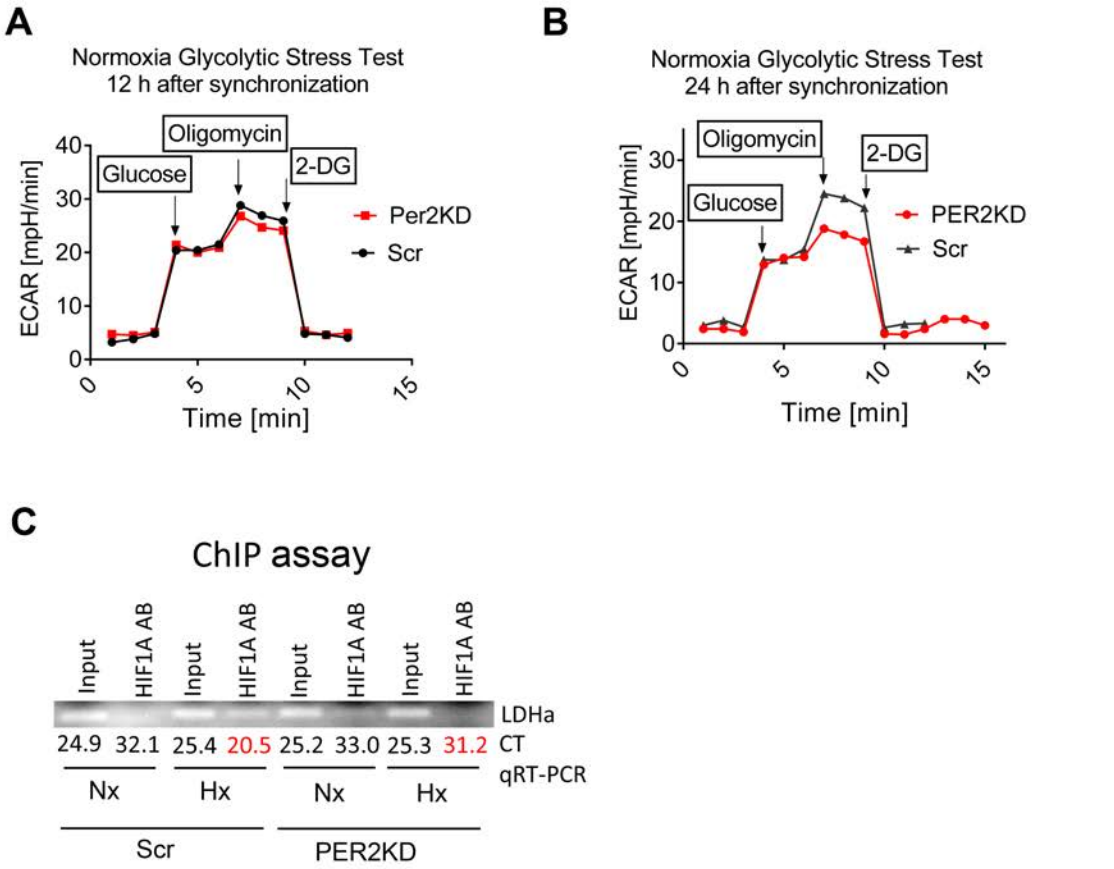

Supplementary Figure 7. HMEC-1 controls (Scr; treated with lentiviral scrambled shRNA) or HMEC-1 PER2 knockdown (KD; treated with lentiviral PER2 shRNA) were synchronized via serum starvation and exposed to 24 h of normoxia (Nx) or 1% hypoxia (Hx (**A, B**) Glycolytic stress tests using a Seahorse Bioanalyzer 12 or 24h after cell synchronization (mean±SD, n=10) under normoxic conditions. (**C**) Chromatin immunoprecipitation analysis to detect HIF1A protein binding to the human LDHa promoter using lentiviral-mediated PER2KD HMEC-1 or controls ([scrambled] Scr). qRT-PCR for the human LDHa promoter was performed for quantification. PCR products analyzed on a 2% agarose gel (top, **not** quantitative) or qunatitaive CT values form the qRT-PCR are shown (bottom, n=3).

bioRxiv preprint doi: https://doi.org/10.1101/561340; this version posted May 15, 2019. The copyright holder for this preprint (which was not certified by peer review) is the author/funder. All rights reserved. No reuse allowed without permission.

Sup. Figure 8

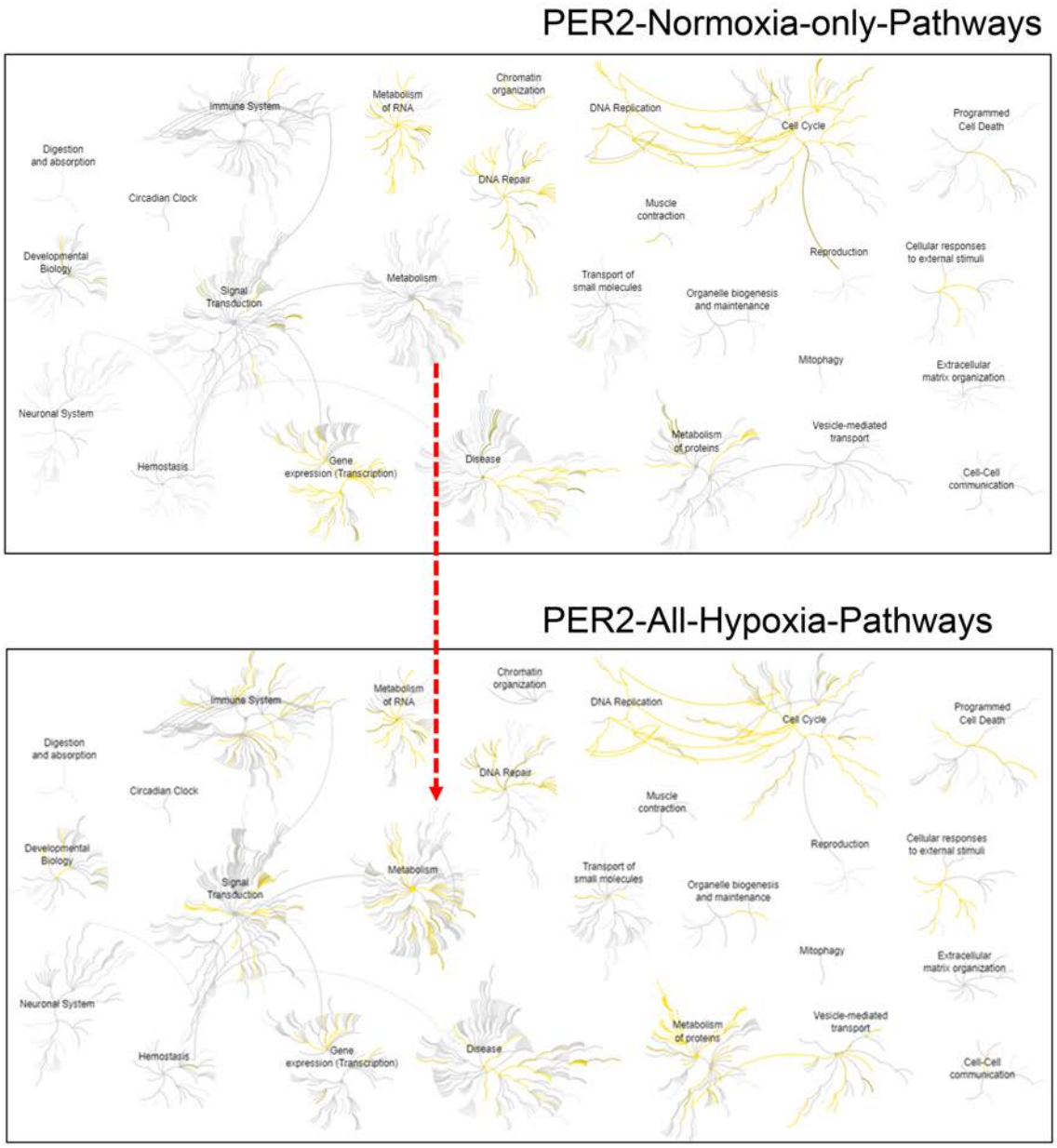

Supplementary Figure 8. PER2-Normoxia-Hypoxia-Pathways. *Reactome* analysis of an affinity purification–mass spectrometry based proteomics from hypoxic HMEC-1 cells, indicating as strong involvement of PER2 in metabolic pathways under hypoxia. Yellow depicts PER2 pathways in comparison to all available *Reactome* pathways (grey).

bioRxiv preprint doi: https://doi.org/10.1101/561340; this version posted May 15, 2019. The copyright holder for this preprint (which was not certified by peer review) is the author/funder. All rights reserved. No reuse allowed without permission.

Sup. Figure 9

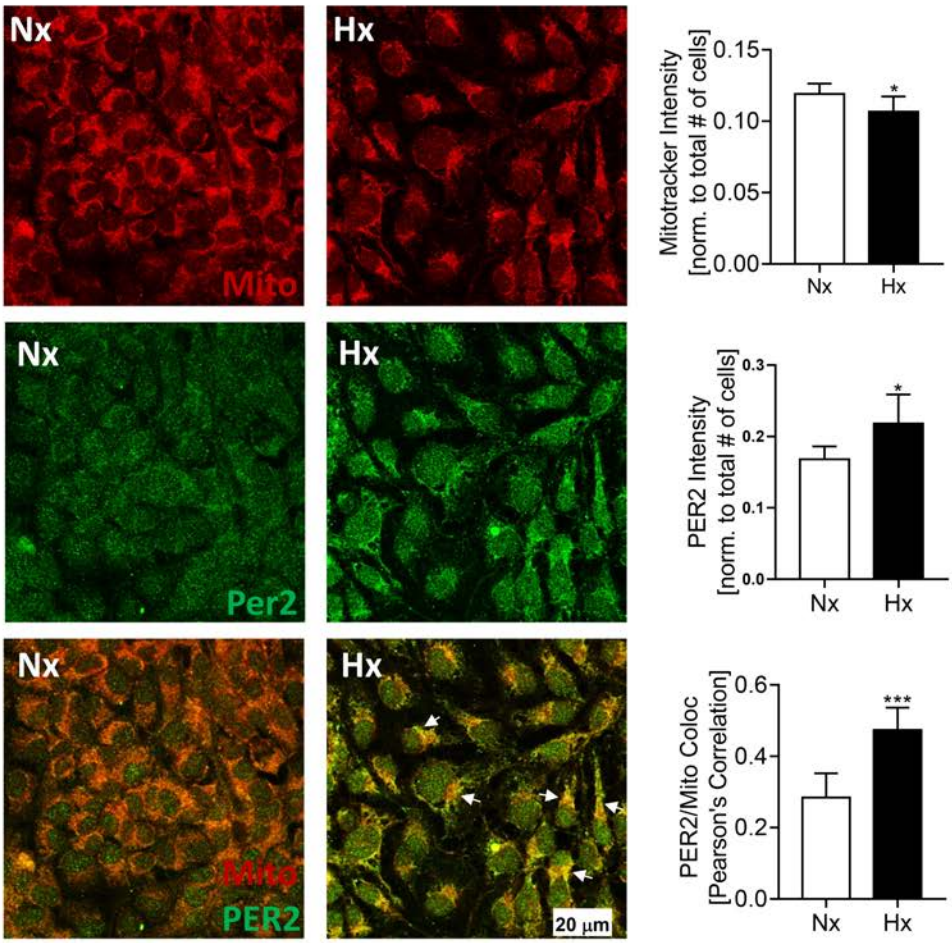

Supplementary Figure 9. Colocalization of PER2 and mitochondria (upper panel: MitoTracker Red CMXRos staining (red), middle panel: PER2 staining (green), lower panel: overlay MitoTracker Red and PER2 staining). Shown are stainings from HMEC-1 cells after 24h of normoxia or 24h of hypoxia 1%. White arrows indicate mitochdrial translocation of PER2 (yellow, mean±SD, n=6, *=P<0.05, ***= P<0.001).

bioRxiv preprint doi: https://doi.org/10.1101/561340; this version posted May 15, 2019. The copyright holder for this preprint (which was not certified by peer review) is the author/funder. All rights reserved. No reuse allowed without permission.

Sup. Figure 10

A

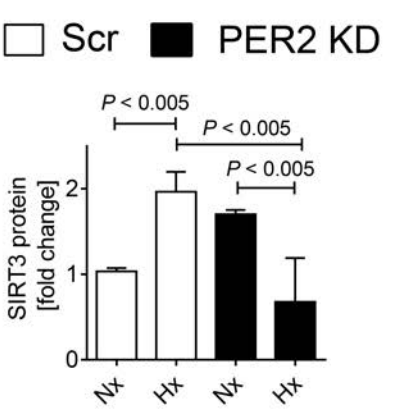

B

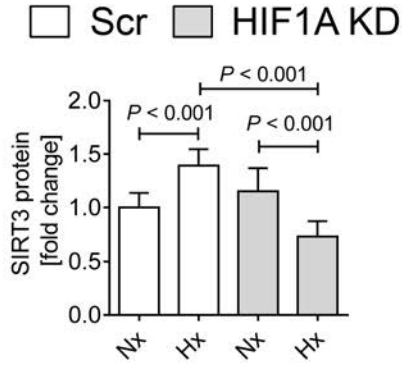

C

SIRT3 promoter with HRE binding site

```
Promoter 2
>FP014148 SIRT3_2              :+U  EU:NC; range  -499 to   100.
TTCGAGGTATTTTGGGCAAGGACAAGCACTTCTTGCGTGTTCGTTGTCGACACCTCGCCC
ACTCTTTCTCACCTTGCCGTGTTTCCTTTGCGGCATGTCTGGGAGTTTACGTGCGTTCCA
ACACCGGGGCCTCCGTCTTTATGCTGATCTGTGGACGTCACTTATGGGGGTTTTGTCGTT
TATTTCACCATTCCCTCATTGAAATACGTTCTAACCTTTAGTTATTGTGCATCATGCTGT
GGTGAATAACCTTGTTGGCACCTCACTGTTTGCATAAATTCCTAGTACTGGGATTGCTAG
GTCCAAAAGTATATGCATTTAACGCTTTAATGATCCCTCATAAATGTTGTGCGGTTAATA
CTCCCACTGGCATGTGATCGTACCCGTCTCCATAGTAATTGCATCTAAGAACTGAGGCTA
CATAGGAAAAAATCTTAAGGTCCATGGTTGTTAGGTATCAGATGCCCTATAATGGATGAA
TATTTAAGTAAATAATGGCACATTGACTTGCTGTCTGACACAACTGCTGAAAATGTTGGT
GAAAAGTGAGTCTCGAAGTGGTAGCTCACACTTGTAATACCAGCACTTTCGGAGGCTGAG
```

Supplementary Figure 10. (A) Quantification of SIRT3 protein from PER2 KD or Scr control HMEC-1 in Hx (hypoxia 1%) or Nx (normoxia). SIRT3 protein calculated based on fold change (mean±SD, n=5). **(B)** Quantification of SIRT3 protein from HIF1A KD or Scr control HMEC-1s in Hx or Nx. SIRT3 protein calculated based on fold change (mean±SD, n=5). **(C)** Region of the human SIRT3 promoter containing a hypoxia response element (HRE) binding site (red).

bioRxiv preprint doi: https://doi.org/10.1101/561340; this version posted May 15, 2019. The copyright holder for this preprint (which was not certified by peer review) is the author/funder. All rights reserved. No reuse allowed without permission.

Sup. Figure 11

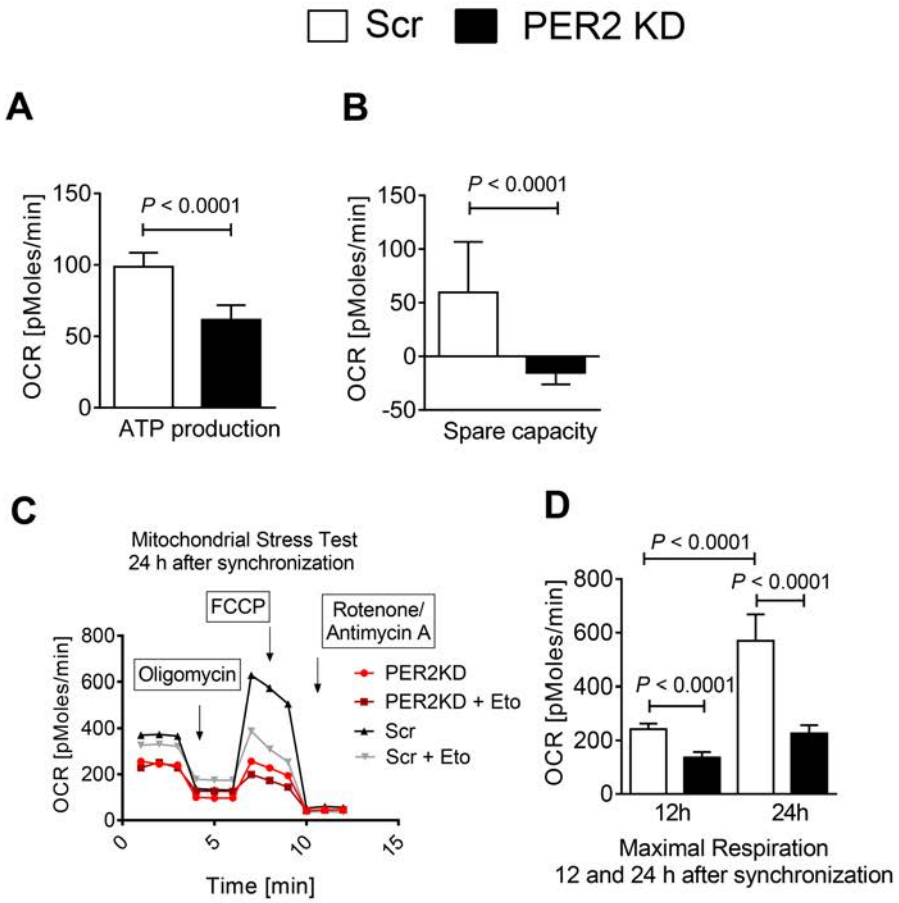

Supplementary Figure 11. (A, B) Mitochondrial stress test assayed using the Seahorse Bioanalyzer in PER2 KD or Scr control HMEC-1 measuring ATP production and spare capacity 12 h after cell synchronization (mean±SD, n=10). **(C, D)** Fatty acid oxidation mitochondrial stress test administered at 24h after cell synchronization in PER2 KD or Scr control cells (mean±SD, n=5). Differences in maximal respiration between time point 12 and 24h are quantified.

bioRxiv preprint doi: https://doi.org/10.1101/561340; this version posted May 15, 2019. The copyright holder for this preprint (which was not certified by peer review) is the author/funder. All rights reserved. No reuse allowed without permission.

Sup. Figure 12

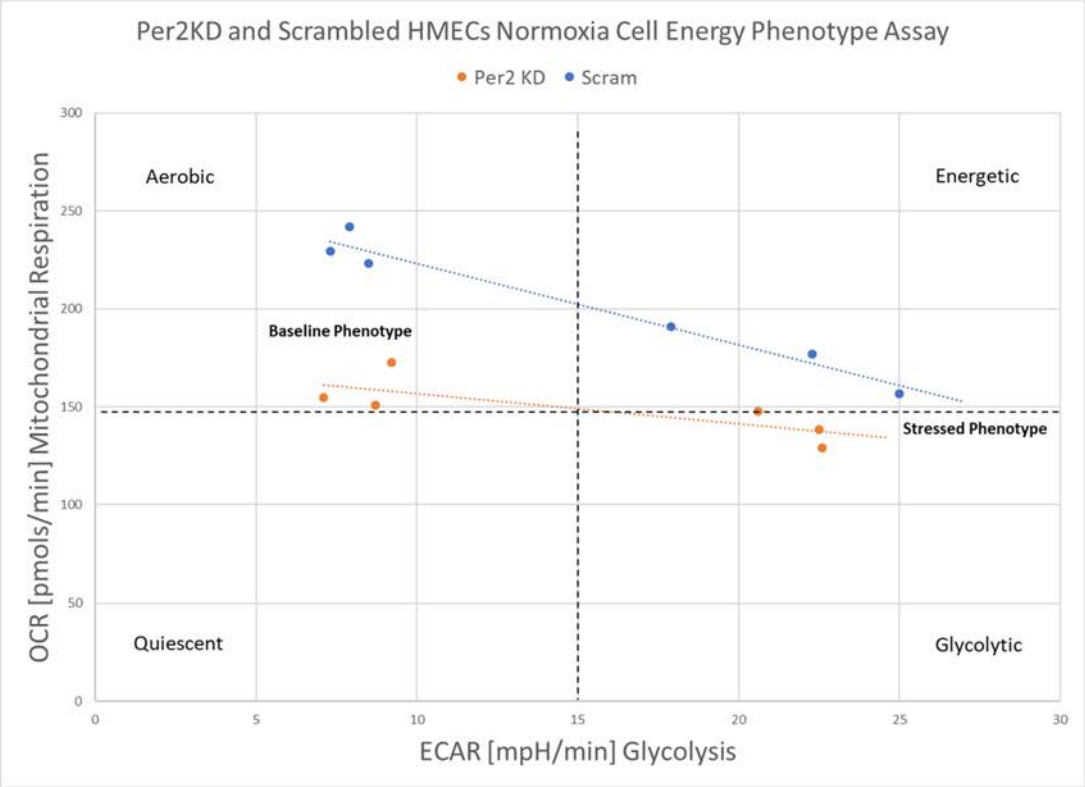

Supplementary Figure 12. Cell energy phenotype test using the Seahorse Bioanalyzer in PER2 KD or Scram control HMEC-1 at baseline. Quiescent phenotype = cell not energetic for either metabolic pathway; energetic phenotype = cell uses both metabolic pathways; aerobic phenotype = cell uses predominantly mitochondrial respiration; and glycolytic = cell uses predominantly glycolysis (mean±SD, n=10).

bioRxiv preprint doi: https://doi.org/10.1101/561340; this version posted May 15, 2019. The copyright holder for this preprint (which was not certified by peer review) is the author/funder. All rights reserved. No reuse allowed without permission.

Sup. Figure 13

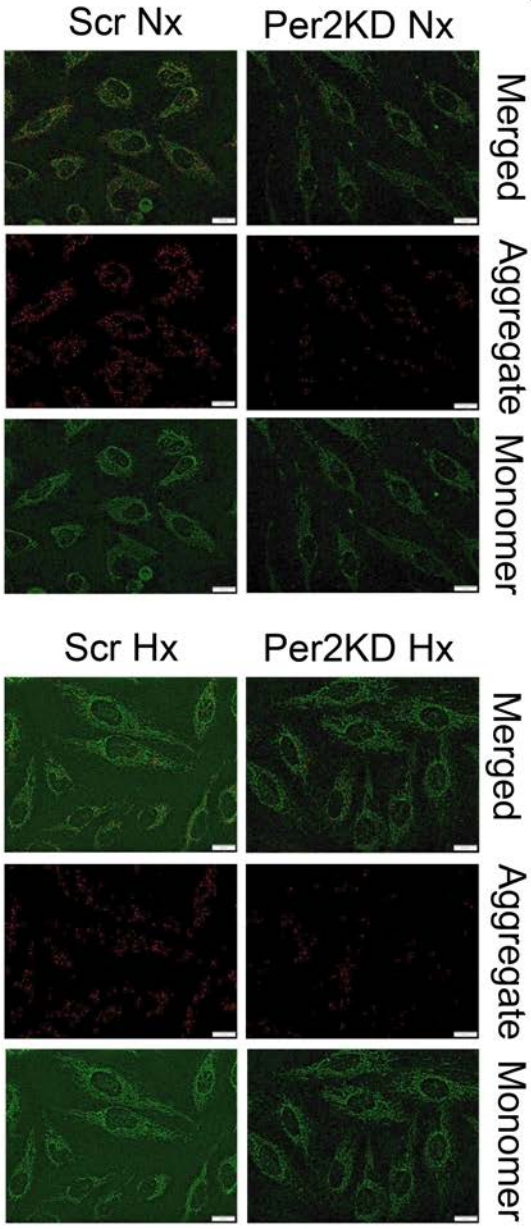

Supplementary Figure 13. JC-1 staining results from PER2 KD or Scr control HMEC-1s in Hx (hypoxia, 1%) or Nx (normoxia). Aggregate represents hyperpolarized cells and monomer represents depolarized cells (mean±SD, n=3).

bioRxiv preprint doi: https://doi.org/10.1101/561340; this version posted May 15, 2019. The copyright holder for this preprint (which was not certified by peer review) is the author/funder. All rights reserved. No reuse allowed without permission.

Sup. Figure 14

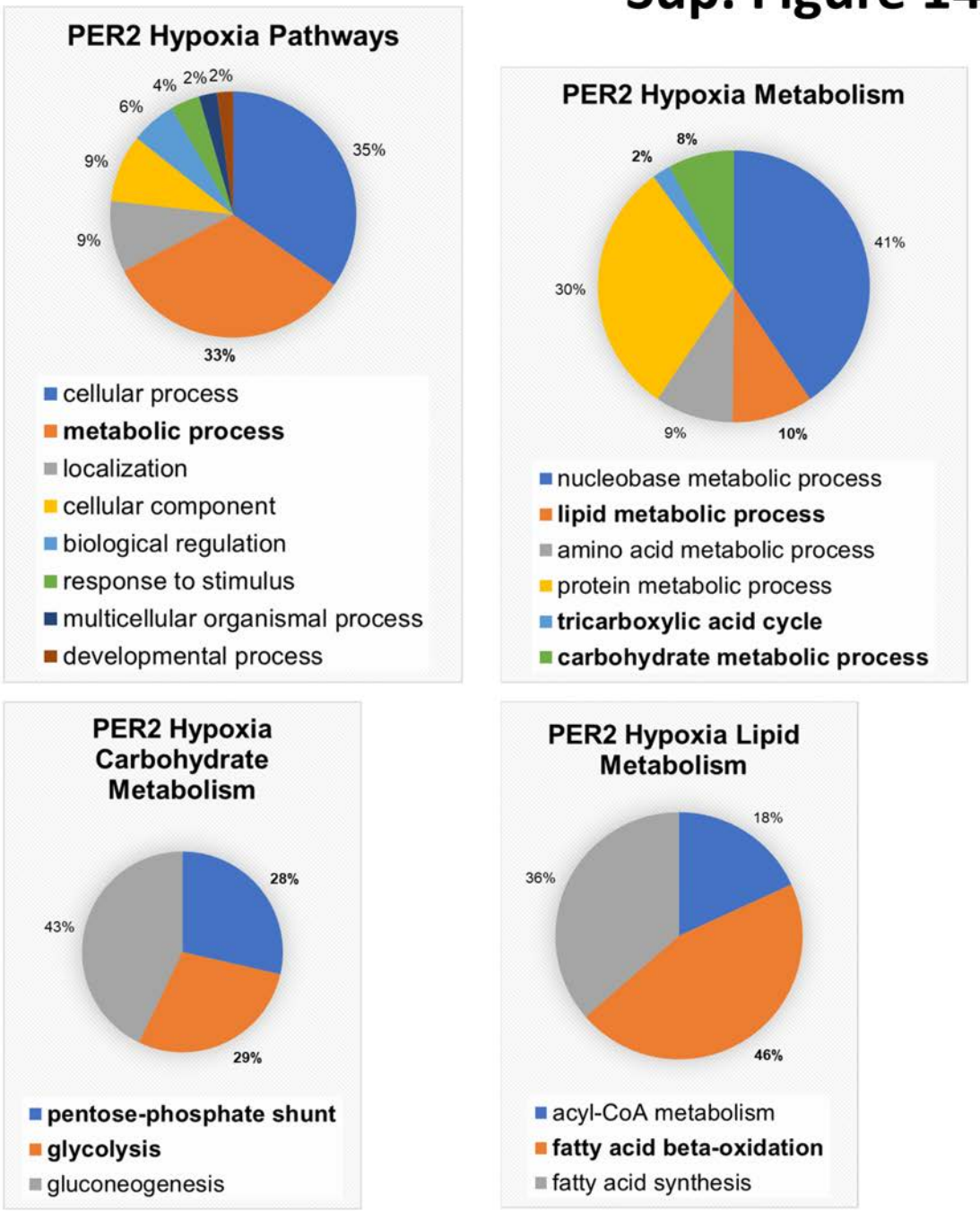

Supplementary Figure 14. PER2-Hypoxia-only-Pathways. PANTHER (Protein ANalysis THrough Evolutionary Relationships) analysis of an affinity purification–mass spectrometry-based proteomics from hypoxic HMEC-1 cells.

bioRxiv preprint doi: https://doi.org/10.1101/561340; this version posted May 15, 2019. The copyright holder for this preprint (which was not certified by peer review) is the author/funder. All rights reserved. No reuse allowed without permission.

Sup. Figure 15

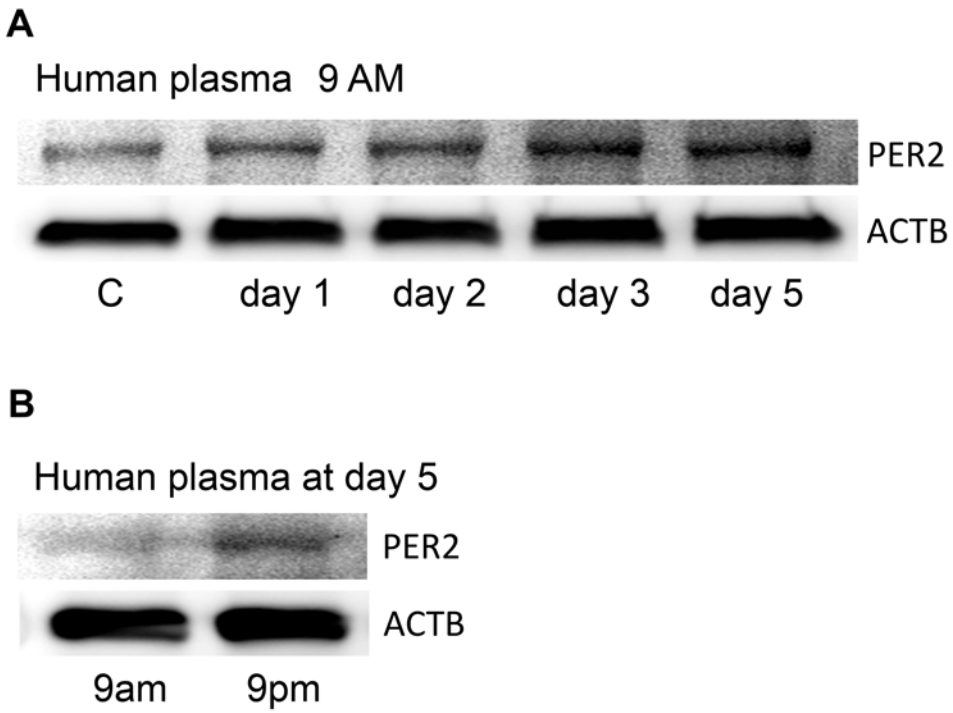

Supplementary Figure 15. (**A, B**) Immunoblots of plasma PER2 at 9AM and 9PM from one healthy human volunteer exposed to 5 days of intense light for 30 min between 8.30 and 9.00 AM.

bioRxiv preprint doi: https://doi.org/10.1101/561340; this version posted May 15, 2019. The copyright holder for this preprint (which was not certified by peer review) is the author/funder. All rights reserved. No reuse allowed without permission.

Sup. Figure 16

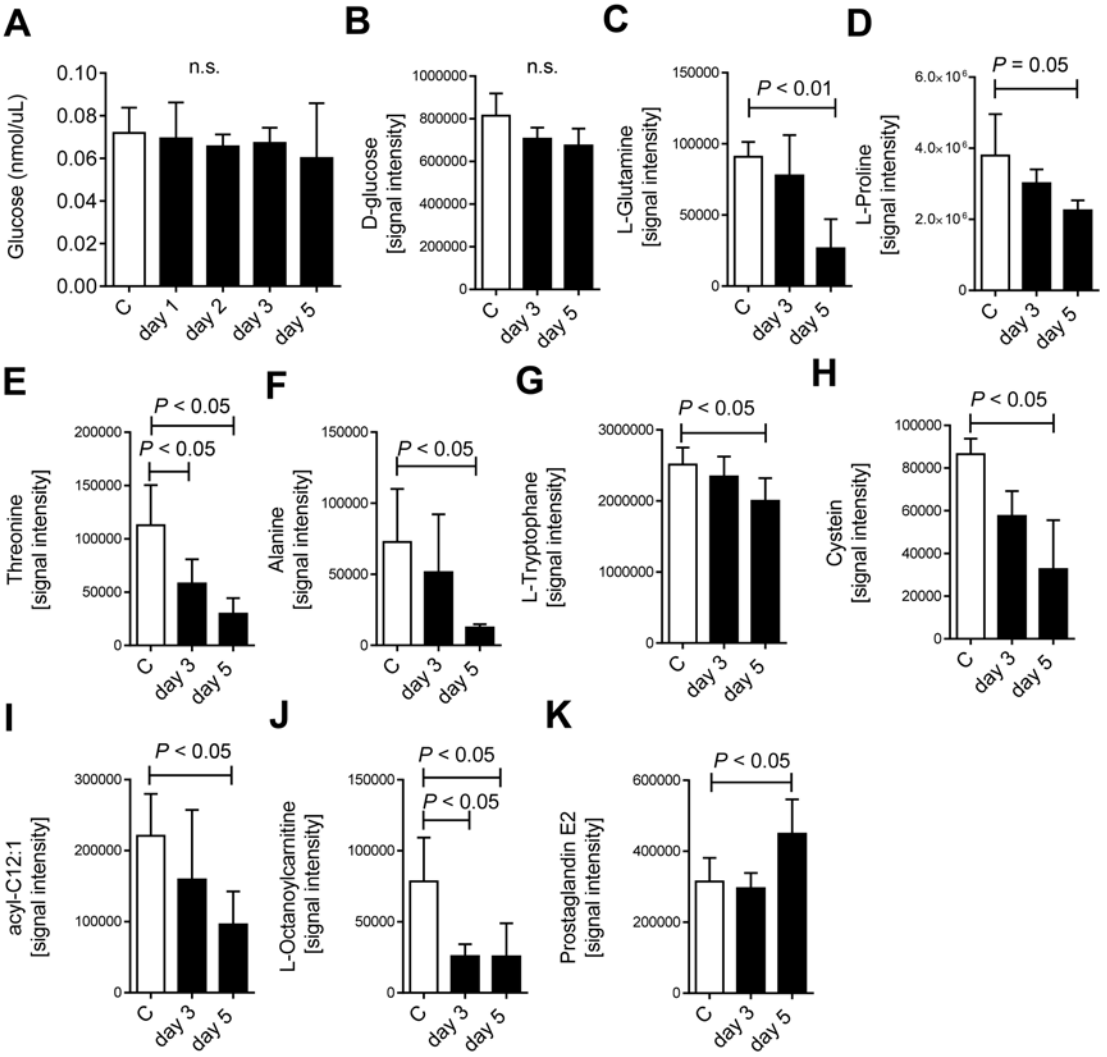

Supplementary Figure 16. (**A**) Plasma glucose levels from human healthy volunteers during 5 days of intense light therapy. (**B-K**)Targeted metabolomics in plasma samples from healthy human volunteers exposed to 5 days of 30 minutes intense light from 8.30 to 9.00 AM each morning.

bioRxiv preprint doi: https://doi.org/10.1101/561340; this version posted May 15, 2019. The copyright holder for this preprint (which was not certified by peer review) is the author/funder. All rights reserved. No reuse allowed without permission.

Sup. Figure 17

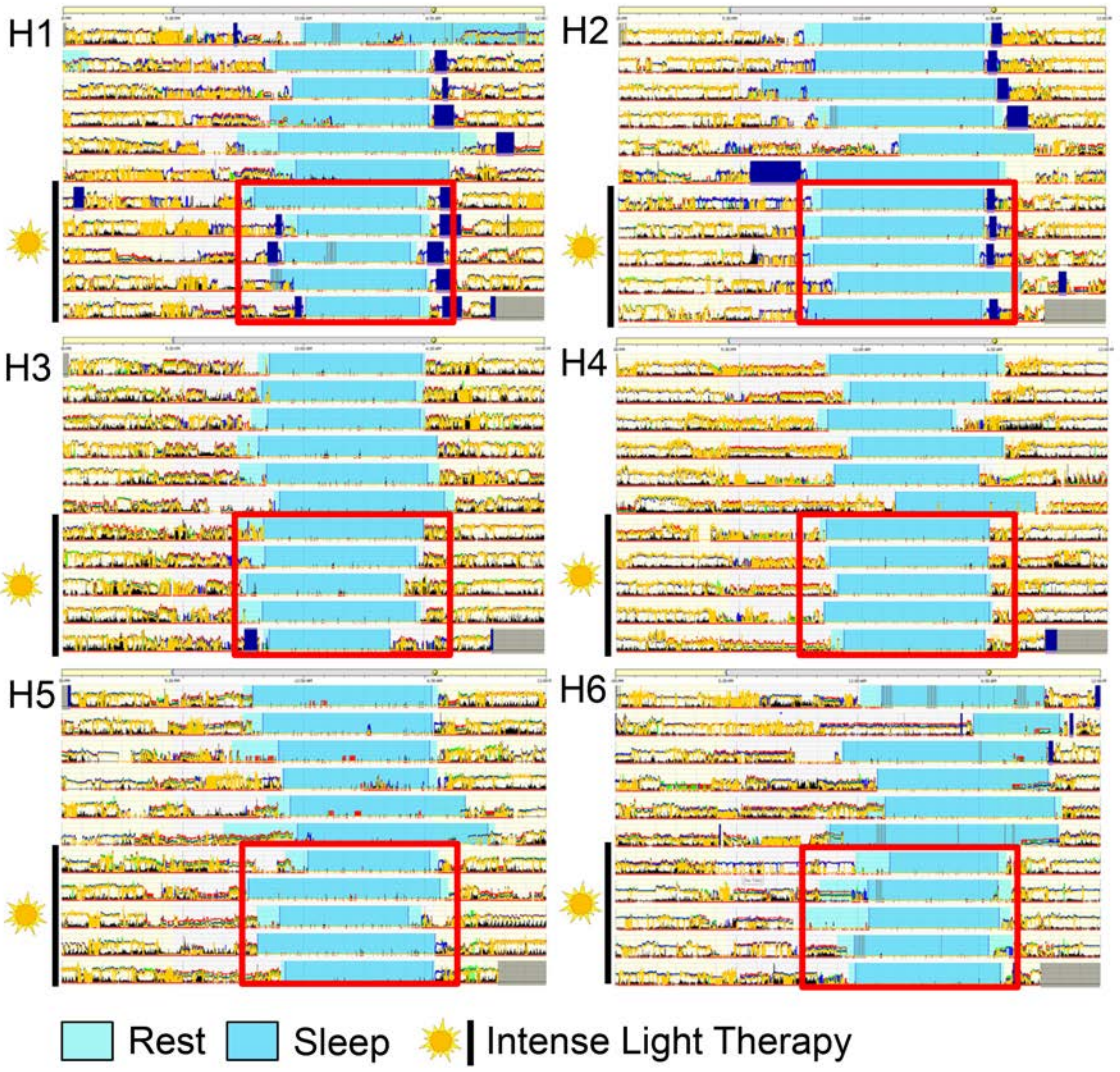

Supplementary Figure 17. Actigraphy data using a validated accelerometer (Actiwatch 2) from human healthy volunteers during 5 days without and 5 days with intense light therapy (30 min intense light from 8.30 – 9.00 AM; n=6, H=healthy volunteer; **Note**: synchronized sleep phases during intense light exposure [red square] vs no intense light therapy.

bioRxiv preprint doi: https://doi.org/10.1101/561340; this version posted May 15, 2019. The copyright holder for this preprint (which was not certified by peer review) is the author/funder. All rights reserved. No reuse allowed without permission.

METHODS

Mouse experiments.

Experimental protocols were approved by the Institutional Review Board (Institutional Animal Care and Use Committee [IACUC]) at the University of Colorado Denver, USA. They were in accordance with the NIH guidelines for the use of live animals. *All mice were housed in a 14 h (hours):10 h L(light):D(dark) cycle and we routinely used 12- to 16-week old male mice.* All mice had a C57BL/6J background. C57BL/6J , *Per2*$^{-/-}$ mice [Per2tm1Brd Tyrc-Brd/J(Zheng et al., 1999)] and PER2 luciferase mice [B6.129S6-*Per2*^{tm1Jt}/J](Yoo et al., 2004) were purchased from Jackson laboratories. *Per2*$^{loxp/loxp}$ and *Adorab2*$^{loxp/loxp}$ (Seo et al., 2015) mice were generated by Ozgene (Perth, Australia). VE-Cadherin-Cre [B6.Cg-Tg(Cdh5-cre)7Mlia/J(Alva et al., 2006)] or Germline Cre [B6.C-Tg(CMV-cre)1Cgn/J] were purchased from Jackson laboratories. To obtain endothelial tissue-specific mice, we crossbred *Per2*$^{loxp/loxp}$ mice with the VE-Cadherin-Cre recombinase mouse. To obtain *Adora2b*$^{-/-}$ mice we crossbred *Adorab2*$^{loxp/loxp}$ with the Germline Cre mouse. Before experiments, mice were housed for at least 4 weeks in a 14/10-h light-dark (lights on 6 AM [ZT0], lights off 8 PM[ZT14]) cycle to synchronize (entrain) the circadian clock of all mice to the ambient light-dark cycle. We conducted all mouse experiments at the same time points (ZT 3, ZT15), unless specified otherwise.

Intense light exposure in mice

Mice were exposed to intense light (10,000 LUX, Lightbox, Uplift Technologies DL930, full spectrum, UV filter) for 3, 5 or 7 days and compared to mice maintained at room light [200 LUX] for 7 days (***Note****: infarct sizes are always the same at ZT 3 (9AM) regardless of the length of being housed under normal housing conditions*) (Bartman et al., 2017). To control for temperature changes, we measured the rectal temperature, using a rectal thermometer probe (RT, Effenberg, Munich, Germany).

bioRxiv preprint doi: https://doi.org/10.1101/561340; this version posted May 15, 2019. The copyright holder for this preprint (which was not certified by peer review) is the author/funder. All rights reserved. No reuse allowed without permission.

Cortisol measurements

To measure plasma cortisol levels in mice after one week of room light or intense light a mouse cortisol ELISA Kit (LifeSpan BioSciences, Inc., Seattle, WA) was used.

Murine model for cardiac MI and heart enzyme measurement

Murine *in situ* myocardial ischemia and reperfusion injury (*60-min ischemia/120 min reperfusion)* and troponin-I (cTnI) measurements were performed as described (Eckle et al., 2006; Eckle et al., 2011; Eckle et al., 2007). Infarct sizes were determined by calculating the percentage of infarcted myocardium to the area at risk (AAR) using a double staining technique with Evan's blue and triphenyltetrazolium chloride. AAR and the infarct size were determined via planimetry using the NIH software Image 1.0 (National Institutes of Health, Bethesda, MA). For troponin I (cTnI) measurements blood was collected by central venous puncture and cTnI was analyzed using a quantitative rapid cTnI assay (Life Diagnostics, Inc., West Chester, PA, USA). ***Note***: *cTnI is highly specific for myocardial ischemia and has a well-documented correlation with the infarct size in mice* (Eckle et al., 2006; Eckle et al., 2008; Eckle et al., 2007; Kohler et al., 2007) *and humans* (Vasile et al., 2008).

Wheel running

Mice were maintained individually in running-wheel cages (Starr Life Sciences, wheel diameter: 11.5 cm). Running-wheel activity was recorded every 5 minutes using the Vital View Data Acquisition System (Starr Life Sciences, Oakmont, PA). Data were analyzed using BioDare (Biological Data Repository) (Moore et al., 2014). Amplitude of wheel running activity were calculated using the fast fourier transform non-linear least squares (FFT-NLLS) method. The distance walked was calculated as the sum of a 7 day-recording.

Luciferase Assay

Expression of the PER2 protein using luciferase reporter mice was assayed as described (Eckle et al., 2012). Expression of the PER2 protein using luciferase reporter mice was determined using the tissue homogenates in T-per Tissue Protein Extraction Reagent (Pierce, Thermo

bioRxiv preprint doi: https://doi.org/10.1101/561340; this version posted May 15, 2019. The copyright holder for this preprint (which was not certified by peer review) is the author/funder. All rights reserved. No reuse allowed without permission.

Fisher Scientific, Waltham, MA). The homogenates were centrifuged for 30mins at 4900 x g at 4oC. The luciferase protein activity was measured by using the Dual-Luciferase Reporter Assay System from Promega according to the manufacturer's instructions using a Biotek Synergy 2 Multimode Microplate Reader (Winooski, VT).

Enucleation procedure in mice

Mice were pre-anesthetized with subcutaneous carprofen and buprenorphine injections and anesthetized with a ketamine/xylazine/ace cocktail. The periocular region was then clipped to remove surrounding hair. After a surgical scrub with betadine, the optic nerve and associated blood vessels were clamped with hemostats. After 2 minutes the entire globe of eye and the optic nerve were removed. For additional analgesia bupivacaine was dripped into the socket. Next, the complete upper and lower eyelid margin were removed with fine tip scissors and the eyelids were closed with 3-4 interrupted sutures. Mice were recovering in cages on warm water circulating blankets. Carprofen injections were repeated every 24 hours for 2 days post operatively. After a 2-week recovery period under standard housing conditions, mice underwent intense light housing or myocardial ischemia studies.

^{13}C-tracers in vivo. C57BL/6 wildtype mice were housed under daylight (10,000 LUX, L:D 14:10 h) or standard room light (200 LUX, L:D 14:10 h) for 7 days followed by infusion of 10 mg/kg/min U-^{13}C-glucose (Cambridge Isotope Laboratories, Tewksbury, MA) via an intra-arterial catheter over 90 minutes. Left ventricles of the hearts were flushed with ice cold KCl and the left ventricle was shock frozen and analyzed by liquid chromatography–tandem mass spectrometry. Isotope-resolved metabolite analyses were performed by LC-MS on a Waters Acquity ultrahigh-performance liquid chromatography (UPLC) system coupled to a Waters Synapt HDMS quadrupole time-of-flight mass spectrometer equipped with an atmospheric pressure electrospray ionization (ESI) source. LC-MS was performed with full-mass detection within m/z 100-1000 in the positive-ion or negative-ion mode as described below. The typical MS operation parameters included ESI spray voltage 2.8 kV, sampling cone voltage 4 V, drying

bioRxiv preprint doi: https://doi.org/10.1101/561340; this version posted May 15, 2019. The copyright holder for this preprint (which was not certified by peer review) is the author/funder. All rights reserved. No reuse allowed without permission.

gas flow 50 L/min / temperature 120 °C, and nebulizing nitrogen gas flow 700 L/h / temperature 350 °C. The authentic compound sodium D-fructose-6-sphosphate was obtained from Sigma-Aldrich and were used as the standard substances for location and identification of the targeted metabolites. UPLC conditions were optimized to ensure appropriate separation of each metabolite from its structural isomers and the interfering components detected in the samples. For sample preparation, frozen specimens were individually ground to fine powder in liquid nitrogen and were weighed to 5-mL borosilicate glass test tubes. Ice-cold methanol-water (50:50, v/v), equivalent to 1 mL per 100 mg tissue, was added to each tube. The samples were lysed on ice with 15 s x 2 sonications using a Fisher Scientific Model 100 cell dismembrator. After vortex-mixing and 5-min sonication in an ice-water bath, ice-cold methanol, equivalent to 1 mL per 100 mg tissue, was added. The sample tubes were capped, violently vortex-mixed for 2 min, sonicated in the same ice-water bath for 5 min and then placed at – 20 °C for 2 h. before the tubes were centrifuged at 4,000 rpm and 4 °C for 15 min in a Beckman Coulter Allegra X-22R centrifuge. The clear supernatant of each sample was collected and transferred to a 3-mL borosilicate glass test tube for the following LC-MS analyses. Fructose-6-phosphate was measured by ion-pairing LC-MS using tributylamine (TBA) as the paired counter ion reagent.(Luo et al., 2007) The chromatographic separation was conducted on a YMC-Triart C18 UPLC column (2.1 x 150 mm, 1.9 µm) using binary-solvent gradient elution with 2 mM TBA in water (pH adjusted to 6 with acetic acid) as mobile phase A and methanol as mobile phase B. The elution gradient was 0-9 min, 2% to 55 % B; 9-9.5 min, 55% to 100 % B; 9.5– 11 min, 100 % B. The column was equilibrated with 2% B for 5 min between injections. The column flow rate was 0.25 mL/min and the column temperature were 50 °C. A 100-µL aliquot of each supernatant from individual mouse heart specimens was dried under a nitrogen flow in a fume hood and the residue was reconstituted in 200 µL of mobile phase A. 5 µL was injected for LC-MS with negative-ion detection. The organic acids were analyzed by chemical derivatization LC-MS with 3-nitrophenyl hydrazine (3NPH) as the pre-analytical derivatizing

bioRxiv preprint doi: https://doi.org/10.1101/561340; this version posted May 15, 2019. The copyright holder for this preprint (which was not certified by peer review) is the author/funder. All rights reserved. No reuse allowed without permission.

reagent.(Han et al., 2013a) In brief, 100 µL of the supernatant was mixed 50 µL of 200 mM 3NPH.HCl in 75% methanol and 50 µL of 150 mM 1-ethyl-3-(3-dimethylaminopropyl)carbodiimide-HCl. The mixture could react at 30 ºC for 30 min and was then mixed with 400 µL of water. 10-µL aliquots were injected onto a C8 UPLC column (2.1 x 50 mm, 1.7 µm) for LC-MS runs with negative-ion detection and using the LC procedure as described.(Han et al., 2013a) For all the above LC-MS analyses, the monoisotopic ion chromatograms of individual metabolites, together with their isotopomeric counterparts resulting from the U-^{13}C glucose tracer, were extracted based on their calculated m/z values, within a mass window of 60 ppm (+/- 30 ppm), and their peak areas were integrated. The peak areas of any observed isotopomeric forms derived from the U-^{13}C glucose tracer for each metabolite was corrected by subtracting the abundance contributions from the natural and any other U-^{13}C glucose tracer-derived isotopic forms (Eckle et al., 2013; Eckle et al., 2012; Han et al., 2013a; Han et al., 2013b).

PFK and cAMP-activity mouse tissue

To measure Phosphofructokinase activity from myocardium or plasma, C57BL/6J or *Per2*$^{-/-}$ mice were euthanized following light exposure. Blood was removed to obtain plasma further analysis, and the tissue was immediately flash frozen at -80°C. Enzyme activity from homogenized tissue or plasma was determined using a PFK Assay Kit from Biovison. To determine cAMP in cardiac tissue, a cyclic AMP Enzyme Immunoassay Kit (Mouse/Rat cAMP Parameter Assay Kit, R&D, Minneapolis, MN) was used according to the manufacturer's protocol.

Adenosine measurements. Whole murine hearts were collected in 1 mL of 80% MeOH and flash-frozen under liquid nitrogen and stored at -80°C. Adenosine was extracted and quantified in the tissue as described (Lee et al., 2018). Analyses were performed on an Agilent Technologies 1260 Infinity HPLC using a phenomenex Luna C18(2) column (100 Å, 150 X 4.6 mm) (mobile phase A: 50 mM KH2PO4, 5 mM tetrabutylammonium bisulfate, pH 6.25;

bioRxiv preprint doi: https://doi.org/10.1101/561340; this version posted May 15, 2019. The copyright holder for this preprint (which was not certified by peer review) is the author/funder. All rights reserved. No reuse allowed without permission.

mobile phase B: acetonitrile; column temperature: 30°C; flow rate: 1 mL/min; 75 µL injection). Samples were filtered through VIVASPIN 500 membranes (Sartorius Stedim Biotech, 5,000 MWCO, PES) prior to HPLC analysis. Chromatographic separation of the metabolites was performed using a combination of isocratic and gradient methods including column washing and equilibration periods at the end (0 min: 100% A; 7 min: 100% A; 10 min: 97% A; 18 min: 97% A; 45 min: 86% A; 60 min: 50% A; 80 min: 50% A; 90 min: 100% A; 135 min: 100% A). Adenosine was detected by absorption at 254 nm, and the absorbance spectra and retention time verified by co-injection with an authentic standard.

HIF1A-HRE binding assay

Nuclear protein fractions were isolated from heart tissue using NE-PER kit following the manufacturer's instructions (Thermo Fisher Scientific, Waltham, MA). Protein was quantified using the BCA Protein Assay Kit (Thermo Fisher Scientific, Waltham, MA). HIF1A transcription factor from 20 µg of nuclear protein were measured using a HIF1A Transcription Factor Assay kit (Abcam, ab133104, Cambridge, MA).

Microarray analysis

Total RNA was isolated from heart tissue from intense light or room light 'pretreated' C57BL/6J or *Per2*$^{-/-}$ mice with the RNeasy micro kit (Qiagen, Valencia, CA) using Qiagen on-column DNase treatment to remove any contaminating genomic DNA. The integrity of RNA was assessed using a Tapestation 2200 (Agilent Technologies) and RNA concentration was determined using a NanoDrop ND-1000 spectrophotometer (NanoDrop, Rockland, DE). Hybridization cocktail was prepared starting with 100ng Total RNA using the GeneChip WT PLUS Reagent Kit. Samples were hybridized to the Arrays (Mouse Clariom D arrays) for 16 hours at 45 degrees C in a GeneChip Hybridization Oven 645. Arrays were then washed and stained in a GeneChip Fluidics Station 450 and scanned in a GeneChip Scanner 3000. Each array was subjected to visual inspection for gross abnormalities. Several other QC metrics were used to monitor hybridization efficiency and RNA integrity over the entire processing

bioRxiv preprint doi: https://doi.org/10.1101/561340; this version posted May 15, 2019. The copyright holder for this preprint (which was not certified by peer review) is the author/funder. All rights reserved. No reuse allowed without permission.

procedure. Raw image files were processed using Affymetrix GCOS 1.3 software to calculate individual probe cell intensity data and generate CEL data files. Using GCOS and the MAS 5.0 algorithm, intensity data was normalized per chip to a target intensity TGT value of 500 and expression data and present/absent calls for individual probe sets calculated. Gene symbols and names for data analyzed with the MAS 5.0 algorithm were from the Affymetrix NetAffx Mouse 430_2 annotations file. Quality control was performed by examining raw DAT image files for anomalies, confirming each GeneChip array had a background value less than 100, monitoring that the percentage present calls was appropriate for the cell type, and inspecting the poly (A) spike in controls, housekeeping genes, and hybridization controls to confirm labeling and hybridization consistency. According to our experimental setup the arrays were normalized, grouped and analyzed for differentially expressed transcripts based on different statistical tests. Different clustering algorithms allowed us to identify transcripts that show similar expression profiles. Using the TAC (Transcriptome Analysis Console, Affymetrix) software we were able to identify biological mechanisms, pathways and functions most relevant to our experimental dataset. Array data have been deposited in the Array Express database at EMBL-EBI (www.ebi.ac.uk/arrayexpress) under accession number E-MTAB-7196 (http://www.ebi.ac.uk/arrayexpress/experiments/E-MTAB-7196). *Username: Reviewer_E-MTAB-7196; Password: WWyjkjym.*

Modified Miles Assay.

Mice were injected with Evans blue dye (80mg/kg) via a carotid catheter at the beginning of reperfusion after 60 minutes of ischemia. After 2 hours of reperfusion, mice were euthanized and perfused with citrate buffer, pH4. The hearts were then excised, cut into 1mm thick slices and photographed. Heart slices were then incubated in 1ml of formamide overnight at 70 °C. After centrifugation, absorbance at 620 nm was measured by using a spectrophotometer Biotek [Synergy 2 Multimode Microplate Reader (Winooski, VT)]. Extravasated Evans blue (ng) was

bioRxiv preprint doi: https://doi.org/10.1101/561340; this version posted May 15, 2019. The copyright holder for this preprint (which was not certified by peer review) is the author/funder. All rights reserved. No reuse allowed without permission.

determined from a standard curve and normalized to tissue weight (g). Evans blue dye content was determined from standard curve and normalized to heart tissue weight (Galaup et al., 2012).

Chromatin immunoprecipitation (ChIP) assay from mouse heart tissue.

ChIP assays for heart tissue were performed using the SimpleChIP® Plus Enzymatic Chromatin IP Kit (Cell signaling). Briefly, freshly whole hearts were placed into PBS containing 1.5% formaldehyde and homogenized using a probe tissue homogenizer. Crosslinking was stopped after 15 min by adding glycine for 5min. The samples were centrifuged to collect the pellet. Pellets were disaggregated with a dounce homogenizer and chromatin was enzymatically digested to yield 200- to 1,500-bp DNA fragments. The chromatin was incubated at 4°C overnight with a HIF1A antibody (NB100-134, Novus, Littleton CO) or rabbit IgG control (Cell Signaling, Danvers, MA). After reverse cross-linking by heating the samples at 65°C overnight and treating with Proteinase K, DNA was purified using DNA purification kit (Cell Signaling, Danvers, MA). Quantitative analyses of DNA products obtained from ChIP assay were performed by real-time RT-PCR with primers specific for the mouse ANGPTL4 promoter. The ChIP data were normalized against IgG to account for non-specific immunoprecipitation (fold enrichment relative to the negative (IgG) sample). Primers used were: Primer 1: sense CCC CAC TTG CCA TCT GAA CT, antisense GAT GCC TTC TTG ACT GAC CCC, Primer 2: sense GGG AAT TTC CGG CCT TAG GAT, antisense GTT CTT GGG GAT GGC TGC TTC, Primer 3: sense CCT GGG ACG AGA TGA ACT TGC, antisense ATC TTT TCC CTT GGG CCC CT for the mouse ANGPTL4 promoter (see also **Supplementary Figure 5**).

Cell culture

Human microvascular endothelial cells (HMEC-1) were cultured as described previously (Eltzschig et al., 2005; Eltzschig et al., 2003). PER2 KD and control cell lines (scrambled [Scr]) were selected using 2.5 μg/mL puromycin. HIF1A KD and control cell lines were selected using 350 μg/mL geneticin (G418). All experiments were conducted after 12h of serum starvation to reset circadian rhythmicity (Eckle et al., 2012).

bioRxiv preprint doi: https://doi.org/10.1101/561340; this version posted May 15, 2019. The copyright holder for this preprint (which was not certified by peer review) is the author/funder. All rights reserved. No reuse allowed without permission.

Hypoxia exposure. For hypoxia experiments cells were placed in a hypoxia chamber (Coy Laboratory Products Inc., Grass Lake, MI) in preequilibrated hypoxic medium at 1% O_2 for 24 hours.

Lentiviral-mediated generation of cells with knockdown of PER2 or HIF1A

Stable cell cultures with decreased PER2 and HIF1A expression were generated by lentiviral-mediated shRNA expression. pLKO.1 lentiviral vector targeting PER2 had shRNA sequence of CCG GGA CAC ACA CAA AGA ACT GAT ACT CGA GTA TCA GTT CTT TGT GTG TGT CTT TTT (TRCN0000018542) and HIF1A had shRNA sequence of CCG GCC AGT TAT GAT TGT GAA GTT ACT CGA GTA ACT TCA CAA TCA TAA CTG GTT TTT (TRCN 0000003809). For controls, nontargeting control shRNA (SHC002; Sigma) was used. HMEC-1 were co-transfected with pLK0.1 vectors and packaging plasmids to produce lentivirus. Filtered supernatants were used for infection of HMEC-1 and cells were selected with puromycin or geneticin until a knockdown was confirmed (Eckle et al., 2013).

Transcriptional Analysis

Total RNA was isolated using Trizol Reagent (Invitrogen, Carlsbad, CA), phenol-chloroform extraction, and ethanol precipitation followed by purification in a modified protocol from RNeasy Mini Kit (Qiagen, Germantown, MD). RNA was quantified using either a Qubit 3.0 RNA BR Assay Kit (Thermo Fisher Scientific, Waltham, MA) or Nanodrop 2000. Quantification of transcript levels was determined by real-time RT-PCR (iCycler; Bio-Rad Laboratories, Inc, Hercules, CA). qPCR reactions contained 1x final primer concentration (Qiagen primers, Germantown, MD) or 1 µM sense and 1 µM antisense oligonucleotides (Invitrogen custom DNA oligos, Carlsbad, CA) with SYBR Green (Bio-Rad, Hercules, CA). Primer sets used (Qiagen QuantiTect) were Hs_PER2_1_SG (QT0011207), Hs_PKM_1_SG (QT00028875), Hs_LDHA_1_SG (QT00001687), Hs_SIRT3_1_SG (QT00091490), Hs_ACTB_2_SG (QT01680476), and Hs_COX4|2_1_SG (QT00044933), Mm_Per2_1_SG (QT00198366), Mm_Angptl4_1_SG (QT00139748), Mm_Actb_2_SG (QT01136772).

bioRxiv preprint doi: https://doi.org/10.1101/561340; this version posted May 15, 2019. The copyright holder for this preprint (which was not certified by peer review) is the author/funder. All rights reserved. No reuse allowed without permission.

Primers for human OPN4 (Invitrogen, Carlsbad, CA, sense 5'-AGT CGC CCC TAC CCC AGC TA-3' and antisense 5'- CAC AGC TGC TGC CTC CAT GT-3') were custom designed. Each target sequence was amplified using the following protocol: 95°C for 3 min, 40 cycles of 95°C for 15 sec, 55°C for 0.5 min, 72°C for 10 sec, 72°C for 1 min and a melt curve protocol.

Immunoblotting experiments

Protein was isolated from HMEC-1 using M-Per following manufacturer's instructions (Thermo Fisher Scientific, Waltham, MA) and including a protease and phosphatase inhibitor cocktail (Thermo Fisher Scientific, Waltham, MA). Protein was quantified using a Qubit Fluorometer 3.0 and Qubit Protein Assay Kit (Thermo Fisher Scientific, Waltham, MA). 5 – 25 μg of protein was denatured at 95°C in Laemmli sample buffer for 5 min. Samples were resolved on a 4 – 10% polyacrylamide gel and transferred to nitrocellulose membranes, which were blocked for 1h at room temperature in either 5% BSA / TBST or 5% milk / TBST. The membranes were incubated in primary antibody at a concentration of 1:1000 overnight at 4°C. The primary antibodies used were rabbit polyclonal PER2 (Novus Biologicals, NB100-125, Littleton CO, or Abcam, ab64460, Cambridge, MA), rabbit polyclonal IDH2 (Novus Biologicals, NBP2-22166, Littleton CO), rabbit polyclonal SUCLG1 (Novus Biologicals, NBP1089489, Littleton CO), rabbit polyclonal ACO2 (Novus Biologicals, H00000050-D01P, Littleton CO), rabbit polyclonal SIRT3 (Abcam, ab86671, Cambridge, MA), anti-alpha Tubulin antibody (Abcam, ab7291, Cambridge, MA), Anti-VDAC1 / Porin antibody (Abcam, ab15895, Cambridge, MA), Anti-TATA binding protein (TBP) antibody (Abcam, ab51841, Cambridge, MA), mouse monoclonal β-ACTIN (Cell Signaling Technologies, 8H10D10, Danvers, MA), and mouse monoclonal anti-DDK (FLAG) (OriGene Technologies, TA50011-100, Rockville, MD). The next day, blots were washed 3 – 4x with TBST and incubated with secondary antibody at a concentration of 1:5000 in the respective blocking buffer, washed an additional 3 times, and visualized using SuperSignal West Femto Maximum Sensitivity Substrate (Thermo Fisher Scientific, Waltham, MA). The secondary antibodies used were goat polyclonal IgG

bioRxiv preprint doi: https://doi.org/10.1101/561340; this version posted May 15, 2019. The copyright holder for this preprint (which was not certified by peer review) is the author/funder. All rights reserved. No reuse allowed without permission.

(Novus Biologicals, NB7487), goat anti-mouse IgM (Calbiochem, San Diego, CA), and goat anti-rabbit IgG (Thermo Fisher Scientific, Waltham, MA).

Lactate measurements

Lactate measurements were done using the L-Lactate Colorimetric Assay Kit following the manufacturer's protocol (Abcam, Cambridge, MA).

Cytotoxicity

Cytotoxicity was determined using the LDH-Cytotoxicity Assay Kit per manufacturer's protocol (Abcam, Cambridge, MA).

Seahorse stress tests

Glycolytic stress tests. The XF24 Seahorse Bioanalyzer was used in conjunction with glycolytic stress tests following manufacturer's specifications (Agilent, Santa Clara, CA). Cells were plated in the morning at a density of $1.2x10^5$ cells / well and serum starved in the evening one day prior to assaying. One hour prior to the stress test cells were incubated in XF Assay Medium (Agilent, Santa Clara, CA) at a pH of 7.4. Final concentration of glucose was 10 mM / well, oligomycin 1.0 μM / well, and 2-deoxyglucose 50 mM / well. *Mitochondrial stress tests.* The XF24 Seahorse Bioanalyzer was used for mitochondrial stress tests (Agilent, Santa Clara, CA). For all assays, pH and oxygen consumption rate (OCR) were measured. For TCA cycle readouts, an additional measurement of carbon dioxide evolution rate (CDER) was measured. Final concentrations were 1.0 μM oligomycin, 3.6 μM FCCP, and 1.125 μM Rotenone / Antimycin A. For fatty acid mitochondrial stress tests, cells were supplemented with palmitate:BSA (Agilent, 102720-100) prior to the run and half the plate received 800 μM etomoxir as a control. *Cell energy phenotype assays.* Following manufacturer's instructions (Agilent, Santa Clara, CA), the Seahorse Bioanalyzer was used to assess cell energy phenotype at baseline.

Chromatin immunoprecipitation (ChIP) assay- cell culture

bioRxiv preprint doi: https://doi.org/10.1101/561340; this version posted May 15, 2019. The copyright holder for this preprint (which was not certified by peer review) is the author/funder. All rights reserved. No reuse allowed without permission.

ChIP assays were performed using the ChIP-IT™ Express Enzymatic Kit from Active Motif (Carlsbad, CA, USA). Briefly, Scr and PER2KD HMECs were grown to 90% confluence in phenol red-free Dulbecco's modified Eagle medium (DMEM) supplemented with 10% charcoal DEXTRAN-stripped FBS for at least 3 days. After hypoxia exposure at 1% O_2 for 24h, ChIP assays were performed according to manufacturer's protocol. Briefly, chromatin was cross-linked in 1% formaldehyde in minimal cell culture medium (Invitrogen, Carlsbad, CA), and nuclei were extracted. Chromatin was enzymatically digested for 11mins to yield 200- to 1,500-bp DNA fragments and the supernatant containing precleared chromatin was then incubated at 4°C overnight with mouse monoclonal HIF1A antibody (H1alpha67, ChIP Grade, Abcam, Cambridge, MA) or rabbit IgG control (Cell Signaling, Danvers, MA). After reverse cross-linking by heating the samples at 65°C overnight and treating with Proteinase K, DNA was purified using phenol-chloroform extraction. Quantitative analyses of DNA products obtained from ChIP assay were performed by RT-PCR with primers specific for the human LDHA promoter. RT-PCRs conducted on DNA derived from input chromatin templates served as positive controls whereas reactions conducted on IgG-precipitated templates served as negative controls. The RT-PCR signal was barely detectable for these controls. The signal for these samples and IgG-precipitated templates was negligible on gels. Primers used were: sense ATT ACG TGC CAG AAG CTG TT and antisense TTT CCT CAT CCA TGA AAC CT for the human LDHa promoter. Conventional PCR signals were stained with ethidium bromide in 1% agarose gels.

Affinity purification-mass spectrometry-based proteomics

HMEC-1 were placed in a hypoxia chamber (Coy Laboratory Products Inc., Grass Lake, MI) in preequilibrated hypoxic medium at 1% O_2. Following 24 h of hypoxia, the samples were isolated for cytoplasmic and nuclear protein fractions according to the NE-PER kit specifications (Thermo Fisher Scientific, Waltham, MA). To identify interacting proteins with PER2, co-immunoprecipitation (Co-IP) for PER2 was performed using the Pierce Co-IP Kit

bioRxiv preprint doi: https://doi.org/10.1101/561340; this version posted May 15, 2019. The copyright holder for this preprint (which was not certified by peer review) is the author/funder. All rights reserved. No reuse allowed without permission.

(Thermo Fisher Scientific, Waltham, MA). Specifically, 10 μg of rabbit anti-PER2 antibody (Novus, NB100-125) was immobilized to the amine-reactive resin. 100 μg of sample was incubated overnight at 4 ^{o}C with the anti-PER2 coupled resin. Samples were washed and then eluted. Samples were then loaded onto a 1.5 mm thick NuPAGE Bis-Tris 4-12% gradient gel (Invitrogen, Carlsbad, CA). The BenchMark™ Protein Ladder (Invitrogen, Carlsbad, CA) was used as a protein molecular mass marker. The electrophoretic run was performing by using MES SDS running buffer, in an X-Cell II mini gel system (Invitrogen) at 200 V, 120 mA, 25 W per gel for 30 minutes. The gel was stained using SimplyBlue™ SafeStain (Invitrogen, Carlsbad, CA) stain and de-stained with water according to the manufacturer's protocol. Each lane of the gel was divided into 9 equal-sized bands, and proteins in the gel were digested as follows. Gel pieces were destained in 200 μL of 25 mM ammonium bicarbonate in 50 % v/v acetonitrile for 15 min and washed with 200 μL of 50% (v/v) acetonitrile. Disulfide bonds in proteins were reduced by incubation in 10 mM dithiothreitol (DTT) at 60 °C for 30 min and cysteine residues were alkylated with 20 mM iodoacetamide (IAA) in the dark at room temperature for 45 min. Gel pieces were subsequently washed with 100 μL of distilled water followed by addition of 100 mL of acetonitrile and dried on SpeedVac (Savant, Thermo Fisher Scientific, Waltham, MA). Then 100 ng of trypsin was added to each sample and allowed to rehydrate the gel plugs at 4 °C for 45 min and then incubated at 37 °C overnight. The tryptic mixtures were acidified with formic acid up to a final concentration of 1%. Peptides were extracted two times from the gel plugs using 1% formic acid in 50% acetonitrile. The collected extractions were pooled with the initial digestion supernatant and dried on SpeedVac (Savant, Thermo Fisher Scientific, Waltham, MA). Samples were desalted on Thermo Scientific Pierce C18 Tip. For mass spectrometry, samples were analyzed on an LTQ Orbitrap Velos Pro mass spectrometer (Thermo Fisher Scientific, Waltham, MA) coupled to an Eksigent nanoLC-2D system through a nanoelectrospray LC − MS interface. A volume of 8 μL of sample was injected into a 10 μL loop using the autosampler. To desalt the sample, material was flushed

bioRxiv preprint doi: https://doi.org/10.1101/561340; this version posted May 15, 2019. The copyright holder for this preprint (which was not certified by peer review) is the author/funder. All rights reserved. No reuse allowed without permission.

out of the loop and loaded onto a trapping column (ZORBAX 300SB-C18, dimensions 5x0.3 mm 5 μm) and washed with 0.1% FA at a flow rate of 5 μL/min for 5 min. The analytical column was then switched on-line at 600 nl/min over an in house-made 100 μm i.d. × 150 mm fused silica capillary packed with 4 μm 80 Å Synergi Hydro C18 resin (Phenomex; Torrance, CA). After 10 min of sample loading, the flow rate was adjusted to 350 nL/min, and each sample was run on a 90-min linear gradient of 2–40% ACN with 0.1% formic acid to separate the peptides. LC mobile phase solvents and sample dilutions used 0.1% formic acid in water (Buffer A) and 0.1% formic acid in acetonitrile (Buffer B) (Optima™ LC/MS, Fisher Scientific, Pittsburgh, PA). Data acquisition was performed using the instrument supplied Xcalibur™ (version 2.1) software. The mass spectrometer was operated in the positive ion mode. Data acquisition was performed using the instrument supplied Xcalibur™ (version 2.1) software. The mass spectrometer was operated in the positive ion mode. Full MS scans were acquired in the Orbitrap mass analyzer over the *m/z* 350–1800 range with resolution 60,000 (*m/z* 400). The target value was 5.00E+05. The twenty most intense were selected for sequencing and fragmented in the ion trap with normalized collision energy of 35%, activation q = 0.25, activation time of 20 ms, and one microscan. The target value was 1.00E+04. The maximum allowed ion accumulation times were 500 ms for full scans and 150 ms for CID. For database searching and protein identification, MS/MS spectra were extracted from raw data files and converted into mgf files using MassMatrix (Cleveland, OH). These mgf files were then independently searched against mouse SwissProt database using an in-house Mascot™ server (Version 2.2, Matrix Science). Mass tolerances were +/- 15 ppm for MS peaks, and +/- 0.6 Da for MS/MS fragment ions. Trypsin specificity was used allowing for 1 missed cleavage. Met oxidation, protein N-terminal acetylation, peptide N-terminal pyroglutamic acid formation were allowed for variable modifications while carbamidomethyl of Cys was set as a fixed modification. Scaffold (version 4.4.6, Proteome Software, Portland, OR, USA) was used to validate MS/MS based peptide and protein identifications. Peptide identifications were

bioRxiv preprint doi: https://doi.org/10.1101/561340; this version posted May 15, 2019. The copyright holder for this preprint (which was not certified by peer review) is the author/funder. All rights reserved. No reuse allowed without permission.

accepted if they could be established at greater than 95.0% probability as specified by the Peptide Prophet algorithm. Protein identifications were accepted if they could be established at greater than 99.0% probability and contained at least two identified unique peptides. Following identification of potential PER2 interacting proteins in normoxia, hypoxia, and normoxia vs. hypoxia, lists obtained from Scaffold were analyzed by Ingenuity Pathway Analysis (Qiagen), Panther Classification System, and Reactome Analysis to detect pathways PER2 regulates in normoxia and hypoxia.

Co-immunoprecipitations (Co-IPs)

Co-IPs were done using the Pierce Co-Immunoprecipitation (Co-IP) Kit (Thermo Fisher Scientific, Waltham, MA). 10 μg of antibody was immobilized to columns. Pulled-down protein was quantified using a Qubit Fluorometer 3.0 and resolved by immunoblotting as described.

Subcellular compartment analysis

HMEC-1 were placed in hypoxia (1% O_2) or normoxia for 24 h. After normoxia or hypoxia exposure, samples were isolated for cytoplasmic and nuclear protein fractions according to the NE-PER kit specifications (Thermo Fisher Scientific, Waltham, MA). Mitochondria protein fraction was isolated with the Dounce homogenization method according to the Mitochondria Isolation Kit for Cultured Cells specifications (Thermo Fisher Scientific, Waltham, MA).

Immunocytochemistry and analysis of PER2 localization to mitochondria

Scr and PER2KD HMEC-1 cells were plated onto collagen coated cover slips and allowed to reach confluency. Following 24hrs of normoxia or hypoxia mitochondria were labeled using MitoTracker-deep red (100nM; Invitrogen) diluted in serum free media for 30mins at 37^{o}C. Cells were then fixed with 4% PFA for 15mins at 37^{o}C. Following PBS washes, samples were incubated with rabbit anti-Per2 (1:5000; Millipore) with 2% lamb serum and 0.1% Triton-X overnight at 4^{o}C. Cells were then washed with PBS and incubated with Alexa Fluor goat-anti rabbit IgG-488 (1:500; Invitrogen) and DAPI (1:2000; Invitrogen). Following PBS washes, the

bioRxiv preprint doi: https://doi.org/10.1101/561340; this version posted May 15, 2019. The copyright holder for this preprint (which was not certified by peer review) is the author/funder. All rights reserved. No reuse allowed without permission.

cover slips were mounted for imaging. Confocal immunofluorescent images were captured using a Zeiss 780 LSM confocal microscope with gain and laser power remaining constant between all samples. Samples were randomized and three images were blindly taken from each sample (n=6/condition). Zen imaging software was used to assess Per2 fluorescent intensity and normalized to the total number of cells per 40x field. Colocalization of Per2 to mitochondria was assessed using ImageJ colocalization threshold analysis with Pearson's correlation coefficient being reported. Analysis of the three images from each sample was averaged for each sample. Representative images were chosen for figures to best depict the results obtained.

Enzyme activities IDH, ACO, SUCLG, Complex IV, PFK

Human isocitrate dehydrogenase (IDH, Biovision, Milpitas, CA), aconitase (ACO, Abcam, Cambridge, MA), succinyl-CoA synthetase (SUCLG, Abcam, Cambridge, MA), phosphofructokinase (PFK, Biovision, Milpitas, CA) or mouse complex 4 activity (Abcam, Cambridge, MA) were measure colorimetric assay kits adhering to manufacturer's instructions.

Mitochondrial membrane potential dyes

MitoTracker Red CMXRos (Invitrogen Molecular Probes, Carlsbad, CA) and JC-1 Mitochondrial Membrane Potential Assay (Abcam, Cambridge, MA) were used per manufacturer's specifications using 5 μM of JC-1 for 30 minutes at 37C. JC-1 quantification was done by calculating mean intensity.

13C-tracers *in vitro*. HMEC-1s were serum starved in either MCDB131 (low glucose) or glucose-free DMEM for 24 h prior to assay. Respective mediums were supplemented with either 12 mM U-^{13}C-glucose (Cambridge Isotope Laboratories, Tewksbury, MA) or 166.67 μM 1,2-$^{13}C_2$-palmitic acid (Cambridge Isotope Laboratories, Tewksbury, MA) in hypoxia or normoxia for 24 h. Frozen cell pellets were extracted at $2e^6$ cells/mL in ice cold lysis/ extraction buffer (methanol:acetonitrile:water 5:3:2). Samples were agitated at 4 °C for 30 min followed by centrifugation at 10,000 g for 10 min at 4 °C. Protein and lipid pellets were discarded, and supernatants were stored at -80 °C prior to metabolomics analysis. Ten μL of extracts were

bioRxiv preprint doi: https://doi.org/10.1101/561340; this version posted May 15, 2019. The copyright holder for this preprint (which was not certified by peer review) is the author/funder. All rights reserved. No reuse allowed without permission.

injected into a UHPLC system (Vanquish, Thermo, San Jose, CA, USA) and run on a Kinetex C18 column (150 x 2.1 mm, 1.7 µm - Phenomenex, Torrance, CA, USA). Solvents were Optima H2O (Phase A) and Optima acetonitrile (Phase B) supplemented with 0.1% formic acid for positive mode runs and 1 mM NH4OAc for negative mode runs. For [U-^{13}C]-glucose flux analysis (Thwe et al., 2017), samples were run on a 3 min isocratic (95% A, 5% B) run at 250 µL/min (Nemkov et al., 2015; Nemkov et al., 2017). For [1,2-$^{13}C_2$]-palmitate flux analysis, samples were analyzed using a 9 min gradient from 5-95% acetonitrile organic phase at 400 µL/min. The autosampler was held at 7 °C for all runs; the column compartment was held at 25 °C for the 3 min method and 45 °C for the 9 min method (McCurdy et al., 2016). The UHPLC system was coupled online with a Q Exactive mass spectrometer (Thermo, Bremen, Germany), scanning in Full MS mode (2 µscans) at 70,000 resolution in the 60-900 m/z range in negative and then positive ion mode (separate runs). Eluate was subjected to electrospray ionization (ESI) with 4 kV spray voltage. Nitrogen gas settings were 15 sheath gas and 5 auxiliary gas for the 3 min runs; 45 sheath gas and 15 auxiliary gas for the 9 min runs. Metabolite assignments and isotopologue distributions were determined using Maven (Princeton, NJ, USA), upon conversion of '*.raw*' files to '*.mzXML*' format through MassMatrix (Cleveland, OH, USA). Chromatographic and MS technical stability were assessed by determining CVs for heavy and light isotopologues in a technical mixture of extract run every 10 injections.

Cell permeability - TEER method

HMEC-1 were grown on polycarbonate permeable supports (0.4-µm pore, 6.5-mm diam; Corning Life Sciences, Acton, MA) at a cell density of 0.3×10^4 cells / well. Confluent HMEC-1 were placed in a hypoxia chamber (Coy Laboratory Products Inc., Grass Lake, MI) in preequilibrated hypoxic medium at 1% O_2. Transendothelial electrical resistance (TEER) was measured with the EVOM2 voltohmmeter (World Precision Instrument, Sarasota, FL, USA). Value of blank well was subtracted.

Light sensing cells

bioRxiv preprint doi: https://doi.org/10.1101/561340; this version posted May 15, 2019. The copyright holder for this preprint (which was not certified by peer review) is the author/funder. All rights reserved. No reuse allowed without permission.

HMEC-1 WT cells were transfected with pCMV6-Entry (C-terminal Myc and DDK Tagged, OriGene Technologies, Rockville, MD) or OPN4 (Myc-DDK-Tagged)-pCMV6-Entry transcript variant 1 (TrueORF Gold Expression-Validated cDNA Clones from OriGene Technologies, Rockville, MD) using FuGene HD Transfection Reagent (Promega, Madison, WI). After transfection, cells were kept in complete darkness until room light (~200 LUX) or intense light (~10,000 LUX) exposures for 30 minutes. Melanopsin protein expression validation was done by isolating protein using RIPA buffer (Thermo Fisher Scientific, Waltham, MA) supplemented with protease and phosphatase inhibitor cocktail (Thermo Fisher Scientific, Waltham, MA). Immunoblotting for anti-DDK (OriGene Technologies, Rockville, MD) was used to detect DDK-tagged melanopsin in transfected cells. Light-sensing cells subjected to glycolytic or mitochondrial stress tests on the Seahorse Bioanalyzer were exposed to light 30 min prior to Seahorse analyses.

cAMP ELISA and phospho-CREB assays

Phospho-CREB (S133) Immunoassay (R&D Systems, Minneapolis, MN) or cAMP Parameter Assay Kit for human (R&D Systems, Minneapolis, MN) were used according to the manufacturer's protocol.

Human light exposure

Healthy human volunteers were exposed to intense light exposure (10,000 LUX) for 30 min every morning for five days from 8:30 AM – 9:00 AM. 5 mL blood was drawn on day one at 8:30 AM and 9:00 AM (before and after light exposure). While light exposure was repeated every morning for the five days, the next blood draws were on day two, three and five at 9:00 AM as indicated. In subset of experiments blood draws were also performed at 9 PM after 5 days of intense light therapy. For experiments involving actigraphy watches, the same volunteers wore the watch for one week without intense light exposure and maintained wearing the watches during the second week when light exposure was included. Actigraphy data were obtained by using a validated accelerometer (Actiwatch 2). We obtained approval from the

bioRxiv preprint doi: https://doi.org/10.1101/561340; this version posted May 15, 2019. The copyright holder for this preprint (which was not certified by peer review) is the author/funder. All rights reserved. No reuse allowed without permission.

Institutional Review Board (COMIRB #13-1607) for our human studies prior to written informed consent from everyone. A total of 17 healthy volunteers were enrolled (11 female and 6 male, age range between 21-44 yrs.).

Human plasma melatonin, HIF1A and triglyceride levels

Melatonin levels were measured using the MT Elisa Kit for humans (My BioSource, San Diego, CA). HIF1A levels from human plasma samples were measured using the human HIF1A ELISA Kit from Invitrogen (Carlsbad, CA). Triglycerides were determined using a human Triglyceride Quantification Assay kit (Abcam, Cambridge, MA).

Targeted metabolomics - mass spectrometry

Targeted metabolomics of human plasma following light exposure was performed as previously reported (A three-minute method for high-throughput quantitative metabolomics and quantitative tracing experiments of central carbon and nitrogen pathways (Nemkov et al., 2017). In brief, plasma samples were diluted at 1:25 in ice cold extraction solution (methanol, acetonitrile, water at a ratio of 5:3:2) and vortexed for 30 minutes at 4° C followed by removal of insoluble proteins and lipids by centrifugation at 10,000 RCF for 10 minutes at 4° C. The supernatants were collected and stored at -80° C until analysis. Analyses were performed using a Vanquish UHPLC system coupled to a Q Exactive mass spectrometer (Thermo Fisher Scientific, San Jose, CA, USA). Samples were resolved by a Kinetex C18 column (2.1 × 150 mm, 1.7 μm particle size; Phenomenex, Torrance, CA, USA) with a guard column at 25°C with an isocratic condition of 5% acetonitrile, 95% water, and 0.1% formic acid with a flow rate of 250 μL/min. The mass spectrometer was operated independently in positive or negative ion mode, scanning in Full MS mode from 60 to 900 m/z at 70,000 resolutions, with 4 kV spray voltage, 15 sheath gas, 5 auxiliary gas. Calibration was performed prior to analysis. Acquired data was converted from. raw to. mzXML file format using Mass Matrix (Cleveland, OH, USA). Metabolite assignments, isotopologue distributions, and correction for expected natural abundances of deuterium, 13C, and 15N isotopes were performed using MAVEN (Princeton,

bioRxiv preprint doi: https://doi.org/10.1101/561340; this version posted May 15, 2019. The copyright holder for this preprint (which was not certified by peer review) is the author/funder. All rights reserved. No reuse allowed without permission.

NJ, USA). Metabolite assignments were referenced to experimental retention times for over 400 analytical standards (MSMLS, IROATech, Bolton, MA, USA) and were determined over a 3-minute isocratic method with 20 μL of standards and samples injected for UHPLC/MS analysis.

Data analysis

For comparison of two groups the unpaired student t-test was performed. For multiple group comparisons a one-way analysis of variance with a Tukey's post hoc test was performed. Values are expressed as mean±SD. $P<0.05$ was considered statistically significant. For all statistical analysis, GraphPad Prism 7.0 software was used. The authors had full access to and take full responsibility for the integrity of the data. All authors have read and agree to the manuscript as written.

bioRxiv preprint doi: https://doi.org/10.1101/561340; this version posted May 15, 2019. The copyright holder for this preprint (which was not certified by peer review) is the author/funder. All rights reserved. No reuse allowed without permission.

REFERENCES

Adamovich, Y., Ladeuix, B., Golik, M., Koeners, M.P., and Asher, G. (2017). Rhythmic Oxygen Levels Reset Circadian Clocks through HIF1alpha. Cell metabolism *25*, 93-101.
Albrecht, U., Zheng, B., Larkin, D., Sun, Z.S., and Lee, C.C. (2001). MPer1 and mper2 are essential for normal resetting of the circadian clock. J Biol Rhythms *16*, 100-104.
Alva, J.A., Zovein, A.C., Monvoisin, A., Murphy, T., Salazar, A., Harvey, N.L., Carmeliet, P., and Iruela-Arispe, M.L. (2006). VE-Cadherin-Cre-recombinase transgenic mouse: a tool for lineage analysis and gene deletion in endothelial cells. Dev Dyn *235*, 759-767.
Aragones, J., Fraisl, P., Baes, M., and Carmeliet, P. (2009). Oxygen Sensors at the Crossroad of Metabolism. Cell metabolism *9*, 11-22.
Bartman, C.M., Oyama, Y., Brodsky, K., Khailova, L., Walker, L., Koeppen, M., and Eckle, T. (2017). Intense light-elicited upregulation of miR-21 facilitates glycolysis and cardioprotection through Per2-dependent mechanisms. PLoS One *12*, e0176243.
Boengler, K., Heusch, G., and Schulz, R. (2011). Nuclear-encoded mitochondrial proteins and their role in cardioprotection. Biochim Biophys Acta *1813*, 1286-1294.
Bonney, S., Hughes, K., Harter, P.N., Mittelbronn, M., Walker, L., and Eckle, T. (2013). Cardiac period 2 in myocardial ischemia: clinical implications of a light dependent protein. Int J Biochem Cell Biol *45*, 667-671.
Brutsaert, D.L. (2003). Cardiac endothelial-myocardial signaling: its role in cardiac growth, contractile performance, and rhythmicity. Physiol Rev *83*, 59-115.
Czeisler, C.A., Johnson, M.P., Duffy, J.F., Brown, E.N., Ronda, J.M., and Kronauer, R.E. (1990). Exposure to bright light and darkness to treat physiologic maladaptation to night work. N Engl J Med *322*, 1253-1259.
Davidson, S.M., and Duchen, M.R. (2007). Endothelial mitochondria: contributing to vascular function and disease. Circ Res *100*, 1128-1141.
Depner, C.M., Stothard, E.R., and Wright, K.P., Jr. (2014). Metabolic consequences of sleep and circadian disorders. Curr Diab Rep *14*, 507.
Eckle, T., Brodsky, K., Bonney, M., Packard, T., Han, J., Borchers, C.H., Mariani, T.J., Kominsky, D.J., Mittelbronn, M., and Eltzschig, H.K. (2013). HIF1A reduces acute lung injury by optimizing carbohydrate metabolism in the alveolar epithelium. PLoS Biol *11*, e1001665.
Eckle, T., Grenz, A., Kohler, D., Redel, A., Falk, M., Rolauffs, B., Osswald, H., Kehl, F., and Eltzschig, H.K. (2006). Systematic evaluation of a novel model for cardiac ischemic preconditioning in mice. Am J Physiol Heart Circ Physiol *291*, H2533-2540.
Eckle, T., Hartmann, K., Bonney, S., Reithel, S., Mittelbronn, M., Walker, L.A., Lowes, B.D., Han, J., Borchers, C.H., Buttrick, P.M., *et al.* (2012). Adora2b-elicited Per2 stabilization promotes a HIF-dependent metabolic switch crucial for myocardial adaptation to ischemia. Nat Med *18*, 774-782.
Eckle, T., Koeppen, M., and Eltzschig, H. (2011). Use of a hanging weight system for coronary artery occlusion in mice. J Vis Exp.
Eckle, T., Kohler, D., Lehmann, R., El Kasmi, K., and Eltzschig, H.K. (2008). Hypoxia-inducible factor-1 is central to cardioprotection: a new paradigm for ischemic preconditioning. Circulation *118*, 166-175.
Eckle, T., Krahn, T., Grenz, A., Kohler, D., Mittelbronn, M., Ledent, C., Jacobson, M.A., Osswald, H., Thompson, L.F., Unertl, K., *et al.* (2007). Cardioprotection by ecto-5'-nucleotidase (CD73) and A2B adenosine receptors. Circulation *115*, 1581-1590.
Eltzschig, H.K., Abdulla, P., Hoffman, E., Hamilton, K.E., Daniels, D., Schonfeld, C., Loffler, M., Reyes, G., Duszenko, M., Karhausen, J., *et al.* (2005). HIF-1-dependent

bioRxiv preprint doi: https://doi.org/10.1101/561340; this version posted May 15, 2019. The copyright holder for this preprint (which was not certified by peer review) is the author/funder. All rights reserved. No reuse allowed without permission.

repression of equilibrative nucleoside transporter (ENT) in hypoxia. J Exp Med *202*, 1493-1505.
Eltzschig, H.K., Ibla, J.C., Furuta, G.T., Leonard, M.O., Jacobson, K.A., Enjyoji, K., Robson, S.C., and Colgan, S.P. (2003). Coordinated adenine nucleotide phosphohydrolysis and nucleoside signaling in posthypoxic endothelium: role of ectonucleotidases and adenosine A2B receptors. J Exp Med *198*, 783-796.
Faou, P., and Hoogenraad, N.J. (2012). Tom34: a cytosolic cochaperone of the Hsp90/Hsp70 protein complex involved in mitochondrial protein import. Biochim Biophys Acta *1823*, 348-357.
Fukuda, R., Zhang, H., Kim, J.W., Shimoda, L., Dang, C.V., and Semenza, G.L. (2007). HIF-1 regulates cytochrome oxidase subunits to optimize efficiency of respiration in hypoxic cells. Cell *129*, 111-122.
Galaup, A., Gomez, E., Souktani, R., Durand, M., Cazes, A., Monnot, C., Teillon, J., Le Jan, S., Bouleti, C., Briois, G., *et al.* (2012). Protection against myocardial infarction and no-reflow through preservation of vascular integrity by angiopoietin-like 4. Circulation *125*, 140-149.
Gile, J., Scott, B., and Eckle, T. (2018). The Period 2 Enhancer Nobiletin as Novel Therapy in Murine Models of Circadian Disruption Resembling Delirium. Crit Care Med.
Ginsberg, H.N., Zhang, Y.L., and Hernandez-Ono, A. (2005). Regulation of plasma triglycerides in insulin resistance and diabetes. Arch Med Res *36*, 232-240.
Gloston, G.F., Yoo, S.H., and Chen, Z.J. (2017). Clock-Enhancing Small Molecules and Potential Applications in Chronic Diseases and Aging. Front Neurol *8*, 100.
Grimaldi, B., Bellet, M.M., Katada, S., Astarita, G., Hirayama, J., Amin, R.H., Granneman, J.G., Piomelli, D., Leff, T., and Sassone-Corsi, P. (2010). PER2 controls lipid metabolism by direct regulation of PPARgamma. Cell metabolism *12*, 509-520.
Gu, Y.Z., Hogenesch, J.B., and Bradfield, C.A. (2000). The PAS superfamily: sensors of environmental and developmental signals. Annu Rev Pharmacol Toxicol *40*, 519-561.
Hallows, W.C., Ptacek, L.J., and Fu, Y.H. (2013). Solving the mystery of human sleep schedules one mutation at a time. Crit Rev Biochem Mol Biol *48*, 465-475.
Han, J., Gagnon, S., Eckle, T., and Borchers, C.H. (2013a). Metabolomic analysis of key central carbon metabolism carboxylic acids as their 3-nitrophenylhydrazones by UPLC/ESI-MS. Electrophoresis *34*, 2891-2900.
Han, J., Tschernutter, V., Yang, J., Eckle, T., and Borchers, C.H. (2013b). Analysis of selected sugars and sugar phosphates in mouse heart tissue by reductive amination and liquid chromatography-electrospray ionization mass spectrometry. Anal Chem *85*, 5965-5973.
Hogenesch, J.B., Gu, Y.Z., Jain, S., and Bradfield, C.A. (1998). The basic-helix-loop-helix-PAS orphan MOP3 forms transcriptionally active complexes with circadian and hypoxia factors. Proc Natl Acad Sci U S A *95*, 5474-5479.
Kobayashi, M., Morinibu, A., Koyasu, S., Goto, Y., Hiraoka, M., and Harada, H. (2017). A circadian clock gene, PER2, activates HIF-1 as an effector molecule for recruitment of HIF-1alpha to promoter regions of its downstream genes. The FEBS journal *284*, 3804-3816.
Kohler, D., Eckle, T., Faigle, M., Grenz, A., Mittelbronn, M., Laucher, S., Hart, M.L., Robson, S.C., Muller, C.E., and Eltzschig, H.K. (2007). CD39/ectonucleoside triphosphate diphosphohydrolase 1 provides myocardial protection during cardiac ischemia/reperfusion injury. Circulation *116*, 1784-1794.
Kolosova, I.A., Mirzapoiazova, T., Adyshev, D., Usatyuk, P., Romer, L.H., Jacobson, J.R., Natarajan, V., Pearse, D.B., Garcia, J.G., and Verin, A.D. (2005). Signaling pathways involved in adenosine triphosphate-induced endothelial cell barrier enhancement. Circ Res *97*, 115-124.
Krishnan, J., Suter, M., Windak, R., Krebs, T., Felley, A., Montessuit, C., Tokarska-Schlattner, M., Aasum, E., Bogdanova, A., Perriard, E., *et al.* (2009). Activation of a

bioRxiv preprint doi: https://doi.org/10.1101/561340; this version posted May 15, 2019. The copyright holder for this preprint (which was not certified by peer review) is the author/funder. All rights reserved. No reuse allowed without permission.

HIF1alpha-PPARgamma axis underlies the integration of glycolytic and lipid anabolic pathways in pathologic cardiac hypertrophy. Cell metabolism *9*, 512-524.
Kronfeld-Schor, N., Bloch, G., and Schwartz, W.J. (2013). Animal clocks: when science meets nature. Proc Biol Sci *280*, 20131354.
Lee, J.S., Wang, R.X., Alexeev, E.E., Lanis, J.M., Battista, K.D., Glover, L.E., and Colgan, S.P. (2018). Hypoxanthine is a checkpoint stress metabolite in colonic epithelial energy modulation and barrier function. J Biol Chem *293*, 6039-6051.
Lee, P.H., and Suen, L.K. (2017). The convergent validity of Actiwatch 2 and ActiGraph Link accelerometers in measuring total sleeping period, wake after sleep onset, and sleep efficiency in free-living condition. Sleep & breathing = Schlaf & Atmung *21*, 209-215.
Lewy, A.J., Wehr, T.A., Goodwin, F.K., Newsome, D.A., and Markey, S.P. (1980). Light suppresses melatonin secretion in humans. Science *210*, 1267-1269.
Liu, W., Shen, S.M., Zhao, X.Y., and Chen, G.Q. (2012). Targeted genes and interacting proteins of hypoxia inducible factor-1. Int J Biochem Mol Biol *3*, 165-178.
Luo, B., Groenke, K., Takors, R., Wandrey, C., and Oldiges, M. (2007). Simultaneous determination of multiple intracellular metabolites in glycolysis, pentose phosphate pathway and tricarboxylic acid cycle by liquid chromatography-mass spectrometry. J Chromatogr A *1147*, 153-164.
Martino, T.A., Tata, N., Belsham, D.D., Chalmers, J., Straume, M., Lee, P., Pribiag, H., Khaper, N., Liu, P.P., Dawood, F., *et al.* (2007). Disturbed diurnal rhythm alters gene expression and exacerbates cardiovascular disease with rescue by resynchronization. Hypertension *49*, 1104-1113.
McCurdy, C.E., Schenk, S., Hetrick, B., Houck, J., Drew, B.G., Kaye, S., Lashbrook, M., Bergman, B.C., Takahashi, D.L., Dean, T.A., *et al.* (2016). Maternal obesity reduces oxidative capacity in fetal skeletal muscle of Japanese macaques. JCI insight *1*, e86612.
McIntosh, B.E., Hogenesch, J.B., and Bradfield, C.A. (2010). Mammalian Per-Arnt-Sim proteins in environmental adaptation. Annu Rev Physiol *72*, 625-645.
Montaigne, D., Marechal, X., Modine, T., Coisne, A., Mouton, S., Fayad, G., Ninni, S., Klein, C., Ortmans, S., Seunes, C., *et al.* (2018). Daytime variation of perioperative myocardial injury in cardiac surgery and its prevention by Rev-Erbalpha antagonism: a single-centre propensity-matched cohort study and a randomised study. Lancet *391*, 59-69.
Moore, A., Zielinski, T., and Millar, A.J. (2014). Online period estimation and determination of rhythmicity in circadian data, using the BioDare data infrastructure. Methods Mol Biol *1158*, 13-44.
Nemkov, T., D'Alessandro, A., and Hansen, K.C. (2015). Three-minute method for amino acid analysis by UHPLC and high-resolution quadrupole orbitrap mass spectrometry. Amino Acids *47*, 2345-2357.
Nemkov, T., Hansen, K.C., and D'Alessandro, A. (2017). A three-minute method for high-throughput quantitative metabolomics and quantitative tracing experiments of central carbon and nitrogen pathways. Rapid Commun Mass Spectrom *31*, 663-673.
O'Neill, J.S., Maywood, E.S., Chesham, J.E., Takahashi, J.S., and Hastings, M.H. (2008). cAMP-dependent signaling as a core component of the mammalian circadian pacemaker. Science *320*, 949-953.
Oster, H., Challet, E., Ott, V., Arvat, E., de Kloet, E.R., Dijk, D.J., Lightman, S., Vgontzas, A., and Van Cauter, E. (2017). The Functional and Clinical Significance of the 24-Hour Rhythm of Circulating Glucocorticoids. Endocr Rev *38*, 3-45.
Oyama, Y., Bartman, C.M., Gile, J., Sehrt, D., and Eckle, T. (2018). The circadian PER2 enhancer Nobiletin reverses the deleterious effects of midazolam in myocardial ischemia and reperfusion injury. Curr Pharm Des.

bioRxiv preprint doi: https://doi.org/10.1101/561340; this version posted May 15, 2019. The copyright holder for this preprint (which was not certified by peer review) is the author/funder. All rights reserved. No reuse allowed without permission.

Peek, C.B., Affinati, A.H., Ramsey, K.M., Kuo, H.Y., Yu, W., Sena, L.A., Ilkayeva, O., Marcheva, B., Kobayashi, Y., Omura, C., *et al.* (2013). Circadian clock NAD+ cycle drives mitochondrial oxidative metabolism in mice. Science *342*, 1243417.
Reffelmann, T., and Kloner, R.A. (2006). The no-reflow phenomenon: A basic mechanism of myocardial ischemia and reperfusion. Basic Res Cardiol *101*, 359-372.
Remi, J. (2015). Humans Entrain to Sunlight - Impact of Social Jet Lag on Disease and Implications for Critical Illness. Curr Pharm Des *21*, 3431-3437.
Rey, G., Valekunja, U.K., Feeney, K.A., Wulund, L., Milev, N.B., Stangherlin, A., Ansel-Bollepalli, L., Velagapudi, V., O'Neill, J.S., and Reddy, A.B. (2016). The Pentose Phosphate Pathway Regulates the Circadian Clock. Cell metabolism *24*, 462-473.
Schibler, U., Gotic, I., Saini, C., Gos, P., Curie, T., Emmenegger, Y., Sinturel, F., Gosselin, P., Gerber, A., Fleury-Olela, F., *et al.* (2015). Clock-Talk: Interactions between Central and Peripheral Circadian Oscillators in Mammals. Cold Spring Harb Symp Quant Biol *80*, 223-232.
Schmiedl, A., Richter, J., and Schnabel, P.A. (2002). Different preservation of myocardial capillary endothelial cells and cardiomyocytes during and after cardioplegic ischemia (25 degrees C) of canine hearts. Pathol Res Pract *198*, 281-290.
Schroeder, A.M., Truong, D., Loh, D.H., Jordan, M.C., Roos, K.P., and Colwell, C.S. (2012). Voluntary scheduled exercise alters diurnal rhythms of behaviour, physiology and gene expression in wild-type and vasoactive intestinal peptide-deficient mice. J Physiol *590*, 6213-6226.
Semenza, G.L. (2011). Hypoxia. Cross talk between oxygen sensing and the cell cycle machinery. Am J Physiol Cell Physiol *301*, C550-552.
Semenza, G.L. (2014). Hypoxia-inducible factor 1 and cardiovascular disease. Annu Rev Physiol *76*, 39-56.
Seo, S.W., Koeppen, M., Bonney, S., Gobel, M., Thayer, M., Harter, P.N., Ravid, K., Eltzschig, H.K., Mittelbronn, M., Walker, L., *et al.* (2015). Differential Tissue-Specific Function of Adora2b in Cardioprotection. J Immunol *195*, 1732-1743.
Solaini, G., Baracca, A., Lenaz, G., and Sgarbi, G. (2010). Hypoxia and mitochondrial oxidative metabolism. Biochim Biophys Acta *1797*, 1171-1177.
Spencer, F.A., Goldberg, R.J., Becker, R.C., and Gore, J.M. (1998). Seasonal distribution of acute myocardial infarction in the second National Registry of Myocardial Infarction. J Am Coll Cardiol *31*, 1226-1233.
Takahashi, J.S. (2017). Transcriptional architecture of the mammalian circadian clock. Nature reviews Genetics *18*, 164-179.
Taylor, B.L., and Zhulin, I.B. (1999). PAS domains: internal sensors of oxygen, redox potential, and light. Microbiol Mol Biol Rev *63*, 479-506.
Thwe, P.M., Pelgrom, L., Cooper, R., Beauchamp, S., Reisz, J.A., D'Alessandro, A., Everts, B., and Amiel, E. (2017). Cell-Intrinsic Glycogen Metabolism Supports Early Glycolytic Reprogramming Required for Dendritic Cell Immune Responses. Cell metabolism *26*, 558-567.e555.
Vasile, V.C., Babuin, L., Giannitsis, E., Katus, H.A., and Jaffe, A.S. (2008). Relationship of MRI-determined infarct size and cTnI measurements in patients with ST-elevation myocardial infarction. Clin Chem *54*, 617-619.
Viswambharan, H., Carvas, J.M., Antic, V., Marecic, A., Jud, C., Zaugg, C.E., Ming, X.F., Montani, J.P., Albrecht, U., and Yang, Z. (2007). Mutation of the circadian clock gene Per2 alters vascular endothelial function. Circulation *115*, 2188-2195.
Wang, C.Y., Wen, M.S., Wang, H.W., Hsieh, I.C., Li, Y., Liu, P.Y., Lin, F.C., and Liao, J.K. (2008). Increased vascular senescence and impaired endothelial progenitor cell function mediated by mutation of circadian gene Per2. Circulation *118*, 2166-2173.

bioRxiv preprint doi: https://doi.org/10.1101/561340; this version posted May 15, 2019. The copyright holder for this preprint (which was not certified by peer review) is the author/funder. All rights reserved. No reuse allowed without permission.

Wu, Y., Tang, D., Liu, N., Xiong, W., Huang, H., Li, Y., Ma, Z., Zhao, H., Chen, P., Qi, X., *et al.* (2017). Reciprocal Regulation between the Circadian Clock and Hypoxia Signaling at the Genome Level in Mammals. Cell metabolism *25*, 73-85.
Yang, Q., He, G.W., Underwood, M.J., and Yu, C.M. (2016). Cellular and molecular mechanisms of endothelial ischemia/reperfusion injury: perspectives and implications for postischemic myocardial protection. Am J Transl Res *8*, 765-777.
Yoo, S.H., Yamazaki, S., Lowrey, P.L., Shimomura, K., Ko, C.H., Buhr, E.D., Siepka, S.M., Hong, H.K., Oh, W.J., Yoo, O.J., *et al.* (2004). PERIOD2::LUCIFERASE real-time reporting of circadian dynamics reveals persistent circadian oscillations in mouse peripheral tissues. Proc Natl Acad Sci U S A *101*, 5339-5346.
Yorguner Kupeli, N., Bulut, N.S., Carkaxhiu Bulut, G., Kurt, E., and Kora, K. (2017). Efficacy of bright light therapy in bipolar depression. Psychiatry Res *260*, 432-438.
Yu, W., Dittenhafer-Reed, K.E., and Denu, J.M. (2012). SIRT3 protein deacetylates isocitrate dehydrogenase 2 (IDH2) and regulates mitochondrial redox status. J Biol Chem *287*, 14078-14086.
Zadeh, R.S., Shepley, M.M., Williams, G., and Chung, S.S. (2014). The impact of windows and daylight on acute-care nurses' physiological, psychological, and behavioral health. Herd *7*, 35-61.
Zerkle, A.L., Poulton, S.W., Newton, R.J., Mettam, C., Claire, M.W., Bekker, A., and Junium, C.K. (2017). Onset of the aerobic nitrogen cycle during the Great Oxidation Event. Nature *542*, 465-467.
Zhang, J., Kaasik, K., Blackburn, M.R., and Lee, C.C. (2006). Constant darkness is a circadian metabolic signal in mammals. Nature *439*, 340-343.
Zheng, B., Larkin, D.W., Albrecht, U., Sun, Z.S., Sage, M., Eichele, G., Lee, C.C., and Bradley, A. (1999). The mPer2 gene encodes a functional component of the mammalian circadian clock. Nature *400*, 169-173.
Zhou, R., Yazdi, A.S., Menu, P., and Tschopp, J. (2011). A role for mitochondria in NLRP3 inflammasome activation. Nature *469*, 221-225.

bioRxiv preprint doi: https://doi.org/10.1101/561340; this version posted May 15, 2019. The copyright holder for this preprint (which was not certified by peer review) is the author/funder. All rights reserved. No reuse allowed without permission.

Supp. Table 1.	*Affinity purification-mass spectrometry-based proteomics screen for PER2 protein interactions under hypoxic conditions*
Accession No.	PER2 protein interactions in hypoxia 1% **(bold highlights investigated/discussed pathways)**
P54577	Tyrosine--tRNA ligase, cytoplasmic OS=Homo sapiens GN=YARS PE=1 SV=4
O60684	Importin subunit alpha-7 OS=Homo sapiens GN=KPNA6 PE=1 SV=1
Q7KZ85	Transcription elongation factor SPT6 OS=Homo sapiens GN=SUPT6H PE=1 SV=2
Q9NTK5	Obg-like ATPase 1 OS=Homo sapiens GN=OLA1 PE=1 SV=2
P53618	Coatomer subunit beta OS=Homo sapiens GN=COPB1 PE=1 SV=3
P13667	Protein disulfide-isomerase A4 OS=Homo sapiens GN=PDIA4 PE=1 SV=2
P56192	Methionine--tRNA ligase, cytoplasmic OS=Homo sapiens GN=MARS PE=1 SV=2
P31327	Carbamoyl-phosphate synthase [ammonia], mitochondrial OS=Homo sapiens GN=CPS1 PE=1 SV=2
P39687	Acidic leucine-rich nuclear phosphoprotein 32 family member A OS=Homo sapiens GN=ANP32A PE=1 SV=1
Q00796	Sorbitol dehydrogenase OS=Homo sapiens GN=SORD PE=1 SV=4
P41252	Isoleucine--tRNA ligase, cytoplasmic OS=Homo sapiens GN=IARS PE=1 SV=2
P11498	Pyruvate carboxylase, mitochondrial OS=Homo sapiens GN=PC PE=1 SV=2
P29401	Transketolase OS=Homo sapiens GN=TKT PE=1 SV=3
P27694	Replication protein A 70 kDa DNA-binding subunit OS=Homo sapiens GN=RPA1 PE=1 SV=2
P07195	**L-lactate dehydrogenase B chain OS=Homo sapiens GN=LDHB PE=1 SV=2**
P78386	Keratin, type II cuticular Hb5 OS=Homo sapiens GN=KRT85 PE=1 SV=1
Q9BY44	Eukaryotic translation initiation factor 2A OS=Homo sapiens GN=EIF2A PE=1 SV=3
P48444	Coatomer subunit delta OS=Homo sapiens GN=ARCN1 PE=1 SV=1
P61626	Lysozyme C OS=Homo sapiens GN=LYZ PE=1 SV=1
Q9BRJ2	39S ribosomal protein L45, mitochondrial OS=Homo sapiens GN=MRPL45 PE=1 SV=2
Q9NSE4	Isoleucine--tRNA ligase, mitochondrial OS=Homo sapiens GN=IARS2 PE=1 SV=2
Q9Y3A5	Ribosome maturation protein SBDS OS=Homo sapiens GN=SBDS PE=1 SV=4

bioRxiv preprint doi: https://doi.org/10.1101/561340; this version posted May 15, 2019. The copyright holder for this preprint (which was not certified by peer review) is the author/funder. All rights reserved. No reuse allowed without permission.

P02788	Lactotransferrin OS=Homo sapiens GN=LTF PE=1 SV=6
P04062	Glucosylceramidase OS=Homo sapiens GN=GBA PE=1 SV=3
Q9HCC0	Methylcrotonoyl-CoA carboxylase beta chain, mitochondrial OS=Homo sapiens GN=MCCC2 PE=1 SV=1
P37268	Squalene synthase OS=Homo sapiens GN=FDFT1 PE=1 SV=1
P12081	Histidine--tRNA ligase, cytoplasmic OS=Homo sapiens GN=HARS PE=1 SV=2
P61011	Signal recognition particle 54 kDa protein OS=Homo sapiens GN=SRP54 PE=1 SV=1
Q9NYK5	39S ribosomal protein L39, mitochondrial OS=Homo sapiens GN=MRPL39 PE=1 SV=3
P55060	Exportin-2 OS=Homo sapiens GN=CSE1L PE=1 SV=3
Q16777	Histone H2A type 2-C OS=Homo sapiens GN=HIST2H2AC PE=1 SV=4
P82932	28S ribosomal protein S6, mitochondrial OS=Homo sapiens GN=MRPS6 PE=1 SV=3
Q96I59	Probable asparagine--tRNA ligase, mitochondrial OS=Homo sapiens GN=NARS2 PE=1 SV=3
P30101	Protein disulfide-isomerase A3 OS=Homo sapiens GN=PDIA3 PE=1 SV=4
O15355	Protein phosphatase 1G OS=Homo sapiens GN=PPM1G PE=1 SV=1
P51398	28S ribosomal protein S29, mitochondrial OS=Homo sapiens GN=DAP3 PE=1 SV=1
Q9GZZ8	Extracellular glycoprotein lacritin OS=Homo sapiens GN=LACRT PE=1 SV=1
P50336	Protoporphyrinogen oxidase OS=Homo sapiens GN=PPOX PE=1 SV=1
O60313	Dynamin-like 120 kDa protein, mitochondrial OS=Homo sapiens GN=OPA1 PE=1 SV=3
P31025	Lipocalin-1 OS=Homo sapiens GN=LCN1 PE=1 SV=1
Q6L8Q7	2',5'-phosphodiesterase 12 OS=Homo sapiens GN=PDE12 PE=1 SV=2
O00629	Importin subunit alpha-3 OS=Homo sapiens GN=KPNA4 PE=1 SV=1
P10768	S-formylglutathione hydrolase OS=Homo sapiens GN=ESD PE=1 SV=2
Q9BYD6	39S ribosomal protein L1, mitochondrial OS=Homo sapiens GN=MRPL1 PE=1 SV=2
Q92665	28S ribosomal protein S31, mitochondrial OS=Homo sapiens GN=MRPS31 PE=1 SV=3
P43490	Nicotinamide phosphoribosyltransferase OS=Homo sapiens GN=NAMPT PE=1 SV=1
Q8N5N7	39S ribosomal protein L50, mitochondrial OS=Homo sapiens GN=MRPL50 PE=1 SV=2

bioRxiv preprint doi: https://doi.org/10.1101/561340; this version posted May 15, 2019. The copyright holder for this preprint (which was not certified by peer review) is the author/funder. All rights reserved. No reuse allowed without permission.

Q16555	Dihydropyrimidinase-related protein 2 OS=Homo sapiens GN=DPYSL2 PE=1 SV=1
O95573	Long-chain-fatty-acid--CoA ligase 3 OS=Homo sapiens GN=ACSL3 PE=1 SV=3
O94903	Proline synthase co-transcribed bacterial homolog protein OS=Homo sapiens GN=PROSC PE=1 SV=1
Q15785	**Mitochondrial import receptor subunit TOM34 OS=Homo sapiens GN=TOMM34 PE=1 SV=2**
O95218	Zinc finger Ran-binding domain-containing protein 2 OS=Homo sapiens GN=ZRANB2 PE=1 SV=2
P09622	Dihydrolipoyl dehydrogenase, mitochondrial OS=Homo sapiens GN=DLD PE=1 SV=2
P47813	Eukaryotic translation initiation factor 1A, X-chromosomal OS=Homo sapiens GN=EIF1AX PE=1 SV=2
Q9BV79	Trans-2-enoyl-CoA reductase, mitochondrial OS=Homo sapiens GN=MECR PE=1 SV=2
O00410	Importin-5 OS=Homo sapiens GN=IPO5 PE=1 SV=4
Q8NBN7	Retinol dehydrogenase 13 OS=Homo sapiens GN=RDH13 PE=1 SV=2
Q92688	Acidic leucine-rich nuclear phosphoprotein 32 family member B OS=Homo sapiens GN=ANP32B PE=1 SV=1
O75821	Eukaryotic translation initiation factor 3 subunit G OS=Homo sapiens GN=EIF3G PE=1 SV=2
Q7Z4V5	Hepatoma-derived growth factor-related protein 2 OS=Homo sapiens GN=HDGFRP2 PE=1 SV=1
P82664	28S ribosomal protein S10, mitochondrial OS=Homo sapiens GN=MRPS10 PE=1 SV=2
P53597	**Succinyl-CoA ligase [ADP/GDP-forming] subunit alpha, mitochondrial OS=Homo sapiens GN=SUCLG1 PE=1 SV=4**
Q9NXG2	THUMP domain-containing protein 1 OS=Homo sapiens GN=THUMPD1 PE=1 SV=2
P08195	4F2 cell-surface antigen heavy chain OS=Homo sapiens GN=SLC3A2 PE=1 SV=3
Q9NPJ3	Acyl-coenzyme A thioesterase 13 OS=Homo sapiens GN=ACOT13 PE=1 SV=1
Q8TCC3	39S ribosomal protein L30, mitochondrial OS=Homo sapiens GN=MRPL30 PE=1 SV=1
P51553	**Isocitrate dehydrogenase [NAD] subunit gamma, mitochondrial OS=Homo sapiens GN=IDH3G PE=1 SV=1**
Q01813	ATP-dependent 6-phosphofructokinase, platelet type OS=Homo sapiens GN=PFKP PE=1 SV=2
P09429	High mobility group protein B1 OS=Homo sapiens GN=HMGB1 PE=1 SV=3

bioRxiv preprint doi: https://doi.org/10.1101/561340; this version posted May 15, 2019. The copyright holder for this preprint (which was not certified by peer review) is the author/funder. All rights reserved. No reuse allowed without permission.

Q9BYD3	39S ribosomal protein L4, mitochondrial OS=Homo sapiens GN=MRPL4 PE=1 SV=1
P10909	Clusterin OS=Homo sapiens GN=CLU PE=1 SV=1
O00203	AP-3 complex subunit beta-1 OS=Homo sapiens GN=AP3B1 PE=1 SV=3
Q96A33	Coiled-coil domain-containing protein 47 OS=Homo sapiens GN=CCDC47 PE=1 SV=1
P01833	Polymeric immunoglobulin receptor OS=Homo sapiens GN=PIGR PE=1 SV=4
Q9Y3D3	28S ribosomal protein S16, mitochondrial OS=Homo sapiens GN=MRPS16 PE=1 SV=1
Q9NVS2	28S ribosomal protein S18a, mitochondrial OS=Homo sapiens GN=MRPS18A PE=1 SV=1
Q9BWD1	Acetyl-CoA acetyltransferase, cytosolic OS=Homo sapiens GN=ACAT2 PE=1 SV=2
Q15323	Keratin, type I cuticular Ha1 OS=Homo sapiens GN=KRT31 PE=2 SV=3
Q7Z7F7	39S ribosomal protein L55, mitochondrial OS=Homo sapiens GN=MRPL55 PE=1 SV=1
Q13509	Tubulin beta-3 chain OS=Homo sapiens GN=TUBB3 PE=1 SV=2
Q9Y676	28S ribosomal protein S18b, mitochondrial OS=Homo sapiens GN=MRPS18B PE=1 SV=1
Q9H2U2	Inorganic pyrophosphatase 2, mitochondrial OS=Homo sapiens GN=PPA2 PE=1 SV=2
Q9Y3D7	Mitochondrial import inner membrane translocase subunit TIM16 OS=Homo sapiens GN=PAM16 PE=1 SV=2
Q9BWM7	Sideroflexin-3 OS=Homo sapiens GN=SFXN3 PE=1 SV=2
Q16378	Proline-rich protein 4 OS=Homo sapiens GN=PRR4 PE=1 SV=3
Q3ZCQ8	Mitochondrial import inner membrane translocase subunit TIM50 OS=Homo sapiens GN=TIMM50 PE=1 SV=2
P16615	Sarcoplasmic/endoplasmic reticulum calcium ATPase 2 OS=Homo sapiens GN=ATP2A2 PE=1 SV=1
P32119	Peroxiredoxin-2 OS=Homo sapiens GN=PRDX2 PE=1 SV=5
Q9H4M9	EH domain-containing protein 1 OS=Homo sapiens GN=EHD1 PE=1 SV=2
O43583	Density-regulated protein OS=Homo sapiens GN=DENR PE=1 SV=2
Q14197	Peptidyl-tRNA hydrolase ICT1, mitochondrial OS=Homo sapiens GN=ICT1 PE=1 SV=1
Q9UGP8	Translocation protein SEC63 homolog OS=Homo sapiens GN=SEC63 PE=1 SV=2
P10599	Thioredoxin OS=Homo sapiens GN=TXN PE=1 SV=3

bioRxiv preprint doi: https://doi.org/10.1101/561340; this version posted May 15, 2019. The copyright holder for this preprint (which was not certified by peer review) is the author/funder. All rights reserved. No reuse allowed without permission.

P11310	Medium-chain specific acyl-CoA dehydrogenase, mitochondrial OS=Homo sapiens GN=ACADM PE=1 SV=1
Q7Z2W9	39S ribosomal protein L21, mitochondrial OS=Homo sapiens GN=MRPL21 PE=1 SV=2
O94979	Protein transport protein Sec31A OS=Homo sapiens GN=SEC31A PE=1 SV=3
Q99536	Synaptic vesicle membrane protein VAT-1 homolog OS=Homo sapiens GN=VAT1 PE=1 SV=2
P04350	Tubulin beta-4A chain OS=Homo sapiens GN=TUBB4A PE=1 SV=2
P01876	Ig alpha-1 chain C region OS=Homo sapiens GN=IGHA1 PE=1 SV=2
P41250	Glycine--tRNA ligase OS=Homo sapiens GN=GARS PE=1 SV=3
Q8TCS8	Polyribonucleotide nucleotidyltransferase 1, mitochondrial OS=Homo sapiens GN=PNPT1 PE=1 SV=2
Q9BYN8	28S ribosomal protein S26, mitochondrial OS=Homo sapiens GN=MRPS26 PE=1 SV=1
P00505	Aspartate aminotransferase, mitochondrial OS=Homo sapiens GN=GOT2 PE=1 SV=3
P61769	Beta-2-microglobulin OS=Homo sapiens GN=B2M PE=1 SV=1
Q8TEA8	D-tyrosyl-tRNA(Tyr) deacylase 1 OS=Homo sapiens GN=DTD1 PE=1 SV=2
Q7Z794	Keratin, type II cytoskeletal 1b OS=Homo sapiens GN=KRT77 PE=2 SV=3
P78385	Keratin, type II cuticular Hb3 OS=Homo sapiens GN=KRT83 PE=1 SV=2
Q6IN85	Serine/threonine-protein phosphatase 4 regulatory subunit 3A OS=Homo sapiens GN=SMEK1 PE=1 SV=1
P08727	Keratin, type I cytoskeletal 19 OS=Homo sapiens GN=KRT19 PE=1 SV=4
P12273	Prolactin-inducible protein OS=Homo sapiens GN=PIP PE=1 SV=1
O75323	Protein NipSnap homolog 2 OS=Homo sapiens GN=GBAS PE=1 SV=1
Q8N983	39S ribosomal protein L43, mitochondrial OS=Homo sapiens GN=MRPL43 PE=1 SV=1
P62917	60S ribosomal protein L8 OS=Homo sapiens GN=RPL8 PE=1 SV=2
P20290	Transcription factor BTF3 OS=Homo sapiens GN=BTF3 PE=1 SV=1
Q9UBM7	7-dehydrocholesterol reductase OS=Homo sapiens GN=DHCR7 PE=1 SV=1
P05023	Sodium/potassium-transporting ATPase subunit alpha-1 OS=Homo sapiens GN=ATP1A1 PE=1 SV=1

bioRxiv preprint doi: https://doi.org/10.1101/561340; this version posted May 15, 2019. The copyright holder for this preprint (which was not certified by peer review) is the author/funder. All rights reserved. No reuse allowed without permission.

Q9BXW7	Cat eye syndrome critical region protein 5 OS=Homo sapiens GN=CECR5 PE=1 SV=1
P23921	Ribonucleoside-diphosphate reductase large subunit OS=Homo sapiens GN=RRM1 PE=1 SV=1
Q9BVJ7	Dual specificity protein phosphatase 23 OS=Homo sapiens GN=DUSP23 PE=1 SV=1
Q9P2J5	Leucine--tRNA ligase, cytoplasmic OS=Homo sapiens GN=LARS PE=1 SV=2
P50213	**Isocitrate dehydrogenase [NAD] subunit alpha, mitochondrial OS=Homo sapiens GN=IDH3A PE=1 SV=1**
P01024	Complement C3 OS=Homo sapiens GN=C3 PE=1 SV=2
Q9NVJ2	ADP-ribosylation factor-like protein 8B OS=Homo sapiens GN=ARL8B PE=1 SV=1
Q9NWU5	39S ribosomal protein L22, mitochondrial OS=Homo sapiens GN=MRPL22 PE=1 SV=1
Q99935	Proline-rich protein 1 OS=Homo sapiens GN=PROL1 PE=1 SV=2
Q96MG8	Protein-L-isoaspartate O-methyltransferase domain-containing protein 1 OS=Homo sapiens GN=PCMTD1 PE=2 SV=2
P14854	**Cytochrome c oxidase subunit 6B1 OS=Homo sapiens GN=COX6B1 PE=1 SV=2 (Complex 4)**
P00387	**NADH-cytochrome b5 reductase 3 OS=Homo sapiens GN=CYB5R3 PE=1 SV=3**
P22830	Ferrochelatase, mitochondrial OS=Homo sapiens GN=FECH PE=1 SV=2
Q6UX04	Peptidyl-prolyl cis-trans isomerase CWC27 homolog OS=Homo sapiens GN=CWC27 PE=1 SV=1
Q92947	Glutaryl-CoA dehydrogenase, mitochondrial OS=Homo sapiens GN=GCDH PE=1 SV=1
Q9BRP8	Partner of Y14 and mago OS=Homo sapiens GN=WIBG PE=1 SV=1
Q12768	WASH complex subunit strumpellin OS=Homo sapiens GN=KIAA0196 PE=1 SV=1
Q9BUF5	Tubulin beta-6 chain OS=Homo sapiens GN=TUBB6 PE=1 SV=1
Q9NVA1	**Ubiquinol-cytochrome-c reductase complex assembly factor 1 OS=Homo sapiens GN=UQCC1 PE=1 SV=3**
Q9Y3C4	EKC/KEOPS complex subunit TPRKB OS=Homo sapiens GN=TPRKB PE=1 SV=1
P61020	Ras-related protein Rab-5B OS=Homo sapiens GN=RAB5B PE=1 SV=1
Q9P032	NADH dehydrogenase [ubiquinone] 1 alpha subcomplex assembly factor 4 OS=Homo sapiens GN=NDUFAF4 PE=1 SV=1
P49915	GMP synthase [glutamine-hydrolyzing] OS=Homo sapiens GN=GMPS PE=1 SV=1

bioRxiv preprint doi: https://doi.org/10.1101/561340; this version posted May 15, 2019. The copyright holder for this preprint (which was not certified by peer review) is the author/funder. All rights reserved. No reuse allowed without permission.

Q9UBP6	tRNA (guanine-N(7)-)-methyltransferase OS=Homo sapiens GN=METTL1 PE=1 SV=1
O75964	**ATP synthase subunit g, mitochondrial OS=Homo sapiens GN=ATP5L PE=1 SV=3**
Q9HDC9	Adipocyte plasma membrane-associated protein OS=Homo sapiens GN=APMAP PE=1 SV=2
P82663	28S ribosomal protein S25, mitochondrial OS=Homo sapiens GN=MRPS25 PE=1 SV=1
Q02338	D-beta-hydroxybutyrate dehydrogenase, mitochondrial OS=Homo sapiens GN=BDH1 PE=1 SV=3
O75556	Mammaglobin-B OS=Homo sapiens GN=SCGB2A1 PE=1 SV=1
P01834	Ig kappa chain C region OS=Homo sapiens GN=IGKC PE=1 SV=1
Q9Y3D6	Mitochondrial fission 1 protein OS=Homo sapiens GN=FIS1 PE=1 SV=2
O95881	Thioredoxin domain-containing protein 12 OS=Homo sapiens GN=TXNDC12 PE=1 SV=1
Q8N1N4	Keratin, type II cytoskeletal 78 OS=Homo sapiens GN=KRT78 PE=2 SV=2
Q6UW78	UPF0723 protein C11orf83 OS=Homo sapiens GN=C11orf83 PE=1 SV=2
Q15067	Peroxisomal acyl-coenzyme A oxidase 1 OS=Homo sapiens GN=ACOX1 PE=1 SV=3
P50443	Sulfate transporter OS=Homo sapiens GN=SLC26A2 PE=1 SV=2
P25789	Proteasome subunit alpha type-4 OS=Homo sapiens GN=PSMA4 PE=1 SV=1
P52294	Importin subunit alpha-5 OS=Homo sapiens GN=KPNA1 PE=1 SV=3
Q5T653	39S ribosomal protein L2, mitochondrial OS=Homo sapiens GN=MRPL2 PE=1 SV=2
Q4U2R6	39S ribosomal protein L51, mitochondrial OS=Homo sapiens GN=MRPL51 PE=1 SV=1
P68366	Tubulin alpha-4A chain OS=Homo sapiens GN=TUBA4A PE=1 SV=1
P22102	Trifunctional purine biosynthetic protein adenosine-3 OS=Homo sapiens GN=GART PE=1 SV=1
Q9Y3D5	28S ribosomal protein S18c, mitochondrial OS=Homo sapiens GN=MRPS18C PE=1 SV=1
Q15691	Microtubule-associated protein RP/EB family member 1 OS=Homo sapiens GN=MAPRE1 PE=1 SV=3
Q13451	Peptidyl-prolyl cis-trans isomerase FKBP5 OS=Homo sapiens GN=FKBP5 PE=1 SV=2
P11908	Ribose-phosphate pyrophosphokinase 2 OS=Homo sapiens GN=PRPS2 PE=1 SV=2

bioRxiv preprint doi: https://doi.org/10.1101/561340; this version posted May 15, 2019. The copyright holder for this preprint (which was not certified by peer review) is the author/funder. All rights reserved. No reuse allowed without permission.

O43837	Isocitrate dehydrogenase [NAD] subunit beta, mitochondrial OS=Homo sapiens GN=IDH3B PE=1 SV=2
Q96DA0	Zymogen granule protein 16 homolog B OS=Homo sapiens GN=ZG16B PE=1 SV=3
Q7Z7K0	COX assembly mitochondrial protein homolog OS=Homo sapiens GN=CMC1 PE=1 SV=1
Q8N5M4	Tetratricopeptide repeat protein 9C OS=Homo sapiens GN=TTC9C PE=1 SV=1
O43776	Asparagine--tRNA ligase, cytoplasmic OS=Homo sapiens GN=NARS PE=1 SV=1
Q9Y4B6	Protein VPRBP OS=Homo sapiens GN=VPRBP PE=1 SV=3
P04818	Thymidylate synthase OS=Homo sapiens GN=TYMS PE=1 SV=3
O00743	Serine/threonine-protein phosphatase 6 catalytic subunit OS=Homo sapiens GN=PPP6C PE=1 SV=1
P46459	Vesicle-fusing ATPase OS=Homo sapiens GN=NSF PE=1 SV=3
Q9BYC8	39S ribosomal protein L32, mitochondrial OS=Homo sapiens GN=MRPL32 PE=1 SV=1
P06702	Protein S100-A9 OS=Homo sapiens GN=S100A9 PE=1 SV=1
O75348	V-type proton ATPase subunit G 1 OS=Homo sapiens GN=ATP6V1G1 PE=1 SV=3
Q9BSJ8	Extended synaptotagmin-1 OS=Homo sapiens GN=ESYT1 PE=1 SV=1
P26640	Valine--tRNA ligase OS=Homo sapiens GN=VARS PE=1 SV=4
Q9UK45	U6 snRNA-associated Sm-like protein LSm7 OS=Homo sapiens GN=LSM7 PE=1 SV=1
Q16540	39S ribosomal protein L23, mitochondrial OS=Homo sapiens GN=MRPL23 PE=1 SV=1
P27816	Microtubule-associated protein 4 OS=Homo sapiens GN=MAP4 PE=1 SV=3
Q15738	Sterol-4-alpha-carboxylate 3-dehydrogenase, decarboxylating OS=Homo sapiens GN=NSDHL PE=1 SV=2
P60520	Gamma-aminobutyric acid receptor-associated protein-like 2 OS=Homo sapiens GN=GABARAPL2 PE=1 SV=1
Q9H061	Transmembrane protein 126A OS=Homo sapiens GN=TMEM126A PE=1 SV=1
P09001	39S ribosomal protein L3, mitochondrial OS=Homo sapiens GN=MRPL3 PE=1 SV=1
P48735	Isocitrate dehydrogenase [NADP], mitochondrial OS=Homo sapiens GN=IDH2 PE=1 SV=2
Q7Z7H8	39S ribosomal protein L10, mitochondrial OS=Homo sapiens GN=MRPL10 PE=1 SV=3

bioRxiv preprint doi: https://doi.org/10.1101/561340; this version posted May 15, 2019. The copyright holder for this preprint (which was not certified by peer review) is the author/funder. All rights reserved. No reuse allowed without permission.

P60900	Proteasome subunit alpha type-6 OS=Homo sapiens GN=PSMA6 PE=1 SV=1
Q9BRQ8	Apoptosis-inducing factor 2 OS=Homo sapiens GN=AIFM2 PE=1 SV=1
P30084	Enoyl-CoA hydratase, mitochondrial OS=Homo sapiens GN=ECHS1 PE=1 SV=4
Q9HAV7	GrpE protein homolog 1, mitochondrial OS=Homo sapiens GN=GRPEL1 PE=1 SV=2
Q8N5K1	CDGSH iron-sulfur domain-containing protein 2 OS=Homo sapiens GN=CISD2 PE=1 SV=1
P49721	Proteasome subunit beta type-2 OS=Homo sapiens GN=PSMB2 PE=1 SV=1
Q96EY7	Pentatricopeptide repeat domain-containing protein 3, mitochondrial OS=Homo sapiens GN=PTCD3 PE=1 SV=3
P06744	Glucose-6-phosphate isomerase OS=Homo sapiens GN=GPI PE=1 SV=4
P35244	Replication protein A 14 kDa subunit OS=Homo sapiens GN=RPA3 PE=1 SV=1
P41567	Eukaryotic translation initiation factor 1 OS=Homo sapiens GN=EIF1 PE=1 SV=1
Q08257	Quinone oxidoreductase OS=Homo sapiens GN=CRYZ PE=1 SV=1
P22307	Non-specific lipid-transfer protein OS=Homo sapiens GN=SCP2 PE=1 SV=2
O00442	RNA 3'-terminal phosphate cyclase OS=Homo sapiens GN=RTCA PE=1 SV=1
Q92900	Regulator of nonsense transcripts 1 OS=Homo sapiens GN=UPF1 PE=1 SV=2
O75394	39S ribosomal protein L33, mitochondrial OS=Homo sapiens GN=MRPL33 PE=1 SV=1
Q96EL2	28S ribosomal protein S24, mitochondrial OS=Homo sapiens GN=MRPS24 PE=1 SV=1
Q96KG9	N-terminal kinase-like protein OS=Homo sapiens GN=SCYL1 PE=1 SV=1
Q8WWY3	U4/U6 small nuclear ribonucleoprotein Prp31 OS=Homo sapiens GN=PRPF31 PE=1 SV=2
P09132	Signal recognition particle 19 kDa protein OS=Homo sapiens GN=SRP19 PE=1 SV=3
Q9UHR5	SAP30-binding protein OS=Homo sapiens GN=SAP30BP PE=1 SV=1
Q16850	Lanosterol 14-alpha demethylase OS=Homo sapiens GN=CYP51A1 PE=1 SV=3
O95433	Activator of 90 kDa heat shock protein ATPase homolog 1 OS=Homo sapiens GN=AHSA1 PE=1 SV=1
Q14232	Translation initiation factor eIF-2B subunit alpha OS=Homo sapiens GN=EIF2B1 PE=1 SV=1
P34897	Serine hydroxymethyltransferase, mitochondrial OS=Homo sapiens GN=SHMT2 PE=1 SV=3

bioRxiv preprint doi: https://doi.org/10.1101/561340; this version posted May 15, 2019. The copyright holder for this preprint (which was not certified by peer review) is the author/funder. All rights reserved. No reuse allowed without permission.

Q30201	Hereditary hemochromatosis protein OS=Homo sapiens GN=HFE PE=1 SV=1
Q9Y606	tRNA pseudouridine synthase A, mitochondrial OS=Homo sapiens GN=PUS1 PE=1 SV=3
B9A064	Immunoglobulin lambda-like polypeptide 5 OS=Homo sapiens GN=IGLL5 PE=2 SV=2
Q9Y446	Plakophilin-3 OS=Homo sapiens GN=PKP3 PE=1 SV=1
P06396	Gelsolin OS=Homo sapiens GN=GSN PE=1 SV=1
P31947	14-3-3 protein sigma OS=Homo sapiens GN=SFN PE=1 SV=1
O15427	Monocarboxylate transporter 4 OS=Homo sapiens GN=SLC16A3 PE=1 SV=1
Q9UDW1	**Cytochrome b-c1 complex subunit 9 OS=Homo sapiens GN=UQCR10 PE=1 SV=3**
O75351	Vacuolar protein sorting-associated protein 4B OS=Homo sapiens GN=VPS4B PE=1 SV=2
P30837	Aldehyde dehydrogenase X, mitochondrial OS=Homo sapiens GN=ALDH1B1 PE=1 SV=3
Q96DB5	Regulator of microtubule dynamics protein 1 OS=Homo sapiens GN=RMDN1 PE=1 SV=1
O60613	15 kDa selenoprotein OS=Homo sapiens GN=SEP15 PE=1 SV=3
Q9Y2Z4	Tyrosine--tRNA ligase, mitochondrial OS=Homo sapiens GN=YARS2 PE=1 SV=2
Q96GC5	39S ribosomal protein L48, mitochondrial OS=Homo sapiens GN=MRPL48 PE=1 SV=2
O00267	Transcription elongation factor SPT5 OS=Homo sapiens GN=SUPT5H PE=1 SV=1
P30046	D-dopachrome decarboxylase OS=Homo sapiens GN=DDT PE=1 SV=3
Q10713	Mitochondrial-processing peptidase subunit alpha OS=Homo sapiens GN=PMPCA PE=1 SV=2
Q96IJ6	Mannose-1-phosphate guanyltransferase alpha OS=Homo sapiens GN=GMPPA PE=1 SV=1
Q13835	Plakophilin-1 OS=Homo sapiens GN=PKP1 PE=1 SV=2
P55058	Phospholipid transfer protein OS=Homo sapiens GN=PLTP PE=1 SV=1
P27348	14-3-3 protein theta OS=Homo sapiens GN=YWHAQ PE=1 SV=1
P25311	Zinc-alpha-2-glycoprotein OS=Homo sapiens GN=AZGP1 PE=1 SV=2
Q9BQA1	Methylosome protein 50 OS=Homo sapiens GN=WDR77 PE=1 SV=1
P11172	Uridine 5'-monophosphate synthase OS=Homo sapiens GN=UMPS PE=1 SV=1
P10515	Dihydrolipoyllysine-residue acetyltransferase component of pyruvate dehydrogenase complex, mitochondrial OS=Homo sapiens GN=DLAT PE=1 SV=3

bioRxiv preprint doi: https://doi.org/10.1101/561340; this version posted May 15, 2019. The copyright holder for this preprint (which was not certified by peer review) is the author/funder. All rights reserved. No reuse allowed without permission.

P42765	3-ketoacyl-CoA thiolase, mitochondrial OS=Homo sapiens GN=ACAA2 PE=1 SV=2
Q8NFV4	Alpha/beta hydrolase domain-containing protein 11 OS=Homo sapiens GN=ABHD11 PE=2 SV=1
Q10567	AP-1 complex subunit beta-1 OS=Homo sapiens GN=AP1B1 PE=1 SV=2
P17812	CTP synthase 1 OS=Homo sapiens GN=CTPS1 PE=1 SV=2
P16152	Carbonyl reductase [NADPH] 1 OS=Homo sapiens GN=CBR1 PE=1 SV=3
Q9H875	PRKR-interacting protein 1 OS=Homo sapiens GN=PRKRIP1 PE=1 SV=1
Q9BYC9	39S ribosomal protein L20, mitochondrial OS=Homo sapiens GN=MRPL20 PE=1 SV=1
P63172	Dynein light chain Tctex-type 1 OS=Homo sapiens GN=DYNLT1 PE=1 SV=1
P23527	Histone H2B type 1-O OS=Homo sapiens GN=HIST1H2BO PE=1 SV=3
Q96A35	39S ribosomal protein L24, mitochondrial OS=Homo sapiens GN=MRPL24 PE=1 SV=1
Q9NYL4	Peptidyl-prolyl cis-trans isomerase FKBP11 OS=Homo sapiens GN=FKBP11 PE=1 SV=1
O00303	Eukaryotic translation initiation factor 3 subunit F OS=Homo sapiens GN=EIF3F PE=1 SV=1
P31153	S-adenosylmethionine synthase isoform type-2 OS=Homo sapiens GN=MAT2A PE=1 SV=1
Q53H12	Acylglycerol kinase, mitochondrial OS=Homo sapiens GN=AGK PE=1 SV=2
P27824	Calnexin OS=Homo sapiens GN=CANX PE=1 SV=2
P38606	V-type proton ATPase catalytic subunit A OS=Homo sapiens GN=ATP6V1A PE=1 SV=2
P49770	Translation initiation factor eIF-2B subunit beta OS=Homo sapiens GN=EIF2B2 PE=1 SV=3
Q02952	A-kinase anchor protein 12 OS=Homo sapiens GN=AKAP12 PE=1 SV=4
P25787	Proteasome subunit alpha type-2 OS=Homo sapiens GN=PSMA2 PE=1 SV=2
P26440	Isovaleryl-CoA dehydrogenase, mitochondrial OS=Homo sapiens GN=IVD PE=1 SV=1
Q15382	GTP-binding protein Rheb OS=Homo sapiens GN=RHEB PE=1 SV=1
Q9BTT0	Acidic leucine-rich nuclear phosphoprotein 32 family member E OS=Homo sapiens GN=ANP32E PE=1 SV=1
Q96CT7	Coiled-coil domain-containing protein 124 OS=Homo sapiens GN=CCDC124 PE=1 SV=1
P00450	Ceruloplasmin OS=Homo sapiens GN=CP PE=1 SV=1
Q8TF66	Leucine-rich repeat-containing protein 15 OS=Homo sapiens GN=LRRC15 PE=1 SV=2

bioRxiv preprint doi: https://doi.org/10.1101/561340; this version posted May 15, 2019. The copyright holder for this preprint (which was not certified by peer review) is the author/funder. All rights reserved. No reuse allowed without permission.

Q9UHG3	Prenylcysteine oxidase 1 OS=Homo sapiens GN=PCYOX1 PE=1 SV=3
Q9Y2S6	Translation machinery-associated protein 7 OS=Homo sapiens GN=TMA7 PE=1 SV=1
Q9BZL1	Ubiquitin-like protein 5 OS=Homo sapiens GN=UBL5 PE=1 SV=1
P84085	ADP-ribosylation factor 5 OS=Homo sapiens GN=ARF5 PE=1 SV=2
O43504	Ragulator complex protein LAMTOR5 OS=Homo sapiens GN=LAMTOR5 PE=1 SV=1
O00487	26S proteasome non-ATPase regulatory subunit 14 OS=Homo sapiens GN=PSMD14 PE=1 SV=1
Q15165	Serum paraoxonase/arylesterase 2 OS=Homo sapiens GN=PON2 PE=1 SV=3
Q12974	Protein tyrosine phosphatase type IVA 2 OS=Homo sapiens GN=PTP4A2 PE=1 SV=1
Q9UL25	Ras-related protein Rab-21 OS=Homo sapiens GN=RAB21 PE=1 SV=3
P61009	Signal peptidase complex subunit 3 OS=Homo sapiens GN=SPCS3 PE=1 SV=1
Q9NQH7	Probable Xaa-Pro aminopeptidase 3 OS=Homo sapiens GN=XPNPEP3 PE=1 SV=1
O76031	ATP-dependent Clp protease ATP-binding subunit clpX-like, mitochondrial OS=Homo sapiens GN=CLPX PE=1 SV=2
P31949	Protein S100-A11 OS=Homo sapiens GN=S100A11 PE=1 SV=2
Q86YS7	C2 domain-containing protein 5 OS=Homo sapiens GN=C2CD5 PE=1 SV=1
Q5T749	Keratinocyte proline-rich protein OS=Homo sapiens GN=KPRP PE=1 SV=1
Q9HA64	Ketosamine-3-kinase OS=Homo sapiens GN=FN3KRP PE=1 SV=2
Q9Y5J6	Mitochondrial import inner membrane translocase subunit Tim10 B OS=Homo sapiens GN=TIMM10B PE=1 SV=1
P55081	Microfibrillar-associated protein 1 OS=Homo sapiens GN=MFAP1 PE=1 SV=2
Q9UGM3	Deleted in malignant brain tumors 1 protein OS=Homo sapiens GN=DMBT1 PE=1 SV=2
Q15758	Neutral amino acid transporter B(0) OS=Homo sapiens GN=SLC1A5 PE=1 SV=2
P57088	Transmembrane protein 33 OS=Homo sapiens GN=TMEM33 PE=1 SV=2
Q15369	Transcription elongation factor B polypeptide 1 OS=Homo sapiens GN=TCEB1 PE=1 SV=1
P62333	26S protease regulatory subunit 10B OS=Homo sapiens GN=PSMC6 PE=1 SV=1
P60468	Protein transport protein Sec61 subunit beta OS=Homo sapiens GN=SEC61B PE=1 SV=2
Q9H9B4	Sideroflexin-1 OS=Homo sapiens GN=SFXN1 PE=1 SV=4

bioRxiv preprint doi: https://doi.org/10.1101/561340; this version posted May 15, 2019. The copyright holder for this preprint (which was not certified by peer review) is the author/funder. All rights reserved. No reuse allowed without permission.

O95757	Heat shock 70 kDa protein 4L OS=Homo sapiens GN=HSPA4L PE=1 SV=3
Q08380	Galectin-3-binding protein OS=Homo sapiens GN=LGALS3BP PE=1 SV=1
Q92764	Keratin, type I cuticular Ha5 OS=Homo sapiens GN=KRT35 PE=2 SV=5
Q7L592	NADH dehydrogenase [ubiquinone] complex I, assembly factor 7 OS=Homo sapiens GN=NDUFAF7 PE=1 SV=1
Q2M389	WASH complex subunit 7 OS=Homo sapiens GN=KIAA1033 PE=1 SV=2
O75600	2-amino-3-ketobutyrate coenzyme A ligase, mitochondrial OS=Homo sapiens GN=GCAT PE=1 SV=1
Q9H3H3	UPF0696 protein C11orf68 OS=Homo sapiens GN=C11orf68 PE=1 SV=2
Q9H936	Mitochondrial glutamate carrier 1 OS=Homo sapiens GN=SLC25A22 PE=1 SV=1
Q13795	ADP-ribosylation factor-related protein 1 OS=Homo sapiens GN=ARFRP1 PE=1 SV=1
O75352	Mannose-P-dolichol utilization defect 1 protein OS=Homo sapiens GN=MPDU1 PE=1 SV=2
Q6P161	39S ribosomal protein L54, mitochondrial OS=Homo sapiens GN=MRPL54 PE=1 SV=1
P26447	Protein S100-A4 OS=Homo sapiens GN=S100A4 PE=1 SV=1
Q9H0U4	Ras-related protein Rab-1B OS=Homo sapiens GN=RAB1B PE=1 SV=1
Q13885	Tubulin beta-2A chain OS=Homo sapiens GN=TUBB2A PE=1 SV=1
P61026	Ras-related protein Rab-10 OS=Homo sapiens GN=RAB10 PE=1 SV=1
Q9NSB4	Keratin, type II cuticular Hb2 OS=Homo sapiens GN=KRT82 PE=1 SV=3
P54619	5'-AMP-activated protein kinase subunit gamma-1 OS=Homo sapiens GN=PRKAG1 PE=1 SV=1
Q6P587	Acylpyruvase FAHD1, mitochondrial OS=Homo sapiens GN=FAHD1 PE=1 SV=2
Q9Y4L1	Hypoxia up-regulated protein 1 OS=Homo sapiens GN=HYOU1 PE=1 SV=1
P11802	Cyclin-dependent kinase 4 OS=Homo sapiens GN=CDK4 PE=1 SV=2
P20340	Ras-related protein Rab-6A OS=Homo sapiens GN=RAB6A PE=1 SV=3
Q13085	Acetyl-CoA carboxylase 1 OS=Homo sapiens GN=ACACA PE=1 SV=2
P82912	28S ribosomal protein S11, mitochondrial OS=Homo sapiens GN=MRPS11 PE=1 SV=2
P49366	Deoxyhypusine synthase OS=Homo sapiens GN=DHPS PE=1 SV=1

bioRxiv preprint doi: https://doi.org/10.1101/561340; this version posted May 15, 2019. The copyright holder for this preprint (which was not certified by peer review) is the author/funder. All rights reserved. No reuse allowed without permission.

A6NDG6	Phosphoglycolate phosphatase OS=Homo sapiens GN=PGP PE=1 SV=1
P17858	**ATP-dependent 6-phosphofructokinase, liver type OS=Homo sapiens GN=PFKL PE=1 SV=6**
P54920	Alpha-soluble NSF attachment protein OS=Homo sapiens GN=NAPA PE=1 SV=3
P08237	ATP-dependent 6-phosphofructokinase, muscle type OS=Homo sapiens GN=PFKM PE=1 SV=2
Q9P0S2	**Cytochrome c oxidase assembly protein COX16 homolog, mitochondrial OS=Homo sapiens GN=COX16 PE=1 SV=1**
Q96S44	TP53-regulating kinase OS=Homo sapiens GN=TP53RK PE=1 SV=2
O95777	U6 snRNA-associated Sm-like protein LSm8 OS=Homo sapiens GN=LSM8 PE=1 SV=3
O75822	Eukaryotic translation initiation factor 3 subunit J OS=Homo sapiens GN=EIF3J PE=1 SV=2
O95968	Secretoglobin family 1D member 1 OS=Homo sapiens GN=SCGB1D1 PE=1 SV=1
P49247	Ribose-5-phosphate isomerase OS=Homo sapiens GN=RPIA PE=1 SV=3
P82675	28S ribosomal protein S5, mitochondrial OS=Homo sapiens GN=MRPS5 PE=1 SV=2
P62310	U6 snRNA-associated Sm-like protein LSm3 OS=Homo sapiens GN=LSM3 PE=1 SV=2
Q15286	Ras-related protein Rab-35 OS=Homo sapiens GN=RAB35 PE=1 SV=1
P02452	Collagen alpha-1(I) chain OS=Homo sapiens GN=COL1A1 PE=1 SV=5
O76071	Probable cytosolic iron-sulfur protein assembly protein CIAO1 OS=Homo sapiens GN=CIAO1 PE=1 SV=1
P30048	Thioredoxin-dependent peroxide reductase, mitochondrial OS=Homo sapiens GN=PRDX3 PE=1 SV=3
P20962	Parathymosin OS=Homo sapiens GN=PTMS PE=1 SV=2
Q5JTJ3	**Cytochrome c oxidase assembly factor 6 homolog OS=Homo sapiens GN=COA6 PE=1 SV=1**
Q15527	Surfeit locus protein 2 OS=Homo sapiens GN=SURF2 PE=1 SV=3
Q6MZM0	Hephaestin-like protein 1 OS=Homo sapiens GN=HEPHL1 PE=2 SV=2
Q92541	RNA polymerase-associated protein RTF1 homolog OS=Homo sapiens GN=RTF1 PE=1 SV=4
P24928	DNA-directed RNA polymerase II subunit RPB1 OS=Homo sapiens GN=POLR2A PE=1 SV=2
P01037	Cystatin-SN OS=Homo sapiens GN=CST1 PE=1 SV=3

bioRxiv preprint doi: https://doi.org/10.1101/561340; this version posted May 15, 2019. The copyright holder for this preprint (which was not certified by peer review) is the author/funder. All rights reserved. No reuse allowed without permission.

Q13228	Selenium-binding protein 1 OS=Homo sapiens GN=SELENBP1 PE=1 SV=2
O14548	**Cytochrome c oxidase subunit 7A-related protein, mitochondrial OS=Homo sapiens GN=COX7A2L PE=1 SV=2**
P24844	Myosin regulatory light polypeptide 9 OS=Homo sapiens GN=MYL9 PE=1 SV=4
Q92626	Peroxidasin homolog OS=Homo sapiens GN=PXDN PE=1 SV=2
P21281	V-type proton ATPase subunit B, brain isoform OS=Homo sapiens GN=ATP6V1B2 PE=1 SV=3
Q03426	Mevalonate kinase OS=Homo sapiens GN=MVK PE=1 SV=1
P23786	Carnitine O-palmitoyltransferase 2, mitochondrial OS=Homo sapiens GN=CPT2 PE=1 SV=2
P61619	Protein transport protein Sec61 subunit alpha isoform 1 OS=Homo sapiens GN=SEC61A1 PE=1 SV=2
Q99439	Calponin-2 OS=Homo sapiens GN=CNN2 PE=1 SV=4
P27144	Adenylate kinase 4, mitochondrial OS=Homo sapiens GN=AK4 PE=1 SV=1
Q969X5	Endoplasmic reticulum-Golgi intermediate compartment protein 1 OS=Homo sapiens GN=ERGIC1 PE=1 SV=1
O43592	Exportin-T OS=Homo sapiens GN=XPOT PE=1 SV=2
Q02252	Methylmalonate-semialdehyde dehydrogenase [acylating], mitochondrial OS=Homo sapiens GN=ALDH6A1 PE=1 SV=2
Q15645	Pachytene checkpoint protein 2 homolog OS=Homo sapiens GN=TRIP13 PE=1 SV=2
Q16706	Alpha-mannosidase 2 OS=Homo sapiens GN=MAN2A1 PE=1 SV=2
Q96EK6	Glucosamine 6-phosphate N-acetyltransferase OS=Homo sapiens GN=GNPNAT1 PE=1 SV=1
P33121	Long-chain-fatty-acid--CoA ligase 1 OS=Homo sapiens GN=ACSL1 PE=1 SV=1
Q9BY32	Inosine triphosphate pyrophosphatase OS=Homo sapiens GN=ITPA PE=1 SV=2
Q92572	AP-3 complex subunit sigma-1 OS=Homo sapiens GN=AP3S1 PE=1 SV=1
P23919	Thymidylate kinase OS=Homo sapiens GN=DTYMK PE=1 SV=4
O14561	Acyl carrier protein, mitochondrial OS=Homo sapiens GN=NDUFAB1 PE=1 SV=3
P49590	Probable histidine--tRNA ligase, mitochondrial OS=Homo sapiens GN=HARS2 PE=1 SV=1
P20061	Transcobalamin-1 OS=Homo sapiens GN=TCN1 PE=1 SV=2

bioRxiv preprint doi: https://doi.org/10.1101/561340; this version posted May 15, 2019. The copyright holder for this preprint (which was not certified by peer review) is the author/funder. All rights reserved. No reuse allowed without permission.

P0CG05	Ig lambda-2 chain C regions OS=Homo sapiens GN=IGLC2 PE=1 SV=1
O00233	26S proteasome non-ATPase regulatory subunit 9 OS=Homo sapiens GN=PSMD9 PE=1 SV=3
Q92973	Transportin-1 OS=Homo sapiens GN=TNPO1 PE=1 SV=2
Q8TAT6	Nuclear protein localization protein 4 homolog OS=Homo sapiens GN=NPLOC4 PE=1 SV=3
P04080	Cystatin-B OS=Homo sapiens GN=CSTB PE=1 SV=2
Q16891	MICOS complex subunit MIC60 OS=Homo sapiens GN=IMMT PE=1 SV=1
P36969	Phospholipid hydroperoxide glutathione peroxidase, mitochondrial OS=Homo sapiens GN=GPX4 PE=1 SV=3
P49720	Proteasome subunit beta type-3 OS=Homo sapiens GN=PSMB3 PE=1 SV=2
Q13405	39S ribosomal protein L49, mitochondrial OS=Homo sapiens GN=MRPL49 PE=1 SV=1
Q86X55	Histone-arginine methyltransferase CARM1 OS=Homo sapiens GN=CARM1 PE=1 SV=3
Q15155	Nodal modulator 1 OS=Homo sapiens GN=NOMO1 PE=1 SV=5
Q8NF37	Lysophosphatidylcholine acyltransferase 1 OS=Homo sapiens GN=LPCAT1 PE=1 SV=2
P60510	Serine/threonine-protein phosphatase 4 catalytic subunit OS=Homo sapiens GN=PPP4C PE=1 SV=1
P61019	Ras-related protein Rab-2A OS=Homo sapiens GN=RAB2A PE=1 SV=1
Q9UI10	Translation initiation factor eIF-2B subunit delta OS=Homo sapiens GN=EIF2B4 PE=1 SV=2
Q08188	Protein-glutamine gamma-glutamyltransferase E OS=Homo sapiens GN=TGM3 PE=1 SV=4
Q13162	Peroxiredoxin-4 OS=Homo sapiens GN=PRDX4 PE=1 SV=1
P55786	Puromycin-sensitive aminopeptidase OS=Homo sapiens GN=NPEPPS PE=1 SV=2
P19474	E3 ubiquitin-protein ligase TRIM21 OS=Homo sapiens GN=TRIM21 PE=1 SV=1
Q9UJ83	2-hydroxyacyl-CoA lyase 1 OS=Homo sapiens GN=HACL1 PE=1 SV=2
Q9BUP3	Oxidoreductase HTATIP2 OS=Homo sapiens GN=HTATIP2 PE=1 SV=2
Q96IU4	Alpha/beta hydrolase domain-containing protein 14B OS=Homo sapiens GN=ABHD14B PE=1 SV=1
O95487	Protein transport protein Sec24B OS=Homo sapiens GN=SEC24B PE=1 SV=2
P84101	Small EDRK-rich factor 2 OS=Homo sapiens GN=SERF2 PE=1 SV=1

bioRxiv preprint doi: https://doi.org/10.1101/561340; this version posted May 15, 2019. The copyright holder for this preprint (which was not certified by peer review) is the author/funder. All rights reserved. No reuse allowed without permission.

P48960	CD97 antigen OS=Homo sapiens GN=CD97 PE=1 SV=4
Q9H9P8	L-2-hydroxyglutarate dehydrogenase, mitochondrial OS=Homo sapiens GN=L2HGDH PE=1 SV=3
Q9BW61	DET1- and DDB1-associated protein 1 OS=Homo sapiens GN=DDA1 PE=1 SV=1
P20930	Filaggrin OS=Homo sapiens GN=FLG PE=1 SV=3
Q86SJ6	Desmoglein-4 OS=Homo sapiens GN=DSG4 PE=1 SV=1
P09110	3-ketoacyl-CoA thiolase, peroxisomal OS=Homo sapiens GN=ACAA1 PE=1 SV=2
P50552	Vasodilator-stimulated phosphoprotein OS=Homo sapiens GN=VASP PE=1 SV=3
P28072	Proteasome subunit beta type-6 OS=Homo sapiens GN=PSMB6 PE=1 SV=4
Q9NZT1	Calmodulin-like protein 5 OS=Homo sapiens GN=CALML5 PE=1 SV=2
P04259	Keratin, type II cytoskeletal 6B OS=Homo sapiens GN=KRT6B PE=1 SV=5
Q13685	Angio-associated migratory cell protein OS=Homo sapiens GN=AAMP PE=1 SV=2
Q15437	Protein transport protein Sec23B OS=Homo sapiens GN=SEC23B PE=1 SV=2
Q9UK41	Vacuolar protein sorting-associated protein 28 homolog OS=Homo sapiens GN=VPS28 PE=1 SV=1
P04632	Calpain small subunit 1 OS=Homo sapiens GN=CAPNS1 PE=1 SV=1
Q04941	Proteolipid protein 2 OS=Homo sapiens GN=PLP2 PE=1 SV=1
Q9Y296	Trafficking protein particle complex subunit 4 OS=Homo sapiens GN=TRAPPC4 PE=1 SV=1
Q9Y587	AP-4 complex subunit sigma-1 OS=Homo sapiens GN=AP4S1 PE=2 SV=1
O14972	Down syndrome critical region protein 3 OS=Homo sapiens GN=DSCR3 PE=2 SV=1
Q5VYK3	Proteasome-associated protein ECM29 homolog OS=Homo sapiens GN=ECM29 PE=1 SV=2
O15228	Dihydroxyacetone phosphate acyltransferase OS=Homo sapiens GN=GNPAT PE=1 SV=1
Q13442	28 kDa heat- and acid-stable phosphoprotein OS=Homo sapiens GN=PDAP1 PE=1 SV=1
Q9Y315	Deoxyribose-phosphate aldolase OS=Homo sapiens GN=DERA PE=1 SV=2
Q9ULA0	Aspartyl aminopeptidase OS=Homo sapiens GN=DNPEP PE=1 SV=1
P19623	Spermidine synthase OS=Homo sapiens GN=SRM PE=1 SV=1
Q7Z4G1	COMM domain-containing protein 6 OS=Homo sapiens GN=COMMD6 PE=1 SV=1

bioRxiv preprint doi: https://doi.org/10.1101/561340; this version posted May 15, 2019. The copyright holder for this preprint (which was not certified by peer review) is the author/funder. All rights reserved. No reuse allowed without permission.

Q6DKJ4	Nucleoredoxin OS=Homo sapiens GN=NXN PE=1 SV=2
Q9UBE0	SUMO-activating enzyme subunit 1 OS=Homo sapiens GN=SAE1 PE=1 SV=1
Q96AB3	Isochorismatase domain-containing protein 2, mitochondrial OS=Homo sapiens GN=ISOC2 PE=1 SV=1
Q5U5X0	Complex III assembly factor LYRM7 OS=Homo sapiens GN=LYRM7 PE=1 SV=1
Q96QA5	Gasdermin-A OS=Homo sapiens GN=GSDMA PE=1 SV=4
Q8IVF2	Protein AHNAK2 OS=Homo sapiens GN=AHNAK2 PE=1 SV=2
P98160	Basement membrane-specific heparan sulfate proteoglycan core protein OS=Homo sapiens GN=HSPG2 PE=1 SV=4
Q9H6E5	Speckle targeted PIP5K1A-regulated poly(A) polymerase OS=Homo sapiens GN=TUT1 PE=1 SV=2
P01620	Ig kappa chain V-III region SIE OS=Homo sapiens PE=1 SV=1
Q96RQ3	Methylcrotonoyl-CoA carboxylase subunit alpha, mitochondrial OS=Homo sapiens GN=MCCC1 PE=1 SV=3
Q9UBW8	COP9 signalosome complex subunit 7a OS=Homo sapiens GN=COPS7A PE=1 SV=1
Q08209	Serine/threonine-protein phosphatase 2B catalytic subunit alpha isoform OS=Homo sapiens GN=PPP3CA PE=1 SV=1
Q9BUP0	EF-hand domain-containing protein D1 OS=Homo sapiens GN=EFHD1 PE=1 SV=1
O75439	Mitochondrial-processing peptidase subunit beta OS=Homo sapiens GN=PMPCB PE=1 SV=2
Q86YQ8	Copine-8 OS=Homo sapiens GN=CPNE8 PE=1 SV=2
Q8IV08	Phospholipase D3 OS=Homo sapiens GN=PLD3 PE=1 SV=1
P00367	Glutamate dehydrogenase 1, mitochondrial OS=Homo sapiens GN=GLUD1 PE=1 SV=2
P52565	Rho GDP-dissociation inhibitor 1 OS=Homo sapiens GN=ARHGDIA PE=1 SV=3
P35613	Basigin OS=Homo sapiens GN=BSG PE=1 SV=2
P29144	Tripeptidyl-peptidase 2 OS=Homo sapiens GN=TPP2 PE=1 SV=4
P61923	Coatomer subunit zeta-1 OS=Homo sapiens GN=COPZ1 PE=1 SV=1
Q9GZY4	**Cytochrome c oxidase assembly factor 1 homolog OS=Homo sapiens GN=COA1 PE=1 SV=1**
Q9Y266	Nuclear migration protein nudC OS=Homo sapiens GN=NUDC PE=1 SV=1

bioRxiv preprint doi: https://doi.org/10.1101/561340; this version posted May 15, 2019. The copyright holder for this preprint (which was not certified by peer review) is the author/funder. All rights reserved. No reuse allowed without permission.

P40616	ADP-ribosylation factor-like protein 1 OS=Homo sapiens GN=ARL1 PE=1 SV=1
P53701	**Cytochrome c-type heme lyase OS=Homo sapiens GN=HCCS PE=1 SV=1**
Q15125	3-beta-hydroxysteroid-Delta(8),Delta(7)-isomerase OS=Homo sapiens GN=EBP PE=1 SV=3
Q8NC60	Nitric oxide-associated protein 1 OS=Homo sapiens GN=NOA1 PE=1 SV=2
Q9H6V9	UPF0554 protein C2orf43 OS=Homo sapiens GN=C2orf43 PE=1 SV=1
P36543	V-type proton ATPase subunit E 1 OS=Homo sapiens GN=ATP6V1E1 PE=1 SV=1
Q16186	Proteasomal ubiquitin receptor ADRM1 OS=Homo sapiens GN=ADRM1 PE=1 SV=2
Q01650	Large neutral amino acids transporter small subunit 1 OS=Homo sapiens GN=SLC7A5 PE=1 SV=2
Q9C0C9	E2/E3 hybrid ubiquitin-protein ligase UBE2O OS=Homo sapiens GN=UBE2O PE=1 SV=3
Q12849	G-rich sequence factor 1 OS=Homo sapiens GN=GRSF1 PE=1 SV=3
Q99798	**Aconitate hydratase, mitochondrial OS=Homo sapiens GN=ACO2 PE=1 SV=2**
O14617	AP-3 complex subunit delta-1 OS=Homo sapiens GN=AP3D1 PE=1 SV=1
P01871	Ig mu chain C region OS=Homo sapiens GN=IGHM PE=1 SV=3
Q9Y262	Eukaryotic translation initiation factor 3 subunit L OS=Homo sapiens GN=EIF3L PE=1 SV=1
Q9UBC9	Small proline-rich protein 3 OS=Homo sapiens GN=SPRR3 PE=1 SV=2
P01591	Immunoglobulin J chain OS=Homo sapiens GN=IGJ PE=1 SV=4
P30419	Glycylpeptide N-tetradecanoyltransferase 1 OS=Homo sapiens GN=NMT1 PE=1 SV=2
Q9NWS0	PIH1 domain-containing protein 1 OS=Homo sapiens GN=PIH1D1 PE=1 SV=1
Q5TAQ9	DDB1- and CUL4-associated factor 8 OS=Homo sapiens GN=DCAF8 PE=1 SV=1
P39748	Flap endonuclease 1 OS=Homo sapiens GN=FEN1 PE=1 SV=1
Q9Y241	HIG1 domain family member 1A, mitochondrial OS=Homo sapiens GN=HIGD1A PE=1 SV=1
Q15054	DNA polymerase delta subunit 3 OS=Homo sapiens GN=POLD3 PE=1 SV=2
Q969U7	Proteasome assembly chaperone 2 OS=Homo sapiens GN=PSMG2 PE=1 SV=1
Q13217	DnaJ homolog subfamily C member 3 OS=Homo sapiens GN=DNAJC3 PE=1 SV=1

bioRxiv preprint doi: https://doi.org/10.1101/561340; this version posted May 15, 2019. The copyright holder for this preprint (which was not certified by peer review) is the author/funder. All rights reserved. No reuse allowed without permission.

P45880	Voltage-dependent anion-selective channel protein 2 OS=Homo sapiens GN=VDAC2 PE=1 SV=2
P20839	Inosine-5'-monophosphate dehydrogenase 1 OS=Homo sapiens GN=IMPDH1 PE=1 SV=2
O43709	Probable 18S rRNA (guanine-N(7))-methyltransferase OS=Homo sapiens GN=WBSCR22 PE=1 SV=2
P54802	Alpha-N-acetylglucosaminidase OS=Homo sapiens GN=NAGLU PE=1 SV=2
Q9UBV2	Protein sel-1 homolog 1 OS=Homo sapiens GN=SEL1L PE=1 SV=3
Q9Y248	DNA replication complex GINS protein PSF2 OS=Homo sapiens GN=GINS2 PE=1 SV=1
P23368	NAD-dependent malic enzyme, mitochondrial OS=Homo sapiens GN=ME2 PE=1 SV=1
O00232	26S proteasome non-ATPase regulatory subunit 12 OS=Homo sapiens GN=PSMD12 PE=1 SV=3
A1L0T0	Acetolactate synthase-like protein OS=Homo sapiens GN=ILVBL PE=1 SV=2
Q14847	LIM and SH3 domain protein 1 OS=Homo sapiens GN=LASP1 PE=1 SV=2
Q14558	Phosphoribosyl pyrophosphate synthase-associated protein 1 OS=Homo sapiens GN=PRPSAP1 PE=1 SV=2
O95202	LETM1 and EF-hand domain-containing protein 1, mitochondrial OS=Homo sapiens GN=LETM1 PE=1 SV=1
P30566	Adenylosuccinate lyase OS=Homo sapiens GN=ADSL PE=1 SV=2
P17655	Calpain-2 catalytic subunit OS=Homo sapiens GN=CAPN2 PE=1 SV=6
O94925	Glutaminase kidney isoform, mitochondrial OS=Homo sapiens GN=GLS PE=1 SV=1
Q02790	Peptidyl-prolyl cis-trans isomerase FKBP4 OS=Homo sapiens GN=FKBP4 PE=1 SV=3
P80303	Nucleobindin-2 OS=Homo sapiens GN=NUCB2 PE=1 SV=2
Q99497	Protein DJ-1 OS=Homo sapiens GN=PARK7 PE=1 SV=2
Q9UBX3	Mitochondrial dicarboxylate carrier OS=Homo sapiens GN=SLC25A10 PE=1 SV=2
Q9Y6C9	Mitochondrial carrier homolog 2 OS=Homo sapiens GN=MTCH2 PE=1 SV=1
O43464	Serine protease HTRA2, mitochondrial OS=Homo sapiens GN=HTRA2 PE=1 SV=2
Q92615	La-related protein 4B OS=Homo sapiens GN=LARP4B PE=1 SV=3
P67812	Signal peptidase complex catalytic subunit SEC11A OS=Homo sapiens GN=SEC11A PE=1 SV=1

bioRxiv preprint doi: https://doi.org/10.1101/561340; this version posted May 15, 2019. The copyright holder for this preprint (which was not certified by peer review) is the author/funder. All rights reserved. No reuse allowed without permission.

P22314	Ubiquitin-like modifier-activating enzyme 1 OS=Homo sapiens GN=UBA1 PE=1 SV=3
P04183	Thymidine kinase, cytosolic OS=Homo sapiens GN=TK1 PE=1 SV=2
O96011	Peroxisomal membrane protein 11B OS=Homo sapiens GN=PEX11B PE=1 SV=1
Q9P000	COMM domain-containing protein 9 OS=Homo sapiens GN=COMMD9 PE=1 SV=2
P43897	Elongation factor Ts, mitochondrial OS=Homo sapiens GN=TSFM PE=1 SV=2
P04179	Superoxide dismutase [Mn], mitochondrial OS=Homo sapiens GN=SOD2 PE=1 SV=2
Q13423	NAD(P) transhydrogenase, mitochondrial OS=Homo sapiens GN=NNT PE=1 SV=3
O43719	HIV Tat-specific factor 1 OS=Homo sapiens GN=HTATSF1 PE=1 SV=1
Q9GZQ3	COMM domain-containing protein 5 OS=Homo sapiens GN=COMMD5 PE=1 SV=1
P58546	Myotrophin OS=Homo sapiens GN=MTPN PE=1 SV=2
Q96ND0	Protein FAM210A OS=Homo sapiens GN=FAM210A PE=1 SV=2
O43854	EGF-like repeat and discoidin I-like domain-containing protein 3 OS=Homo sapiens GN=EDIL3 PE=1 SV=1
Q9H173	Nucleotide exchange factor SIL1 OS=Homo sapiens GN=SIL1 PE=1 SV=1
Q9H814	Phosphorylated adapter RNA export protein OS=Homo sapiens GN=PHAX PE=1 SV=1
A0FGR8	Extended synaptotagmin-2 OS=Homo sapiens GN=ESYT2 PE=1 SV=1
O95071	E3 ubiquitin-protein ligase UBR5 OS=Homo sapiens GN=UBR5 PE=1 SV=2
Q6GMV3	Putative peptidyl-tRNA hydrolase PTRHD1 OS=Homo sapiens GN=PTRHD1 PE=1 SV=1
Q00688	Peptidyl-prolyl cis-trans isomerase FKBP3 OS=Homo sapiens GN=FKBP3 PE=1 SV=1
Q7Z4H8	KDEL motif-containing protein 2 OS=Homo sapiens GN=KDELC2 PE=1 SV=2
P51570	Galactokinase OS=Homo sapiens GN=GALK1 PE=1 SV=1
O75436	Vacuolar protein sorting-associated protein 26A OS=Homo sapiens GN=VPS26A PE=1 SV=2
P11217	Glycogen phosphorylase, muscle form OS=Homo sapiens GN=PYGM PE=1 SV=6
O75367	Core histone macro-H2A.1 OS=Homo sapiens GN=H2AFY PE=1 SV=4
P13693	Translationally-controlled tumor protein OS=Homo sapiens GN=TPT1 PE=1 SV=1
Q08554	Desmocollin-1 OS=Homo sapiens GN=DSC1 PE=1 SV=2

bioRxiv preprint doi: https://doi.org/10.1101/561340; this version posted May 15, 2019. The copyright holder for this preprint (which was not certified by peer review) is the author/funder. All rights reserved. No reuse allowed without permission.

O95302	Peptidyl-prolyl cis-trans isomerase FKBP9 OS=Homo sapiens GN=FKBP9 PE=1 SV=2
Q86WW8	**Cytochrome c oxidase assembly factor 5 OS=Homo sapiens GN=COA5 PE=1 SV=1**
P08473	Neprilysin OS=Homo sapiens GN=MME PE=1 SV=2
Q15181	Inorganic pyrophosphatase OS=Homo sapiens GN=PPA1 PE=1 SV=2
Q9BSE5	Agmatinase, mitochondrial OS=Homo sapiens GN=AGMAT PE=1 SV=2
O94952	F-box only protein 21 OS=Homo sapiens GN=FBXO21 PE=2 SV=2
P05114	Non-histone chromosomal protein HMG-14 OS=Homo sapiens GN=HMGN1 PE=1 SV=3
P00491	Purine nucleoside phosphorylase OS=Homo sapiens GN=PNP PE=1 SV=2
P53611	Geranylgeranyl transferase type-2 subunit beta OS=Homo sapiens GN=RABGGTB PE=1 SV=2
P49006	MARCKS-related protein OS=Homo sapiens GN=MARCKSL1 PE=1 SV=2
Q06210	Glutamine--fructose-6-phosphate aminotransferase [isomerizing] 1 OS=Homo sapiens GN=GFPT1 PE=1 SV=3
P46379	Large proline-rich protein BAG6 OS=Homo sapiens GN=BAG6 PE=1 SV=2
Q02218	2-oxoglutarate dehydrogenase, mitochondrial OS=Homo sapiens GN=OGDH PE=1 SV=3
P30626	Sorcin OS=Homo sapiens GN=SRI PE=1 SV=1
Q99436	Proteasome subunit beta type-7 OS=Homo sapiens GN=PSMB7 PE=1 SV=1
Q8WUF5	RelA-associated inhibitor OS=Homo sapiens GN=PPP1R13L PE=1 SV=4
Q6KB66	Keratin, type II cytoskeletal 80 OS=Homo sapiens GN=KRT80 PE=1 SV=2
Q9Y3D0	Mitotic spindle-associated MMXD complex subunit MIP18 OS=Homo sapiens GN=FAM96B PE=1 SV=1
P20020	Plasma membrane calcium-transporting ATPase 1 OS=Homo sapiens GN=ATP2B1 PE=1 SV=3
Q05639	Elongation factor 1-alpha 2 OS=Homo sapiens GN=EEF1A2 PE=1 SV=1
P10586	Receptor-type tyrosine-protein phosphatase F OS=Homo sapiens GN=PTPRF PE=1 SV=2
O75616	GTPase Era, mitochondrial OS=Homo sapiens GN=ERAL1 PE=1 SV=2
P30740	Leukocyte elastase inhibitor OS=Homo sapiens GN=SERPINB1 PE=1 SV=1
Q8TAE8	Growth arrest and DNA damage-inducible proteins-interacting protein 1 OS=Homo sapiens GN=GADD45GIP1 PE=1 SV=1

bioRxiv preprint doi: https://doi.org/10.1101/561340; this version posted May 15, 2019. The copyright holder for this preprint (which was not certified by peer review) is the author/funder. All rights reserved. No reuse allowed without permission.

Q9UBQ7	Glyoxylate reductase/hydroxypyruvate reductase OS=Homo sapiens GN=GRHPR PE=1 SV=1
O43847	Nardilysin OS=Homo sapiens GN=NRD1 PE=1 SV=2
P08236	Beta-glucuronidase OS=Homo sapiens GN=GUSB PE=1 SV=2
P57081	tRNA (guanine-N(7)-)-methyltransferase non-catalytic subunit WDR4 OS=Homo sapiens GN=WDR4 PE=1 SV=2
P01781	Ig heavy chain V-III region GAL OS=Homo sapiens PE=1 SV=1
P62328	Thymosin beta-4 OS=Homo sapiens GN=TMSB4X PE=1 SV=2
Q9Y5J7	Mitochondrial import inner membrane translocase subunit Tim9 OS=Homo sapiens GN=TIMM9 PE=1 SV=1
Q96K17	Transcription factor BTF3 homolog 4 OS=Homo sapiens GN=BTF3L4 PE=1 SV=1
P48507	Glutamate--cysteine ligase regulatory subunit OS=Homo sapiens GN=GCLM PE=1 SV=1
Q969Z0	Protein TBRG4 OS=Homo sapiens GN=TBRG4 PE=1 SV=1
Q96SW2	Protein cereblon OS=Homo sapiens GN=CRBN PE=1 SV=1
O15439	Multidrug resistance-associated protein 4 OS=Homo sapiens GN=ABCC4 PE=1 SV=3
O00186	Syntaxin-binding protein 3 OS=Homo sapiens GN=STXBP3 PE=1 SV=2
Q8WWC4	Uncharacterized protein C2orf47, mitochondrial OS=Homo sapiens GN=C2orf47 PE=1 SV=1
O43865	Putative adenosylhomocysteinase 2 OS=Homo sapiens GN=AHCYL1 PE=1 SV=2
Q4G0J3	La-related protein 7 OS=Homo sapiens GN=LARP7 PE=1 SV=1
Q96GD0	Pyridoxal phosphate phosphatase OS=Homo sapiens GN=PDXP PE=1 SV=2
Q8N4Q0	Zinc-binding alcohol dehydrogenase domain-containing protein 2 OS=Homo sapiens GN=ZADH2 PE=1 SV=1
O75569	Interferon-inducible double-stranded RNA-dependent protein kinase activator A OS=Homo sapiens GN=PRKRA PE=1 SV=1
O95817	BAG family molecular chaperone regulator 3 OS=Homo sapiens GN=BAG3 PE=1 SV=3
P47929	Galectin-7 OS=Homo sapiens GN=LGALS7 PE=1 SV=2
P82914	28S ribosomal protein S15, mitochondrial OS=Homo sapiens GN=MRPS15 PE=1 SV=1
Q14764	Major vault protein OS=Homo sapiens GN=MVP PE=1 SV=4

bioRxiv preprint doi: https://doi.org/10.1101/561340; this version posted May 15, 2019. The copyright holder for this preprint (which was not certified by peer review) is the author/funder. All rights reserved. No reuse allowed without permission.

P80748	Ig lambda chain V-III region LOI OS=Homo sapiens PE=1 SV=1
Q13144	Translation initiation factor eIF-2B subunit epsilon OS=Homo sapiens GN=EIF2B5 PE=1 SV=3
O60869	Endothelial differentiation-related factor 1 OS=Homo sapiens GN=EDF1 PE=1 SV=1
P30043	Flavin reductase (NADPH) OS=Homo sapiens GN=BLVRB PE=1 SV=3
Q13610	Periodic tryptophan protein 1 homolog OS=Homo sapiens GN=PWP1 PE=1 SV=1
Q9HCN4	GPN-loop GTPase 1 OS=Homo sapiens GN=GPN1 PE=1 SV=1
Q13561	Dynactin subunit 2 OS=Homo sapiens GN=DCTN2 PE=1 SV=4
Q96PZ0	Pseudouridylate synthase 7 homolog OS=Homo sapiens GN=PUS7 PE=1 SV=2
P04207	Ig kappa chain V-III region CLL OS=Homo sapiens PE=1 SV=2
Q9H9T3	Elongator complex protein 3 OS=Homo sapiens GN=ELP3 PE=1 SV=2